A NEW DIFFUSE REFLECTING MATERIAL WITH APPLICATIONS INCLUDING INTEGRATING CAVITY RING-DOWN SPECTROSCOPY

A Dissertation

by

MICHAEL THOMAS CONE

Submitted to the Office of Graduate and Professional Studies of
Texas A&M University
in partial fulfillment of the requirements for the degree of

DOCTOR OF PHILOSOPHY

Chair of Committee,	Edward S. Fry
Committee Members,	George W. Kattawar
	George R. Welch
	John W. Bevan
Head of Department,	George R. Welch

May 2014

Major Subject: Physics

ABSTRACT

We report the development of a new diffuse reflecting material with measured diffuse reflectivity values as high as 0.9992 at 532 nm, and 0.9969 at 266 nm. These values are, to the author's best knowledge, the highest diffuse reflectivity values ever produced. The material is a high-purity fumed silica, or quartz powder. We demonstrate the application of this new material to several areas of integrating cavity enhanced spectroscopy, including absorption, Raman, and fluorescence spectroscopy. In addition, we demonstrate a new spectroscopic technique based on cavity ring-down spectroscopy using an integrating cavity made of our new diffuse reflector. This technique, which we call integrating cavity ring-down spectroscopy (ICRDS), has tremendous potential for sensitive absorption measurements of low-absorbing samples, even when there is strong scattering. Results for measurements of the absorption coefficient of retinal pigment epithelium cells using this ICRDS technique are also presented. Finally, we discuss the importance of the "wall-time" when considering the temporal response of an integrating cavity. Light reflecting off the inner wall of an integrating cavity actually penetrates into the diffuse reflecting material. Therefore, the light spends some time inside the cavity wall. We measure this wall-time via two independent methods, and show that it can be on the order of several picoseconds.

To my parents,

and Brenda

ACKNOWLEDGEMENTS

I first decided that I wanted to study physics after stumbling across a book about black holes in my high school library. I had always had an interest in science, and particularly in science fiction, but this was the first time I remember thinking that I actually wanted to be a scientist. Some years later (the exact number need not be mentioned), I find myself writing this dissertation. My research area may have diverged radically from those early interests, but I still have the same fascination with science.

It has been my great fortune to have the help of many wonderful people during my time here. My advisor, Dr. Edward Fry, has been an exceptional mentor, and a good friend. His excitement for research and education is both inspiring, and contagious. I'm also indebted to the rest of my committee, Dr. George Kattawar, Dr. George Welch, and Dr. John Bevan, for their time and thoughts regarding my work. I received a tremendous amount of guidance from Erwin Thomas, Jason Caswell, Steve Payne, James Kirby, Tom Weimer, Kavin Morris, and Ron Page. Special mention must go to Bill Merka in the chemistry glass shop. His work and advice have proved invaluable to many of my projects over the years.

Many of my fellow graduate students (both former, and current), have provided tremendous support. My labmates, Joe Musser, David Haubrich, Ellie Figueroa, John Mason, Juana Gomez, Jeff Katz, Xinmei Qu, and Zheng Lu have all been great sources of discussion, assistance and friendship during this work. Glenn Agnolet, Tatiana Erukhimova, Nate Pogue, Matt Cervantes, Lucas Naveira, Jonathan Asaadi, David Maffei, Patrick Noyes, Jim Drachenberg, Kevin Resil, Eunsin Lee, Sergio Degach, Tyler Morrison, Chris OBrien, Anderw Traverso, Karie Melconian,

Brett Hokr, Dawson Nodurft, Tristan Leggett, and Joel Bixler have all been great colleagues and friends. I also need to acknowledge a few others who collaborated, or assisted on some of the work in this dissertation: Dr. Vlad Yakovlev, Dr. Jeffrey Wigle, Dr. Benjamin Rockwell, Gary Noojin, and Chase Winkler.

My parents Thomas and Nancy Cone, have always been an unswerving source of encouragement in everything I have undertaken. I would not be who I am, or where I am today without their love and support. My sister Jennifer, and brother Brian have also always been there for me, and for this I'm eternally grateful.

I am certainly of the persuasion that pets are family, and mine are no exception. I found Rhiannon Emma Paige in Kirksville, Missouri shortly before I finished undergraduate school. She's been with me ever since, and thus has borne witness to the entirety of my graduate career. Zoe came to me through my girlfriend Brenda, and brings a playful, if anxious, spirit to everything she does. Nikko has become such a significant and consistent aspect of my life that it is difficult to imagine how I got along without him. Whether it was walking to the duck pond, going on road trips, or watching the Cardinals win the World Series, Nikko has always been up for it. He was there to help me relax in times of stress, and to help me waste time when I needed to procrastinate. He is as good a friend as anyone could ask for.

I met Brenda shortly before she finished her veterinary school program at Texas A&M. It's now been seven years, and she has gone on to start her own highly successful clinic in Houston. This has been a very challenging and stressful endeavor, and yet she has never failed to be supportive, encouraging, and most of all patient, as I have worked towards finishing my own degree. Somehow during this absurdly busy time, we have also managed to travel, take part in several weddings, and even do the occasional triathlon. She's an amazing companion, and my best friend. I'm truly fortunate to have her, and excited for our future together.

TABLE OF CONTENTS

LIST OF FIGURES

FIGURE Page

LIST OF TABLES

TABLE Page

1. INTRODUCTION*

Materials and surfaces that diffusely scatter light are all around us. In fact, the majority of the light that gets to our eyes is diffusely scattered. We are all familiar with the standard textbook example involving an incoming ray of light incident on a flat mirror. The ray is reflected according to the well known law of reflection, and thus leaves at one, and only one angle. While these specular reflections are certainly important, when it comes to the real world they are more the exception than the rule. Even a highly directional laser beam reflecting off a mirror will produce a noticeable diffuse reflection in addition to the strong specular reflection. This is the reason we can see the spot where the laser strikes the mirror from any viewing angle, and not just the angle for the specular reflection.

The example of the mirror shows that all surfaces produce at least some level of diffuse scattering. However, many surfaces produce no appreciable specular reflections. For these types of surfaces all the reflected light results from diffuse scattering. White paper, or a wall with a matte white paint finish are both examples of good diffuse scatterers. One can easily check this by simply observing such a surface while changing the angle of view and noting that the perceived brightness is nearly constant. In nature we see examples of strong diffuse scattering in clouds, snow, the white coat of a polar bear, and the famous White Cliffs of Dover.

Aside from their abundance in the natural world, diffusely scattering surfaces also have many uses in the laboratory. One of the most notable applications, the integrating cavity, has been used in the fields of optics, radiometry and photometry

*Portions of this chapter are reprinted with permission from "Integrating cavities: temporal response," E.S. Fry, J. Musser, G.W. Kattawar, and P.-W. Zhai, 2006. *Applied Optics*, **45**, Copyright [2006] by Optical Society of America.

for over a century. The theoretical concept was originally conceived of by W. E. Sumpner in 1892, and was then further developed by R. Ulbricht in 1900.[1] Integrating cavities are essentially just cavities with interior walls made or coated with a highly reflective diffuse scattering material. They can be used to measure the total flux from a light source, create uniform light sources, and even to measure the reflectivity of other diffuse reflectors.

1.1 Radiometry Basics

The properties of diffuse reflectors and integrating cavities are typically described in terms of radiometric quantities. With this in mind, we will begin by defining a few basic terms from the field of radiometry. The radiant intensity I, is the radiant power (or flux) per unit solid angle emitted by a source ($^{W}/_{sr}$). This can be expressed as,

$$I = \frac{d\Phi}{d\Omega}, \tag{1.1}$$

where $d\Phi$ is the power emitted into the solid angle $d\Omega$. This definition of intensity is often confused with the more common definition in optics where the intensity is the magnitude of the Poynting vector.

Another useful quantity is the irradiance F, or the radiant power per unit area received by a surface ($^{W}/_{m^2}$). This can be expressed as,

$$F = \frac{d\Phi}{dA}, \tag{1.2}$$

where dA is the area of the surface element. Finally, the radiance L, is the radiant power per unit projected area per unit solid angle leaving a real or imaginary surface ($^{W}/_{sr \cdot m^2}$), and is given by,[2]

$$L = \frac{d^2\Phi}{dA_{proj}d\Omega}. \tag{1.3}$$

Figure 1.1 shows the various geometrical quantities involved in the definition of radiance for a pencil of radiation. The radiance is of particular importance in radiometry and radiative transfer theory because it is a conserved quantity for light propagating through a lossless system.

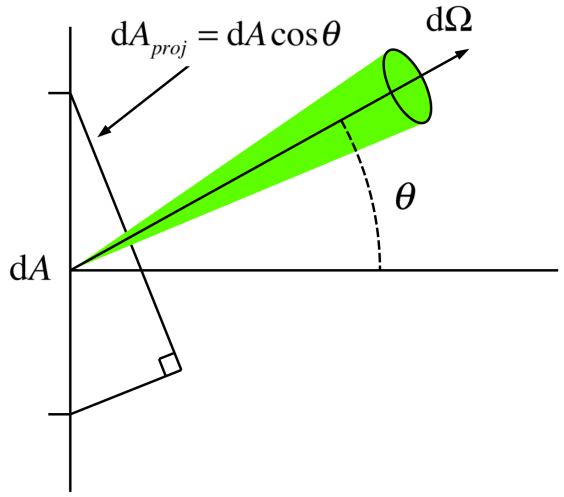

Figure 1.1: Diagram of the geometrical quantities involved in the definition of radiance.[2]

1.2 The Radiative Transfer Equation

The radiation field within a medium can experience absorption, scattering, or be added to via emission. Radiative transfer theory deals with how this radiation propagates through such a medium. The fundamental relation describing this propagation is the radiative transfer equation (RTE). In general, the RTE would have to

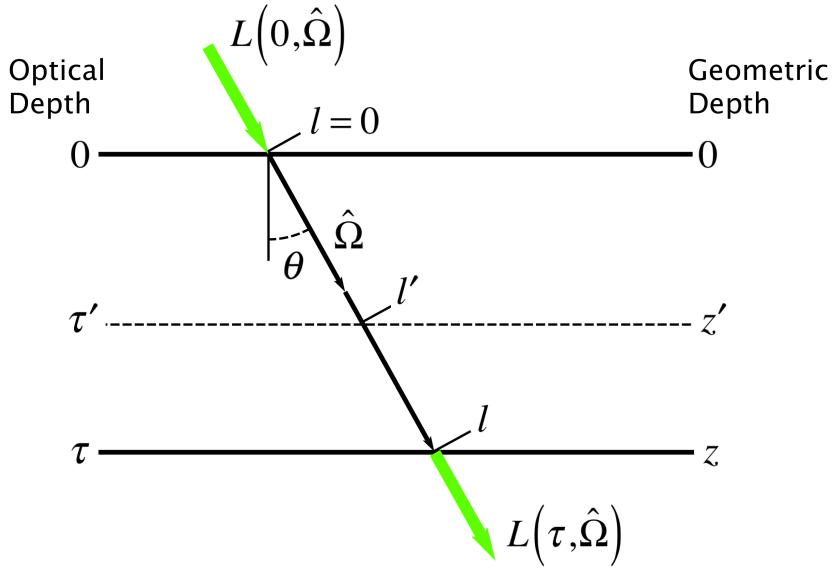

Figure 1.2: Diagram showing the progression of radiation through a medium.[3]

account for changes in mediums (i.e. interfaces), as well as changes in the index of refraction within a given medium. For our purposes it will be sufficient to restrict ourselves to the case of a single homogenous medium with a constant index of refraction. Figure 1.2 depicts the propagation of an incident radiance, $L(0,\hat{\Omega})$, through a medium with a geometric depth given by z, where the vector $\hat{\Omega}$ is a unit vector along the direction of the radiance. A useful alternative to using the geometric depth is a quantity known as the *optical depth*, τ. This is defined as,

$$d\tau = c(z)dz, \tag{1.4}$$

where *c(z)* is the attenuation coefficient, or the sum of the absorption coefficient *a(z)*, and the scattering coefficient *b(z)*. In other words, the optical depth represents how opaque or transparent a medium is to radiation traveling through it. Using this we

can write the RTE for our situation as follows:

$$\mu \frac{dL(\tau, \hat{\Omega})}{d\tau} = -L(\tau, \hat{\Omega}) + \omega_0(\tau) \int_{\Omega'} L(\tau, \hat{\Omega}')\rho(\tau; \hat{\Omega}, \hat{\Omega}')d\Omega' + \frac{1}{c(\tau)} S(\tau, \hat{\Omega}), \qquad (1.5)$$

where μ is the cosine of the angle of incidence (see Fig. 1.2), $\omega_0(\tau)$ is the single-scattering albedo, $\rho(\tau; \hat{\Omega}, \hat{\Omega}')$ is the scattering phase function, and $S(\tau, \hat{\Omega})$ is a source term.[3–5] The single-scattering albedo is defined as $\omega_0(\tau) = {}^{b(\tau)}/_{c(\tau)}$, and can be thought of as the probability that a photon will be scattered, rather than absorbed. An $\omega_0 = 1$ indicates that all of the attenuation in the medium is due to scattering; while an $\omega_0 = 0$ indicates all the attenuation is due to absorption. The scattering phase function gives the angular distribution of the scattered photons and obeys the normalization condition

$$\frac{1}{4\pi} \int_{\Omega'} \rho(\tau; \hat{\Omega}, \hat{\Omega}')d\Omega' = 1. \qquad (1.6)$$

In order to gain more insight into the RTE we will take a closer look at each of its terms. The left-hand side of Eq. 1.5 is simply a derivative giving the change in the radiance as a function of the optical depth. On the right-hand side, the first term is simply the negative of the radiance, indicating its exponential decay with increasing depth due to attenuation within the medium. The second term shows how much radiance is gained via elastic scattering in the direction $\hat{\Omega}$. Finally, the third term accounts for any radiance gained due to inelastic scattering, or emission in the direction $\hat{\Omega}$. Thus, we see that the RTE is simply stating that the change in the radiance as it travels through a medium is the sum of the losses due to attenuation, and the gains due to scattering and emission.

For much of this work we will be interested in various methods of measuring absorption coefficients for different mediums. We can use the RTE to get a physical picture of what an absorption coefficient represents. If we restrict ourselves to the simple case where scattering is negligible (i.e. $\omega_0 = 0$), and there are no sources of radiation (i.e. $S = 0$), then Eq. 1.5 reduces to,

$$\mu \frac{dL(\tau, \hat{\Omega})}{d\tau} = -L(\tau, \hat{\Omega}). \tag{1.7}$$

This is a general form of the well-known Beer, Lambert, Bouguer Law. We can further simplify this expression by introducing the *optical path length* l, defined as,

$$dl = \frac{d\tau}{\mu}. \tag{1.8}$$

Using this we can write Eq. 1.7 as,

$$\mu \frac{dL}{d\tau} = \frac{dL}{dl} = -L, \tag{1.9}$$

which has a solution of the form,

$$L(l) = L(0)e^{-l}. \tag{1.10}$$

For the case of a homogenous medium with normal incidence (i.e. $\theta = 0$), we have $c(z) = a(z) = a$ and $\mu = 1$. This means that the optical path length can be expressed as,

$$l = \frac{1}{|\mu|} \int_0^z c(z')dz = a \int_0^z z'dz = az, \tag{1.11}$$

and thus our solution, Eq. 1.10, becomes,

$$L(z) = L(0)e^{-az}. \tag{1.12}$$

This is the more familiar form of the Beer, Lambert, Bouguer Law, and shows that the radiance in a purely absorbing, homogenous medium will exponentially decay with increasing geometric depth.[3] Equation 1.12 also makes the meaning of an absorption coefficient very clear. That is, $1/a$ is the distance that light must travel through an absorbing medium for 63% of the initial light to be absorbed.

1.3 Diffuse Reflector Basics

The basic idea of diffuse and specular reflections was mentioned at the beginning of this chapter, but now we will cover this concept in more detail. Figure 1.3(a) shows several incoming rays of light undergoing specular reflection at a surface. In this case the angle between the incident ray and the surface normal θ_i, is equal to the angle between the reflected ray and the surface normal θ_r. Figure 1.3(b) shows several light rays scattering off a diffuse reflecting surface. In this case there is no relation between the angle of incidence and the angle of reflection for a given photon. Instead we see incoming light leaving the surface at all viewing angles.

If we consider a microscopic view of a diffuse reflecting surface we can gain some insight as to why light from a single incoming direction is scattered into many directions. Figure 1.4 shows a simplified microscopic model of a diffuse reflecting surface. In this model the individual particles, or aggregated particles that make up a real diffuse reflecting wall are approximated by irregular polygons that act as partially reflecting surfaces. An incoming ray of light will be be partially reflected off of each surface it comes into contact with, but the remaining light will be transmitted, and thus continues in its original direction of propagation. The primary reflections (or scattering) from each interface can in turn produce secondary reflections, and so on.

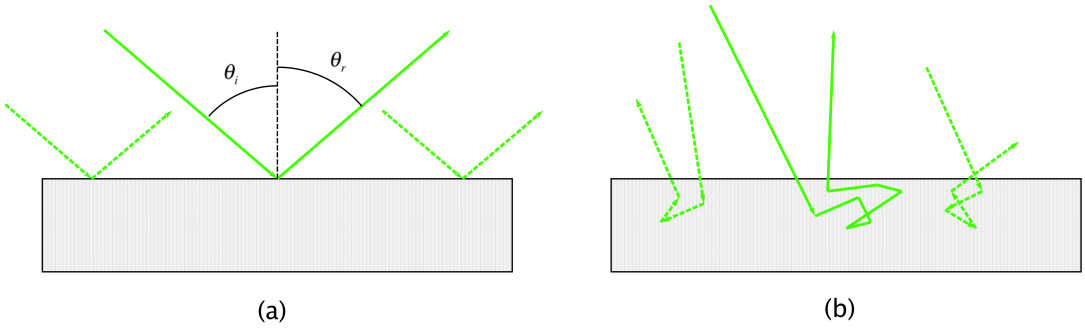

Figure 1.3: Diagram depicting incoming light rays reflecting off (a) a specular reflecting surface, and (b) a diffuse reflecting surface.

In other words, individual photons can be scattered just once, or multiple times before they are able to leave the surface as reflected light. These multiple scattering events, combined with the random orientation of the scattering surfaces leads to the diffuse nature of the reflected light.

Diffuse reflectors are typically characterized by two properties: the materials reflectance, and its bidirectional reflectance distribution function (BRDF).[6] The reflectance is simply the ratio of the reflected radiant power to incident radiant power. The BRDF, as proposed by Nicodemus *et al.*, is defined as the ratio of the outgoing radiance of a sample to the incoming irradiance on the sample, for a given direction of incidence, (θ_i, ϕ_i), and direction of scatter, (θ_s, ϕ_s).[7] The geometry for this is represented pictorially in Fig. 1.5.

The BRDF can be expressed in terms of the incoming radiant power P_i on a sample, and the scattered radiant power P_s, as follows:

$$BRDF(\theta_s, \phi_s) \equiv \frac{radiance(\theta_s, \phi_s)}{irradiance} = \frac{\left({}^{P_s}/_{Acos(\theta_s)d\Omega}\right)}{{}^{P_i}/_{A}} = \frac{P_s}{P_i cos(\theta_s) d\Omega}, \tag{1.13}$$

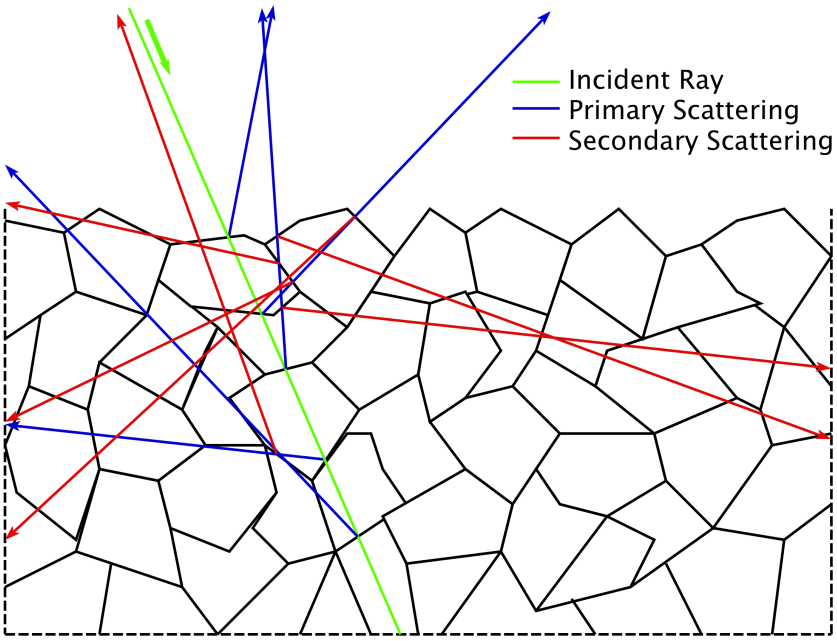

Figure 1.4: Generic diagram depicting a simplified model of a diffuse reflecting surface at the microscopic level.

where A is the area of the sample. The scattered power is directed into a solid angle $d\Omega$ with a direction designated by the unit vector $\hat{\Omega}$. Although the BRDF is a function of both θ_s and ϕ_s, symmetry typically allows the azimuthal dependence to be neglected.

An important special class of diffuse reflector is that of a Lambertian reflector, where incoming light from any single direction is reflected such that the outgoing radiance is the same in all directions. This is equivalent to saying that the outgoing radiant intensity varies with the cosine of the angle θ between the receiver and the surface normal of the reflecting surface.[2] This is expressed as,

$$I = I_0 cos\theta_s. \tag{1.14}$$

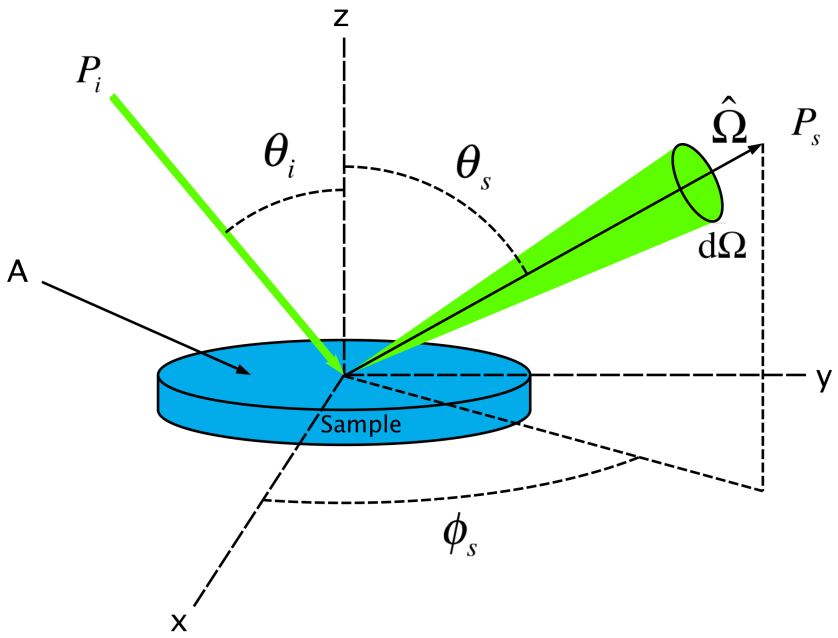

Figure 1.5: Geometry for BRDF.

If we consider the BRDF for the case of a Lambertian reflecting sample, then Eq. 1.13 becomes,

$$BRDF_{Lambetian} = \frac{P_s}{P_i cos(\theta_s) d\Omega} = \frac{\rho P_i cos(\theta_s)}{P_i cos(\theta_s) d\Omega} = \frac{\rho}{d\Omega}, \tag{1.15}$$

where ρ is the reflectivity of the sample. In other words, the BRDF for an ideal Lambertian reflector is a constant value. By contrast, an ideal specular reflection is represented by a delta function in the BRDF. While ideal Lambertian reflectors are theoretical, and thus do not exist in nature, we will see later that some exhibit nearly Lambertian behavior.

1.4 Integrating Cavity Basics

We will finish up this chapter by going over some of the basic aspects of integrating cavities. Figure 1.6 shows a diagram of the cross section of a generic spherical integrating cavity. The inner wall is made of a diffuse reflector material of high reflectivity, while the composition of the outer supporting wall varies and is often irrelevant to the cavities function. Ports in the cavity allow light to be coupled into the cavity, as well as out of the cavity for detection.

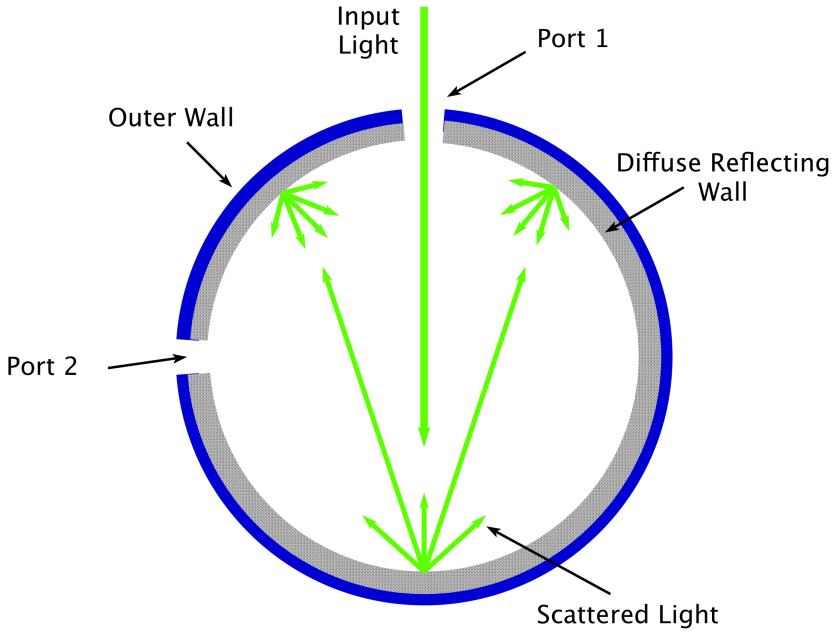

Figure 1.6: Cross section of a generic integrating cavity.

For an integrating cavity with nearly Lambertian walls, any light that enters the cavity will scatter off the diffuse reflecting wall such that the outgoing radiance is the

same in all directions. This scattered light will in turn strike other portions of the inner cavity wall, and will again be scattered in a nearly Lambertian manner. The result of all this is that after several reflections, the irradiance is essentially constant over the cavity wall. Thus, integrating cavities are said to spatially integrate the input radiant flux.[1,8]

Integrating cavities have numerous applications in the fields of optics, radiometry and photometry. Common uses include: measuring the total radiant flux from sources such as lamps and lasers, measuring the reflectance and transmittance of scattering materials, and creating uniform sources of light.[8] In addition to this, P. Elterman demonstrated that an integrating cavity could be used to measure the absorption coefficient of a sample that is placed inside the cavity.[9] This method of absorption spectroscopy will be discussed in detail in Ch. 3.

1.5 Temporal Response of an Integrating Cavity

Much of what follows in this section will be based on the temporal response of an integrating cavity to the input of a short pulse of light. In particular, we want to know how the radiation inside the cavity will decay with respect to time. The derivation for the temporal response of an integrating cavity is described in detail by Fry *et al.*, and is partially reproduced here.[10]

Consider an integrating cavity with walls made of a Lambertian diffuse reflecting material. We want to determine the amount of time it takes the irradiance on the cavity walls to decrease to $1/e$ of its initial value. We begin by defining the following variables:

E = the irradiance on the cavity wall.

ρ = the average reflectivity of the Lambertian surface of the cavity, $0 \leq \rho \leq 1$.

τ = the time constant for the cavity.

n = the average number of reflections in time τ.

$\bar{d}$ = the average distance between reflections at the cavity wall.

$\bar{t}$ = the average time between reflection at the cavity wall.

c = the speed of light.

If we assume that the irradiance incident on the cavity wall E_I, decays exponentially, then

$$E_I(t) = E_0^{'} e^{-t/\tau}, \tag{1.16}$$

where $E_0^{'}$ is the irradiance incident on the wall at time $t = 0$. The irradiance leaving the cavity wall at time t, $E_L(t)$, is given by,

$$E_L(t) = \rho E_0^{'} e^{-t/\tau}. \tag{1.17}$$

If we choose the zero of time to be the instant of the first reflection, then at the $(n+1)$th reflection we will have $t = n\bar{t} = \tau$. This gives,

$$E_I(\tau) = E_0 \rho^n, \qquad E_L(\tau) = E_0 \rho^{n+1}. \tag{1.18}$$

We can also express E_I and E_L at time $t = \tau$ using Eqs. 1.16 and 1.17, which gives

$$E_I(\tau) = E_0^{'} e^{-1}, \qquad E_L(\tau) = \rho E_0^{'} e^{-1}. \tag{1.19}$$

By combining Eqs. 1.18 and 1.19 we find,

$$n = \frac{\tau}{\bar{t}} = -\frac{1}{ln\rho}. \tag{1.20}$$

By noting that $\bar{t} = {}^{\bar{d}}/_{c}$ we can rewrite Eq. 1.20 as,

$$\tau = -\frac{1}{ln\rho}\frac{\bar{d}}{c}. \tag{1.21}$$

In the prior derivation we started with the assumption that $E_I(t)$ took the form of an exponential decay. We can avoid this assumption by starting with a Taylor expansion of $E_I(t+\bar{t})$ about the time t. Thus, we have

$$E_I(t+\bar{t}) = E_I(t) + \sum_{k=1}^{\infty} \frac{\bar{t}^k}{k!}\frac{d^k E_I(t)}{dt^k}. \tag{1.22}$$

If we make a change of variables, $\xi = {}^{t}/_{\bar{t}}$, then Eq. 1.22 becomes

$$E_I(t+\bar{t}) = E_I(t) + \sum_{k=1}^{\infty} \frac{1}{k!}\frac{d^k E_I(t)}{d\xi^k}. \tag{1.23}$$

Noting that $E_I(t+\bar{t}) - E_I(t) = E_I(t)(1-\rho)$, Eq. 1.23 becomes

$$\sum_{k=1}^{\infty} \frac{1}{k!}\frac{d^k E_I(t)}{d\xi^k} + E_I(t)(1-\rho) = 0. \tag{1.24}$$

Equation 1.24 is a homogenous infinite-order differential equation with constant coefficients. This suggests solutions of the form $exp(\gamma\xi)$, where γ is a parameter. If we substitute this into Eq. 1.24 we find the characteristic equation,

$$\sum_{k=1}^{\infty} \frac{1}{k!}\gamma^k + (1-\rho) = 0. \tag{1.25}$$

Replacing the summation in Eq. 1.25 by an exponential, we have

$$e^{\gamma} - \rho = 0. \tag{1.26}$$

Thus, the solution to Eq. 1.24 is given by

$$E_I(t) = E_0^{'} e^{\gamma t/\bar{t}} = E_0^{'} e^{tln\rho/\bar{t}}. \tag{1.27}$$

Comparing Eq. 1.27 to $E_I(t) = E_0 exp\,(^{-t}/_{\tau})$ yields

$$\tau = -\frac{\bar{t}}{ln\rho}, \tag{1.28}$$

which is in agreement with Eq. 1.21.

Fry *et al.* showed that Monte Carlo simulations of the decay of the radiation inside an integrating cavity are in excellent agreement with the model derived above. However, the model and the simulations begin to deviate for low reflectivities. For example, a sphere with a diameter of 2 (the unit of distance is the cavity radius R) was simulated with the Monte Carlo simulation. The simulation calculates the cavity time constant τ, for a given reflectivity ρ. These values were compared to $\tau's$ calculated using the simple model given in Eq. 1.21. For the case of $\rho = 0.50$, the τ calculated from Eq. 1.21 is 3.9% off the value calculated from the physically correct Monte Carlo model. However, for $\rho = 0.9$ the error drops to only 0.65%, and for $\rho = 0.99$ it is only 0.06%.[10]

1.6 The Average Distance Between Reflections in an Integrating Cavity

In the previous section we derived a simple model for calculating the decay constant of an integrating cavity, and we found that a crucial component of that model is the average distance between reflections, $\bar{d}$. Naturally, we would like to be able to calculate $\bar{d}$ for a given cavity geometry. Fry *et al.* derived $\bar{d}$ for special cavity ge-

ometries like, spherical, cylindrical, spherical shell, and any cavity formed by planes tangent to an inscribed sphere. In addition to all these, they also derived a simple expression for a cavity of arbitrary geometry. This derivation is reproduced here.[10]

We begin by considering a cavity of arbitrary shape with a volume V, and surface area S. In addition, assume that the cavity contains n photons per unit volume, and that they are distributed such that the radiance $L(\mathbf{r}, \Omega)$, is constant throughout the cavity. Figure 1.7 shows an infinitesimal cylindrical volume inside this cavity, where one end of the cylinder is an element of area dS, on the cavity wall. The number of photons in the cylinder is given by $n(c\delta t)(\mu \mathrm{d}S)$, where $\mu = cos\theta$.

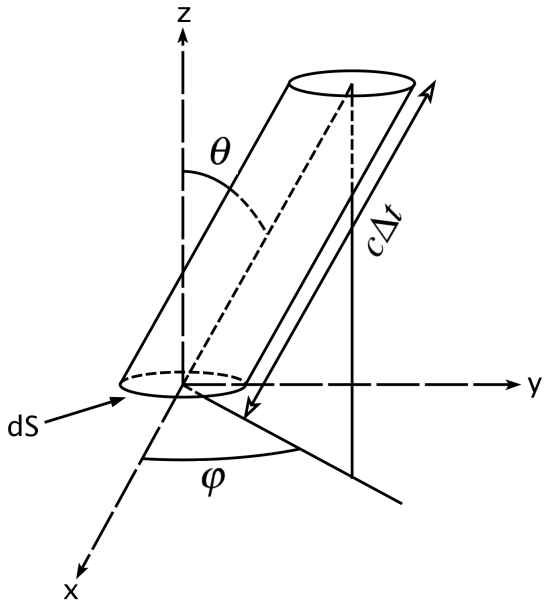

Figure 1.7: Diagram depicting the photon flux incident on the cavity wall.

The photon propagation directions are uniformly distributed over a 4π solid angle

for any point inside the cavity volume. Thus the fraction of photons propagating in the direction (θ, ϕ) in the solid angle $\mathrm{d}\Omega = \mathrm{d}\mu\mathrm{d}\phi$ is given by

$$p_u = \frac{1}{4\pi}\mathrm{d}\mu\mathrm{d}\phi. \tag{1.29}$$

This means that the number of photons in the cylinder depicted in Fig. 1.7 that are traveling in the direction (θ, ϕ) in an infinitesimal solide angle $\mathrm{d}\mu\mathrm{d}\phi$ is

$$\mathrm{d}N_u = n(c\Delta t)(\mu \mathrm{d}S)\left(\frac{1}{4\pi}\mathrm{d}\mu\mathrm{d}\phi\right) = \left(\frac{nc}{4\pi}\right)(\mu\mathrm{d}\mu\mathrm{d}\phi)\mathrm{d}S\mathrm{d}t. \tag{1.30}$$

Because there is no photon-photon scattering within the volume, all of these photons must have been supplied by reflection from the cavity surface.

We now turn our attention to the photons that are reflected from the cavity surface. The total number of photons in the cavity is nV and, on average, all of these photons will be incident on the wall in a time $\bar{d}/c$, where $\bar{d}$ is the average distance between collisions with the cavity wall. This means that the total number of photons incident on the cavity wall per unit time per unit area is

$$\frac{nV}{(\bar{d}/c)\,S} = \frac{nc}{\bar{d}}\frac{V}{S}. \tag{1.31}$$

If we assume that the surface is Lambertian (i.e. constant $L(\mathbf{r}, \Omega)$), then the probability that photons will be reflected from the surface at an angle θ to the normal is proportional to $\mu = cos\theta$ and is independent of the angle of incidence. Thus, the probability that photons will be reflected in the direction (θ, ϕ) into an infinitesimal solid angle $\mathrm{d}\Omega = \mathrm{d}\mu\mathrm{d}\phi$ is given by

$$p_r = \frac{1}{\pi}\mu\mathrm{d}\mu\mathrm{d}\phi, \tag{1.32}$$

where the $\frac{1}{\pi}$ is a normalization factor. Therefore, photons reflected in the direction (θ, ϕ) into the infinitesimal solid angle $\mathrm{d}\mu\mathrm{d}\phi$ from the element of cavity surface area $\mathrm{d}S$ in time $\mathrm{d}t$ are contained in the cylinder depicted in Figure 1.7. Combining Eqs. 1.31 and 1.32, we find that the number of these photons is given by,

$$\mathrm{d}N_r = \left(\frac{nc}{\bar{d}}\frac{V}{S}\right)\left(\frac{1}{\pi}\mu\mathrm{d}\mu\mathrm{d}\phi\right)\mathrm{d}S\mathrm{d}t = \left(\frac{nc}{\pi\bar{d}}\frac{V}{S}\right)(\mu\mathrm{d}\mu\mathrm{d}\phi)\,\mathrm{d}S\mathrm{d}t. \tag{1.33}$$

Maintaining constant radiance throughout the cavity requires that $\mathrm{d}N_u = \mathrm{d}N_r$. Comparing Eqs. 1.30 and 1.32, and noting that they have the same dependences on θ and ϕ leads to the expression

$$\bar{d} = 4\frac{V}{S}. \tag{1.34}$$

This provides us with a completely general result for $\bar{d}$ that is independent of the shape of the cavity. Since Eq. 1.34 depends only on the volume-to-surface ratio, it becomes trivial to calculate $\bar{d}$ for many simple cavity geometries. For example, it is easy to show that both a sphere of diameter D, and a right circular cylinder with diameter D, and height $H = D$ have a $\bar{d}$ given by

$$\bar{d} = \frac{2}{3}D. \tag{1.35}$$

This result agrees with more complicated geometry-specific results for spherical and cylindrical cavities.[10] Both Eqs. 1.34 and 1.35 will be used extensively throughout this dissertation.

2. A NEW DIFFUSE REFLECTOR

2.1 Examples of Current Diffuse Reflecting Materials

There are a large variety of high-quality diffuse reflectance materials available for use in integrating cavities, and other applications. Barium sulfate based powders and coatings, such as Eastman Kodak 6080, have been in use for several decades.[11,12] These coatings can easily be applied to most surfaces, making them ideal for integrating cavities. A modern example, the barium sulfate based material Spectrareflect®, provides a reflectance of over 97% throughout the visible and near-infrared portion of the spectrum.[6] However, the reflectance of all these barium sulfate materials drops considerably in the UV, with Spectrareflect's reflectance at 250 nm being only 94%.*

Spectralon® is the current industry leader in diffuse reflectance over the UV-VIS-NIR portion of the spectrum.[6] The material is composed of a powder of polytetrafluoroethylene (PTFE), that is then pressed and sintered into machinable blocks. Spectralon has a reflectance of 99.0-99.2% across the visible spectrum, but much like Spectrareflect, this value goes down in the ultraviolet, being only 95.0% at 250nm.[6] Spectralon is also susceptible to photolytic degradation if it is allowed to come into contact with contaminants in water, tubing plasticizers, epoxy components, or other sources.[14] In addition to this, Goodman *et al.* and Hope *et al.* have shown the degradation of Spectralon samples under long-term exposure to high and low levels of ultraviolet irradiation without the presence of these contaminants.[15,16] However,

*Strictly speaking, the terms reflectance and reflectivity are not equivalent. Reflectance is typically used in reference to thin layers, and can vary with surface thickness, while reflectivity applies to thick reflecting objects. In this sense, reflectivity can be thought of as the limit of the reflectance for a material as the sample thickness increases. Another common usage regards reflectivity as the property of a pure material, and reflectance as the property of a particular sample.[1,13] In this work the two terms will be used interchangeably, except for cases when doing so would lead to confusion, or when citing specific source materials.

there have been studies that show that this degradation can be mitigated, or even eliminated by a vacuum bakeout procedure.[17,18]

2.2 Simple Model of a Highly Reflecting Wall

By considering the light reflecting off a simple air-glass interface, we can gain some understanding of how one might construct a high efficiency diffuse reflecting wall. Figure 2.1 shows a single plate of glass surrounded on both sides by air in front of a back surface with reflectivity η. The reflectivity at the air-glass interface is ρ, and the absorption in the glass is assumed to be negligible. Let i_n be the intensity of light at the n^{th} location, where the location order and direction are as shown in Fig. 2.1. With the initial incident intensity given as i_0, the remaining intensities are given by the following set of equations:

$$i_1 = i_0\rho + i_3(1-\rho), \tag{2.1}$$

$$i_2 = i_3\rho + i_0(1-\rho), \tag{2.2}$$

$$i_3 = i_2\rho + i_5(1-\rho), \tag{2.3}$$

$$i_4 = i_5\rho + i_2(1-\rho), \tag{2.4}$$

$$i_5 = i_4\eta. \tag{2.5}$$

These simultaneous equations can be solved for the total reflected light $R = {}^{i_1}\!/_{i_0}$,

$$\text{1 plate of glass} \qquad R = \frac{\eta + 2\rho - 3\eta\rho}{1 + \rho - 2\eta\rho}. \tag{2.6}$$

Figure 2.2 shows this model extended to the case of N plates separated by air gaps. The ordering and direction scheme for the intensities is the same as the case for one plate. Thus, the intensity leaving the N^{th} plate is i_{4N}, and the intensity of light incident from above on the N^{th} plate is i_{4N+1}, etc.

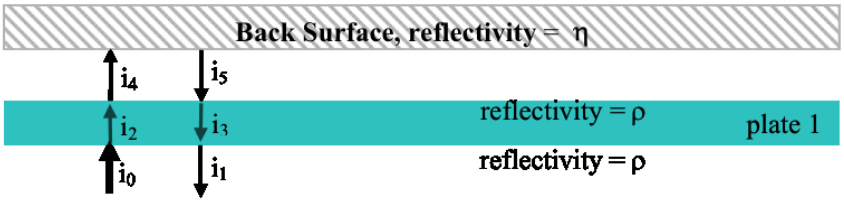

Figure 2.1: Geometry for calculating the reflectivity of 1 plate.

Using Fig. 2.2, and following the same method used above for 1 plate, we find the following solutions:

$$\text{2 plates of glass} \qquad R = \frac{\eta + 4\rho - 5\eta\rho}{1 + 3\rho - 4\eta\rho}. \tag{2.7}$$

$$\text{3 plates of glass} \qquad R = \frac{\eta + 6\rho - 7\eta\rho}{1 + 5\rho - 6\eta\rho}. \tag{2.8}$$

$$\text{N plates of glass} \qquad R = \frac{\eta + 2N\rho - (2N+1)\eta\rho}{1 + (2N-1)\rho - 2N\eta\rho}. \tag{2.9}$$

Some insight can be gained by considering some special test cases of Eq. 2.9. If $N = 0$ (i.e. 0 glass plates) the reflectivity is simply η, or the reflectivity of the back surface. If $\rho = 0$ the reflectivity is once again η. Finally, if either ρ or $\eta = 1$ the reflectivity goes to 1. These results are all in agreement with the expectations for such a setup.[†]

The more interesting case is when N grows large for a fixed value of ρ. Figure 2.3 shows the reflectivity of a stack of plates with $\rho = 0.04$ (a typical value for an air-glass interface) for various values of η. It can be seen that as N grows large, η has

[†]It should be noted that a similar result was obtained by Stokes in 1862.[19]

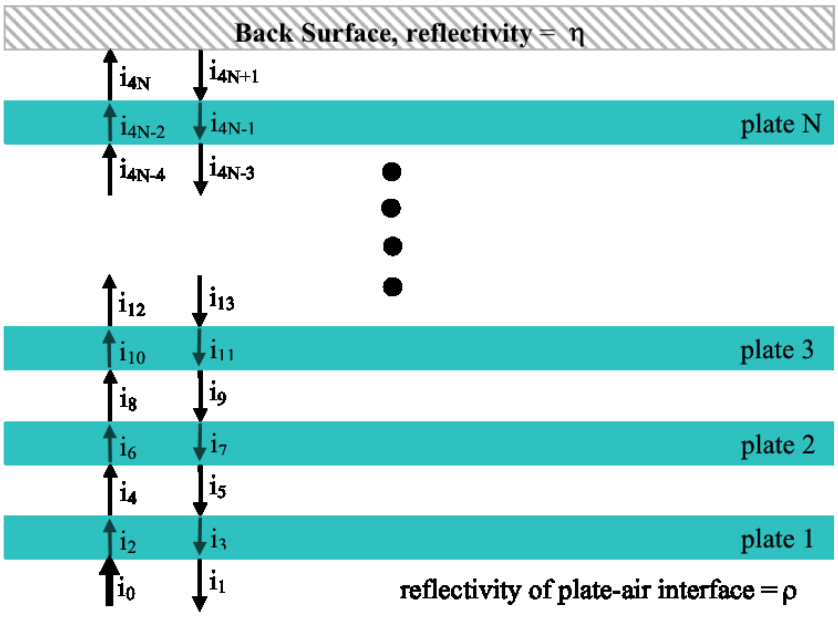

Figure 2.2: Geometry for calculating the reflectivity of N plates.

little effect on the reflectivity of the stack. If we set $\eta = 0$ and $\rho = 0.04$, then the reflectivity of the stack reaches 0.999 with an N of approximately 12,000 (see Fig. 2.4). Thus, very high reflectivities can be reached with a system made up only of interfaces of relatively low reflectivity. Of course, it is completely impractical to build a stack of 12,000 glass plates, but micron sized particles, or powders could easily allow one to achieve this number of interfaces for a wall of modest thickness.

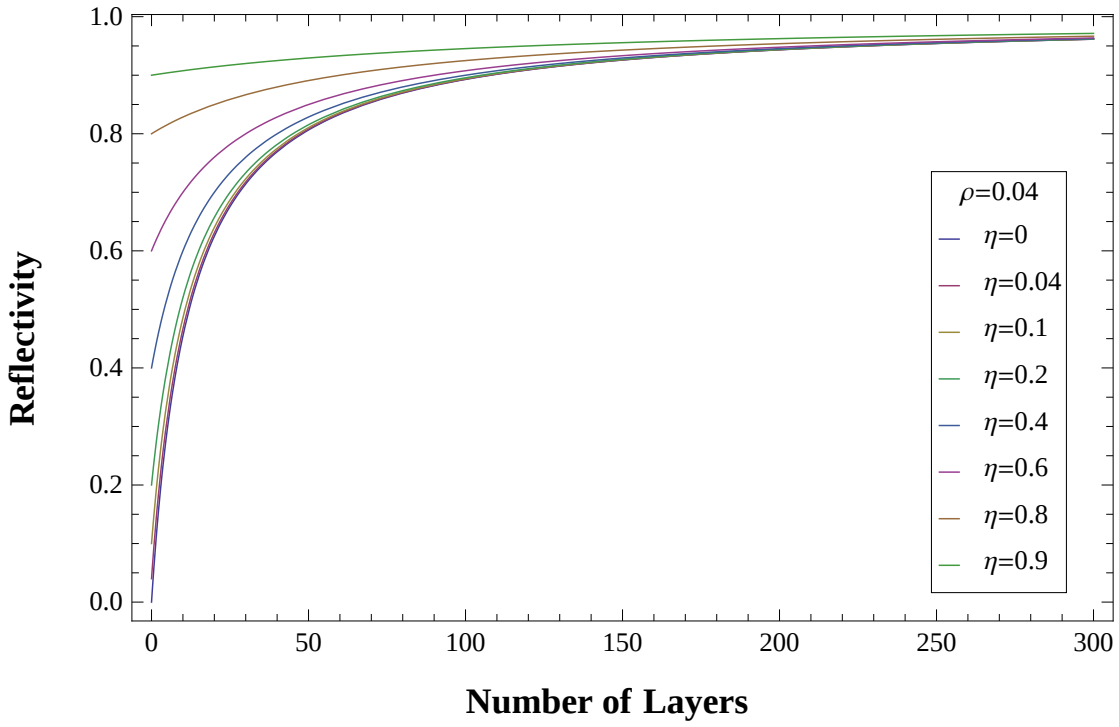

Figure 2.3: Plot showing the total reflectivity of a stack of glass plates vs. the number of plates in the stack for an air-glass interface of reflectivity $\rho = 0.04$. The various colors represent different values of the background reflectivity, η.

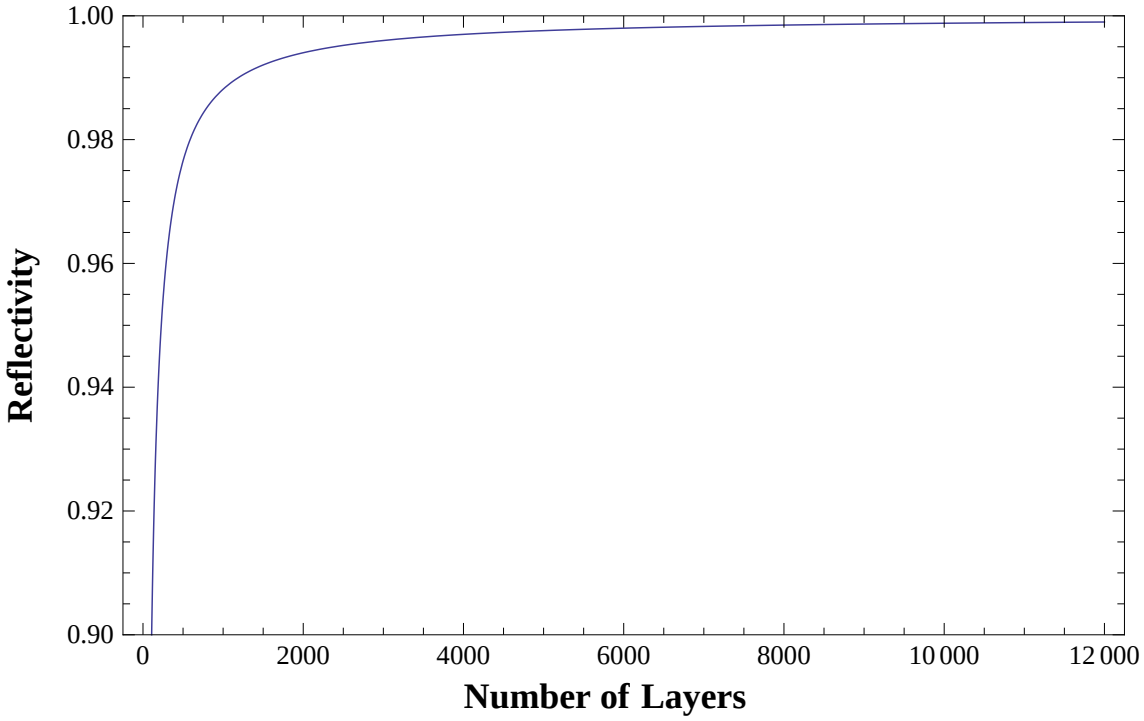

Figure 2.4: Plot showing the total reflectivity of a stack of glass plates vs. the number of plates in the stack for an air-glass interface of reflectivity $\rho = 0.04$.

2.3 A New Diffuse Reflector

We have developed a new diffuse reflecting material for use in integrating cavity applications in the ultraviolet, visible and near-infrared portions of the spectrum. The material is a fumed silica, or quartz powder, and is based on the line of hydrophilic Aerosil® products produced by Evonik Industries in Essen, Germany. Several products from this line have been tested, including Aerosil 380, Aerosil 90, and Aerosil EG50. The number attached to each name indicates the specific surface area (m^2/g) for the particular material. Average particle sizes are approximately 40 nm, but these individual particles are not found alone. Instead the material forms aggregates of partially fused particles (see Fig. 2.5(a)). These aggregates can then form larger agglomerate particles that can be several microns across (see Fig. 2.5(b)).[20,21]

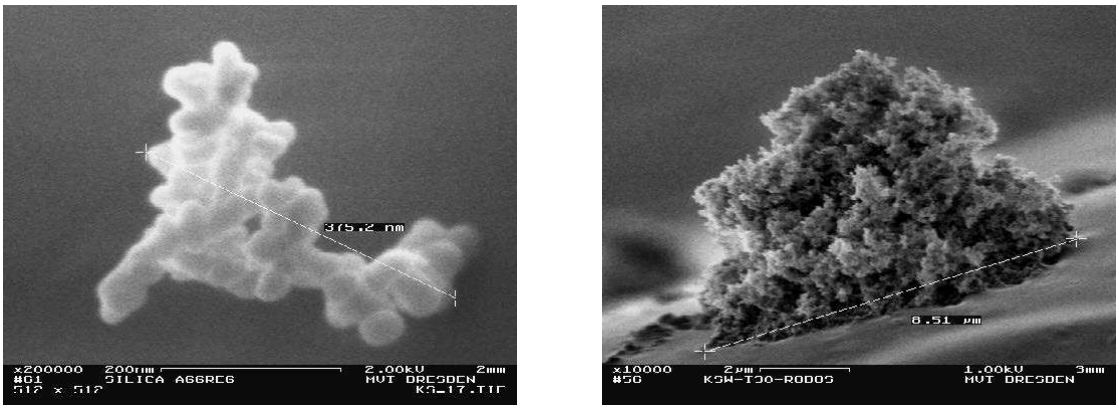

(a) (b)

Figure 2.5: SEM image of (a) a fumed silica aggregate particle, and (b) an agglomerate particle.[20]

If we recall the discussion in the previous section about highly reflecting walls

made of stacks of air-glass interfaces we can immediately see that these fumed silica particles are an excellent candidate to make such a wall. The micron size scale of the agglomerate particles means that the required 12,000 interfaces for a reflectivity of 0.999 could be reached with a wall thickness of only a few cm. Of course, a wall made up of such particles would not produce the type of retro-reflections depicted in Fig. 2.2. The light would instead be diffusely scattered at the various air-quartz interfaces due to the random orientation of the individual particles. This means that we should expect a wall made of this quartz powder to be a good diffuse reflector.

2.4 Relative Reflectivity Measurements

Early attempts to gauge the reflectivity of a sample of packed fumed silica involved comparing it to a known diffuse reflector, Spectralon. Figure 2.6 shows the basic setup used in these experiments. The individual samples were rotated under a port in an integrating cavity. A 532 nm laser was directed through a second port onto the sample at an angle of approximately 8° from the surface normal. The irradiance on one of the cavity walls was sampled with a Hamamatsu 1P21 photomultiplier tube through a third port that was shielded from direct reflections by a baffle. Figure 2.7 shows the results from one of these tests. The small peaks on each side of the data for the powder samples are the result of the specular reflections from the metal ring that held those samples. The data clearly shows that both the Aerosil 90 and the Aerosil EG50 fumed silica powders outperformed the Spectralon sample.[22]

Figure 2.8 shows a histogram of the results from several of these relative reflectivity tests. The plot has been scaled such that the Spectralon sample used as the reference has a reflectivity of unity. We see that nearly all of the quartz powder samples perform better than the Spectralon sample. The sample labeled "Pegasus" is another type of pure silica powder produced by Pegasus Glassworks Incorporated

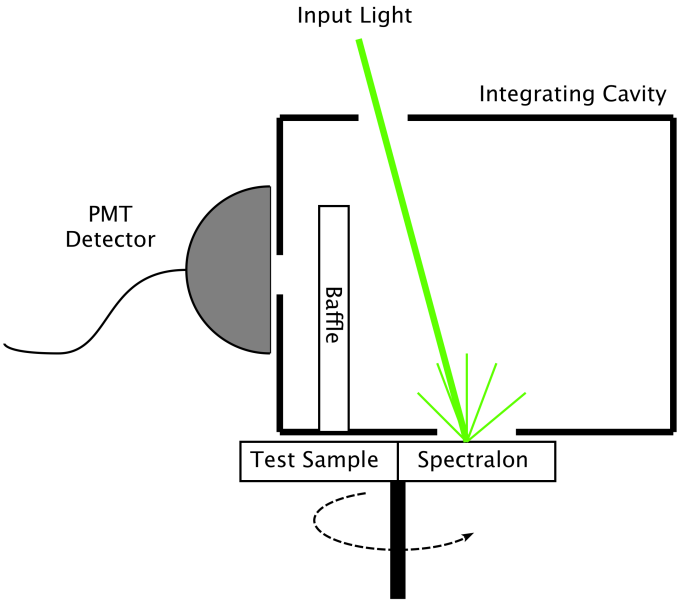

Figure 2.6: Diagram showing the basic setup for the relative reflectivity tests.[22]

in Sturbridge, MA.

Figure 2.7 also shows data for two "baked" samples. It was mentioned earlier in Sec. 2.3 that the fumed silica is hydrophilic, and that the base particles have a large surface to mass ratio. Thus contamination due to trapped water is a serious concern. It is easy to see why trapped water, or any other source of contamination, could be an issue if we recall our model for a highly reflecting wall presented in Sec. 2.2. We made the assumption that the absorption in the glass plates was negligible. Clearly, this would not be true if there is a contaminant in the powder that absorbs in the spectral region of interest. In addition, anything that reduces the number of air-quartz interfaces (i.e. large amounts of trapped water) will also hinder the reflectivity of the wall. Therefore, the powder was baked before being used in order to mitigate any possible contamination. It is easy to see from Fig. 2.7 that the baked

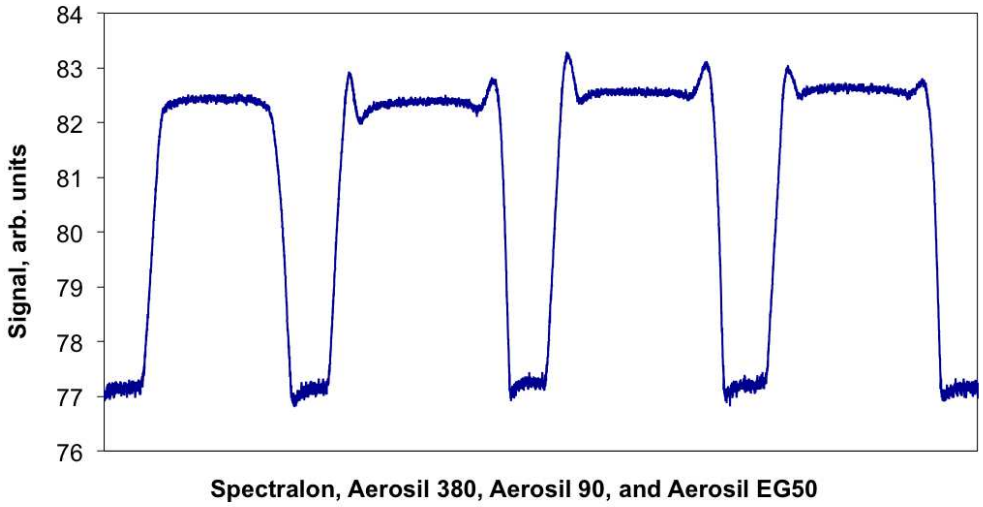

Figure 2.7: Screenshot of the oscilloscope output showing the results of the relative reflectivity tests.[22]

samples outperformed the unbaked samples, with the baked Aerosil EG50 being the best overall. A more detailed discussion of the baking process, and other preparation and handling concerns is given later in this chapter.

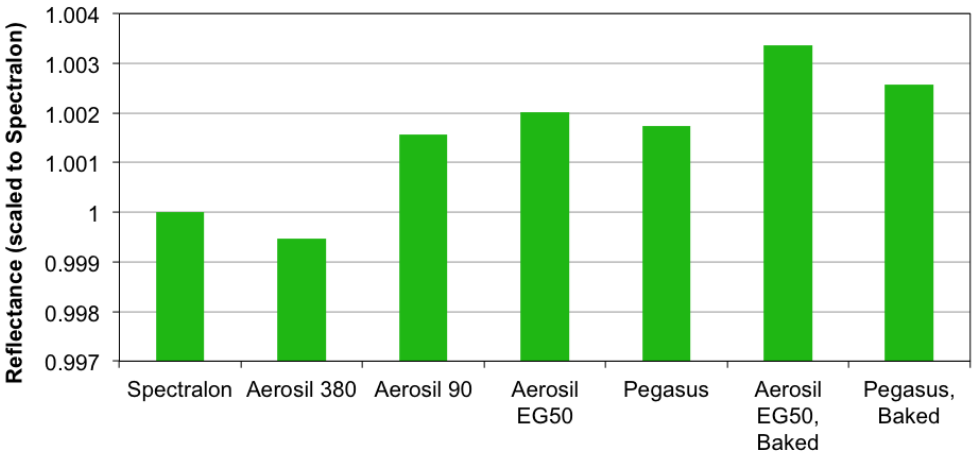

Figure 2.8: Histogram of the relative reflectivities for various fumed silica powders. The plot is scaled such that Spectralon has a reflectivity of unity.[22]

2.5 BRDF Measurements

Recall from Sec. 1.3 that the two primary characteristics for a diffuse reflector are its reflectivity and its BRDF. Spectralon has a nearly constant BRDF, and thus exhibits excellent Lambertian behavior.[6] BRDF measurements for both Spectralon and Aerosil 90 were carried out at 404, 532 and 633 nm. The incident light was perpendicularly polarized, and directed at an angle of 30° from the surface normal. The detector was set to measure 8° degrees out of the plane of incidence. Figure 2.9 shows the results from these measurements for the three wavelengths. The data sets for the various wavelengths have been offset to allow for easy visualization on one plot. Figure 2.10 shows the results with the same setup, but with the incident light at parallel polarization. Similar results were seen when the angle of incidence was changed to 60° with both perpendicular and parallel polarization.[22] The results show that the fumed silica exhibits highly Lambertian behavior, and therefore is an

excellent Lambertian reflector.

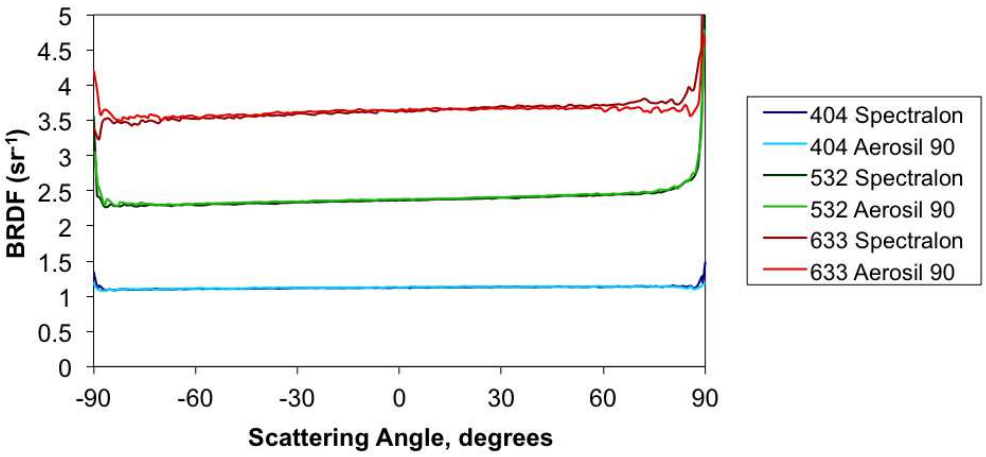

Figure 2.9: BRDF for incident light at 30° with perpendicular polarization.[22]

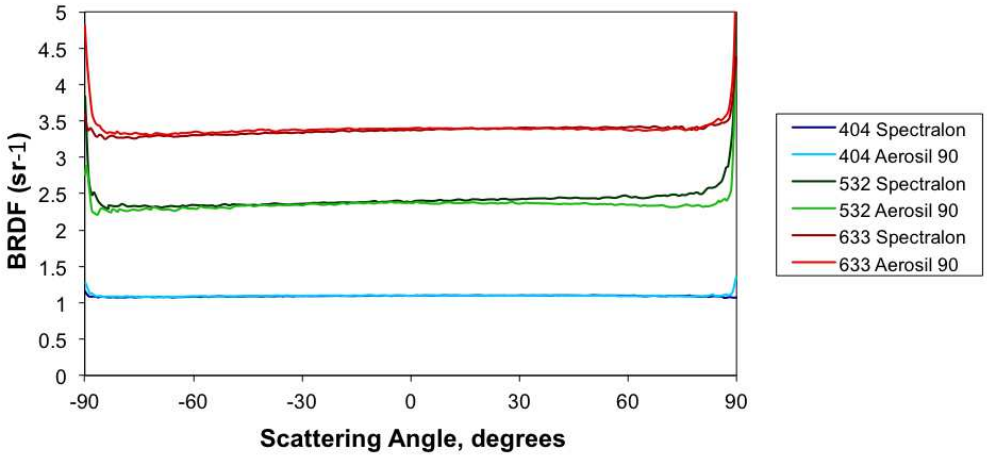

Figure 2.10: BRDF for incident light at 30° with parallel polarization.[22]

2.6 Preparation and Design of Fumed Silica Integrating Cavities

In the previous sections the measurements were carried out on small samples of packed fumed silica. Much of what follows involves the use of actual integrating cavities made of the fumed silica. Therefore, we will spend some time discussing how such cavities are designed and manufactured.

It was mentioned in Sec. 2.4 that, due to its hydrophilic nature, the powder must be baked to achieve the best results. This is typically done in a Fischer Scientific Isotemp Vacuum Oven that is coupled to a liquid nitrogen sorption pump. The system allows the powder to be baked at a temperature of ∼280° C at a pressure of ∼1 Torr. The oven also has a purge line that allows for backfilling with ultra-high purity argon as the material is cooling. This pre-baked powder is packed with a hydraulic press into a semi-solid material that can be used to make the cavity walls. Previous work comparing packing pressure to transmission of incident light for sample disks of the powder demonstrated that transmission was minimized for a

pressure range of 30-1000 psi.[22] In fact, for very high pressures, the pressed powder will start to become transparent as the individual fumed silica particles begin to make optical contact.

The cavities themselves are constructed in variety of different ways. One method involves using a mold that the powder can be packed into to form the desired cavity shape. These molded cavities are usually made in separate halves that are then stacked together to form the complete cavity. Figure 2.11 shows an example of a molded cavity, where the spherical inner cavity region was formed by packing the powder over a quartz glass hemisphere, which was later removed. High purity quartz glass is always used to form the inner cavity portion of the molded cavities in order to avoid contamination.

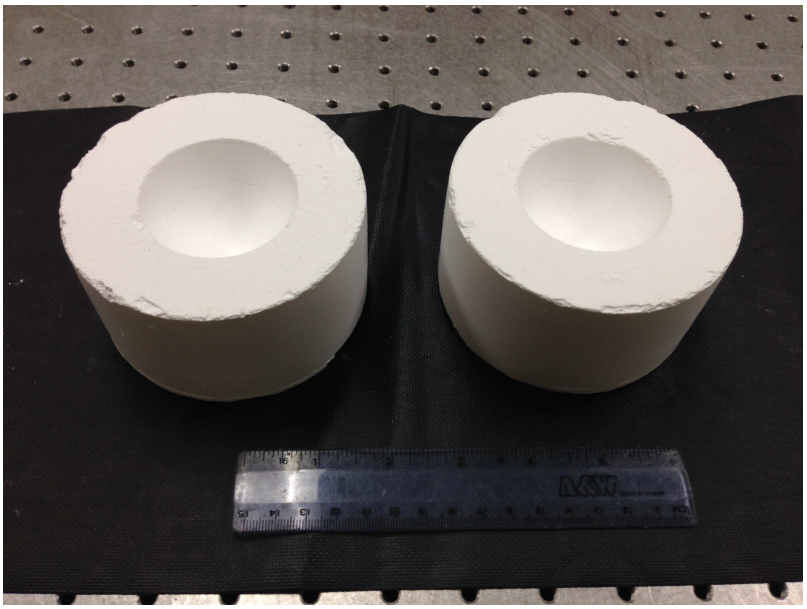

Figure 2.11: Picture of the two halves of a molded fumed silica spherical integrating cavity.

Another method for making cavities involves packing solid cylinders of the quartz powder, and then machining out the inner cavity region with a lathe or mill. This method also requires the cavity to be made in halves. Figure 2.12 shows an example of a cavity made using this machining method, and Fig. 2.13 shows the same cavity assembled.

Figure 2.12: Picture of the two halves of a machined fumed silica cylindrical integrating cavity.

Many of the applications that follow involve introducing a liquid or gaseous sample into an integrating cavity. In these cases, it is necessary to isolate the porous fumed silica that constitutes the cavity wall from the sample being tested. This is typically done by using a fused silica (quartz glass) sample cell to form the inner cavity wall. The quartz powder is then packed around this sample cell to form the

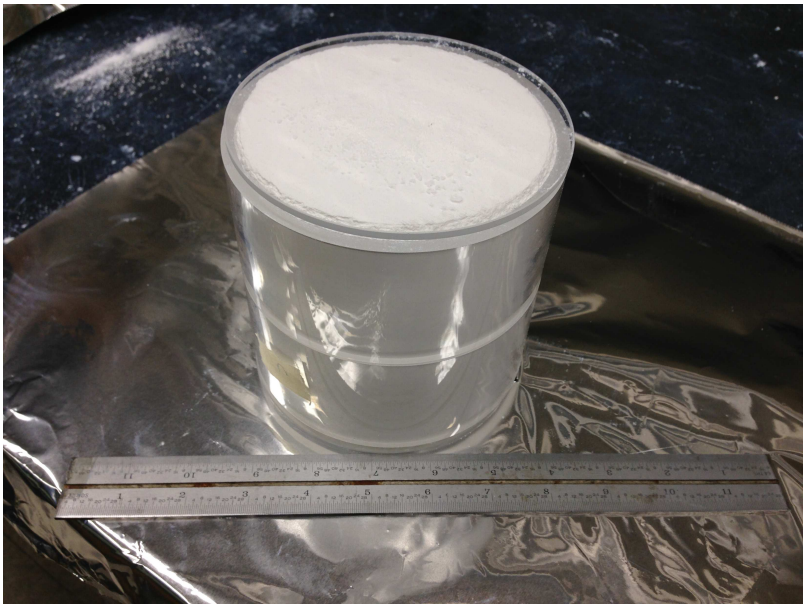

Figure 2.13: Picture of an assembled machined fumed silica integrating cavity.

diffuse reflecting wall. The Integrating Cavity Absorption Meter, discussed in the next chapter, is an example of this type of cavity.

Due to the intrinsic hardness of the material (quartz has a value of 7 on the Mohs scale), the powder will often "bite" into the surfaces of the mold pieces during packing. This can make it difficult to remove the finished pieces from the mold without significant damage. In addition, the powder can pick up a significant static charge during the packing process, which exacerbates this issue. Both of these issues can be alleviated by "pre-packing" the powder before making the final pieces. This involves packing the fumed silica to a given pressure (typically lower than the final packing pressure) in a quartz mold, and then breaking this packed material back into a powder form. During this entire process, only high-purity fused silica pieces are allowed to come into contact with the material to prevent any potential contamination. This pre-packed powder exhibits far less static and biting effects during the final packing

process, making it significantly easier to produce high quality pieces.

2.7 Absolute Measurements of Reflectivity

The relative reflectivity experiments described in Sec. 2.4 demonstrate that the Aerosil 90 and Aerosil EG50 fumed silica products exhibit a reflectivity higher than an equivalent Spectralon sample. However, these measurements do not allow one to get a meaningful absolute reflectivity value for the powders. In order to do this we have used a variation of a technique known as cavity ring-down spectroscopy (CRDS) developed by O'Keefe and Deacon.[23] In CRDS a temporally short pulse of light is coupled into a high-finesse cavity and is allowed to decay, or "ring-down." The exponential decay in the cavity can be monitored by placing a detector behind one of the mirrors to sample the intensity of the light leaving the cavity. The decay constant τ, for a pulse in such a cavity can be expressed as,

$$\tau = \frac{t_r}{2[-\ln\rho + al]}, \tag{2.10}$$

where t_r is the round-trip time for a pulse to traverse the cavity, ρ is the mirror reflectivity, a is the absorption coefficient of any absorbing medium placed within the cavity, and l is the length of the cavity.[24] The factor of 2 in Eq. 2.10 is included because the light must traverse the cavity twice for a round trip. For an empty cavity, $a = 0$, the cavity will ring-down with a decay constant τ_e. If that same cavity is filled with an absorber, the intensity will ring-down faster, giving a decay constant of τ_a. These two decay constants can then be used, with Eq. 2.10, to solve for the absorption coefficient. In addition, if the cavity dimensions (i.e. l) are known, one can also use the empty cavity decay time to determine the absolute reflectivity of the cavity mirrors.

In the case of an empty integrating cavity Eq. 2.10 reduces to,

$$\tau = -\frac{1}{ln\rho}\frac{\bar{d}}{c}, \tag{2.11}$$

where $^{t_r}/_2$ has been replaced with $^{\bar{d}}/_c$. This is identical to the result we derived in Sec. 1.5 for the decay of radiation inside an empty integrating cavity, where $\bar{d}$ is the average distance between reflections inside the cavity, and c is the speed of light. Recall from Sec. 1.6 that $\bar{d}$ for an arbitrary cavity is given by,

$$\bar{d} = 4\frac{V}{S}, \tag{2.12}$$

where V is the cavity volume, and S is the cavity surface area. Thus for an integrating cavity of known dimensions, measurement of the empty cavity decay constant τ_e, allows one to measure the absolute reflectivity for the cavity.

Ring-down measurements were made for fumed silica integrating cavities at 532 nm and 266 nm using the 2nd and 4th harmonic outputs from a Continuum Powerlite 9010 ND:YAG laser. The basic setup is shown in Fig. 2.14. The input pulse, typically 10-15 ns, was coupled into the cavity via a multimode fiber. Another multimode fiber samples the decay, or ring-down, of the irradiance on the cavity wall. This signal was detected via a Hamamatsu 1P21 photomultiplier tube. The input pulse was also measured with a Thorlabs DET210 photodiode by taking a reflection off of a glass filter.

The data was collected using a Hewlett Packard Infinium oscilloscope. The ring-down signal for single shots can be recorded, but typically the the data sets were averaged over 1024 shots. Figure 2.15 shows a typical oscilloscope signal after averaging. The green trace is the laser pulse measured by a photodiode inside the laser housing, and is used for triggering. The purple trace is the reflection of the input pulse indicated in Fig. 2.14, and the yellow trace is the ring-down signal from the

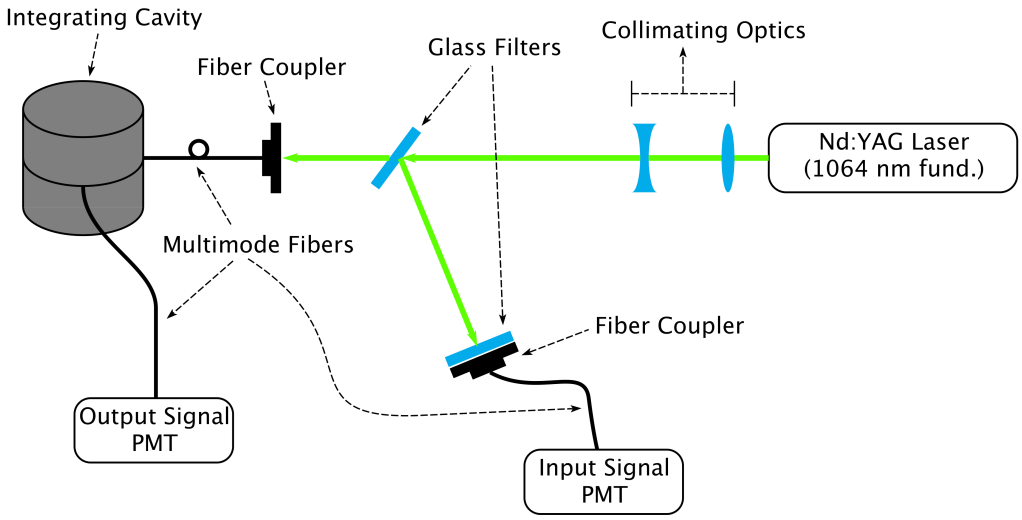

Figure 2.14: Typical experimental setup for measuring cavity reflectivity via the ring-down signal.

cavity.

In order to determine the decay constant for the cavity, the output pulse is fitted to an exponential function. This can be done in a variety of ways including: fitting only the tail of the output decay curve to an exponential of the form given in Eq. 2.11, convolving the actual input pulse with an exponential decay and fitting that to the output decay curve, and fitting the decay curve to the convolution of a Gaussian (representing the input pulse) and an exponential decay. All of these methods have been used, but the results shown here are fitted using the third method. The form of the convolution function is given by,

$$Fit(t) = A \exp\left(\frac{w^2}{2\tau^2} - \frac{(t-t_s)}{\tau}\right)\left(1 - \mathrm{erf}\left(\frac{w^2 - \tau(t-t_s}{\sqrt{2}w\tau}\right)\right), \tag{2.13}$$

where A is an amplitude coefficient, w is the width of the Gaussian function, t_s is a

Figure 2.15: Averaged oscilloscope output for a typical ring-down signal. The green trace is the signal from a photodiode inside the laser housing, the purple trace is a reflection of the input pulse, and the yellow is the ring-down signal from the cavity.

time shift from $t = 0$, and τ is the decay constant for the exponential function.

The absolute reflectivity tests were done on cavities made with the Aerosil EG50 powder. These cavities were manufactured in two halves using the machining method described in the previous section. The cavity used for the 532 nm test was a right-circular cylinder with a diameter of 3.81 cm and a height of 6.47 cm. Figure 2.16 shows the input laser pulse (in blue), the output ring-down decay curve (in red), and a fit to the decay curve (in green). Both the input and output curves have been normalized for this plot. The fit to the decay curve gives a decay constant of $\tau = 120.5$ ns. Combining this with Eqs. 2.11 and 2.12 gives a reflectivity of 0.9992

for the cavity.

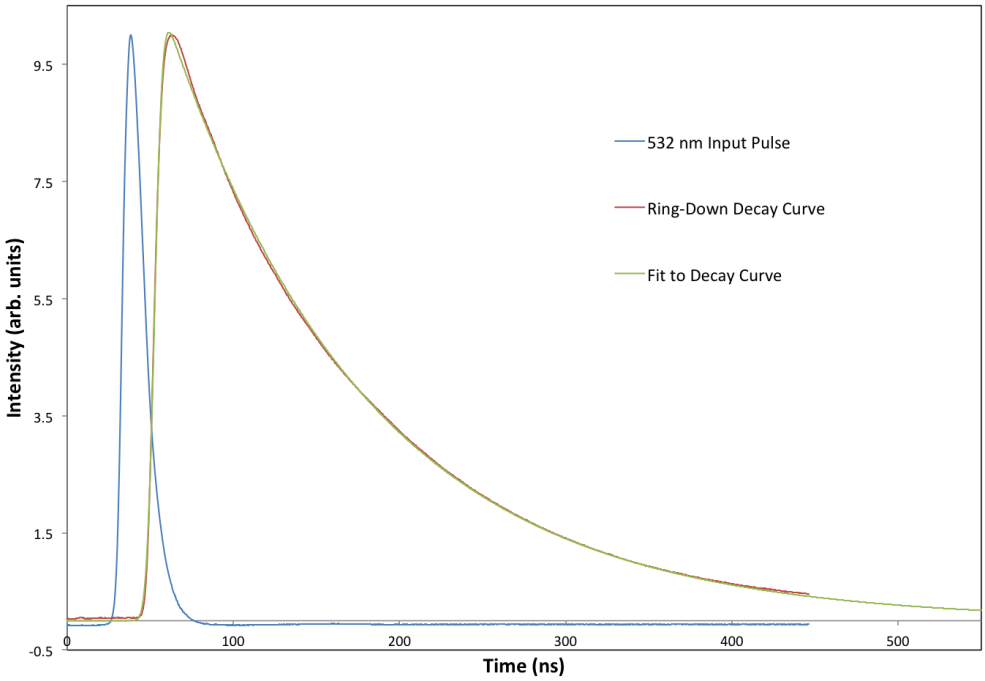

Figure 2.16: Plot showing the 532 nm input pulse (in blue), the ring-down decay curve for the fumed silica cavity (in red), and a fit to the decay curve (in green).

The 266 nm absolute reflectivity test was done with a cylindrical cavity with 5 cm height and diameter. Figure 2.17 shows the input laser pulse, the ring-down decay curve, and a fit to the decay curve for the 266 nm test. Again, both the input and output pulses were normalized for the plot. The fit to the decay curve gives a decay constant of $\tau = 35.3$ ns, which yields a cavity reflectivity of 0.9969.[22] This value, along with the value of 0.9992 at 532 nm, are, to the author's best knowledge, the highest diffuse reflectivity values ever measured.

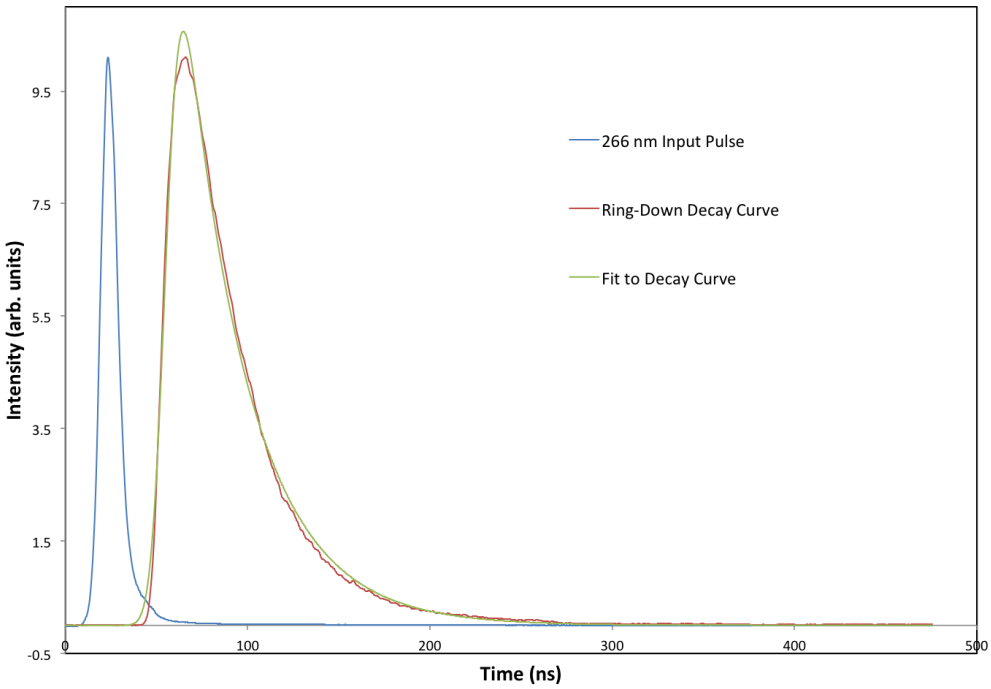

Figure 2.17: Plot showing the 266 nm input pulse (in blue), the ring-down decay curve for the fumed silica cavity (in red), and a fit to the decay curve (in green).

Recall from Sec. 2.1 that Spectralon, the current industry leader in diffuse reflectance, has reflectance values as high as 0.992 in the visible, but drops to 0.950 at 250 nm.[6] The values for our new fumed silica diffuse reflector are considerably higher in both regions. This difference is perhaps better appreciated if we consider the total effective path length L_{eff}, for a photon inside the cavity. In Sec. 1.5 we saw that the average number of reflections n, for a photon inside the cavity was given by,

$$n = -\frac{1}{\ln \rho}. \tag{2.14}$$

L_{eff} should simply be this n multiplied by the average distance between reflections in the cavity $\bar{d}$. Thus, we have

$$L_{eff} = -\frac{1}{\ln \rho}\bar{d} = \frac{1}{(1-\rho)}\bar{d} = \frac{4}{(1-\rho)}\frac{V}{S}, \tag{2.15}$$

where we have used Eq. 2.12, and exploited the fact that $^{-1}/_{\ln \rho} \approx {}^{1}/_{(1-\rho)}$ for $\rho \approx 1$. Using Eq. 2.15 for a spherical cavity with a diameter of 5 cm, we find total effective path lengths of $L_{eff} = 4.167$ m and $L_{eft} = 41.67$ m for cavity refelctivities of 0.991 and 0.9991, respectively. Figures 2.18 and 2.19 show plots of the effective path length vs. reflectivity for a 5 cm spherical cavity.

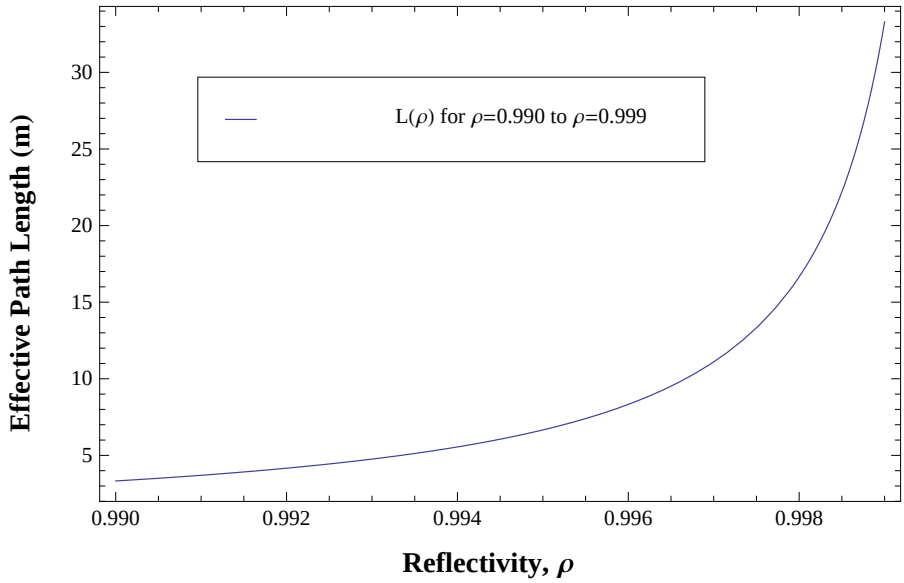

Figure 2.18: Plot of the effective path L_{eff} vs. the reflectivity ρ for a 5 cm spherical cavity over the range $\rho = 0.990$ to 0.999.

It should be noted that these absolute reflectivity values represent the average reflectivity of the cavity, and not the reflectivity for any particular portion of the cavity wall. In general this number should be less than or equal to the actual reflec-

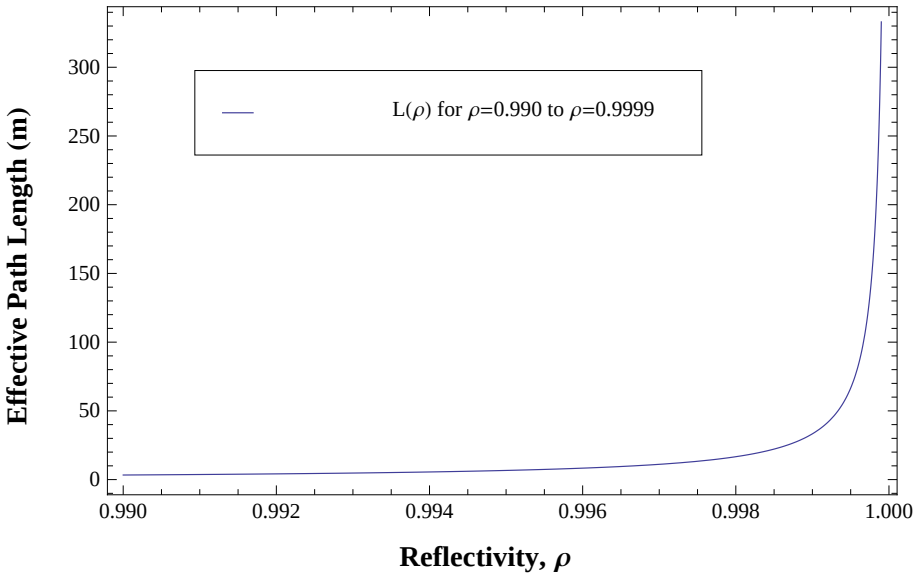

Figure 2.19: Plot of the effective path L_{eff} vs. the reflectivity ρ for a 5 cm spherical cavity over the range $\rho = 0.990$ to 0.9999.

tivity (or reflectance) for the fumed silica wall. The reason for this is that the cavity reflectivity intrinsically includes any loss effects due to ports, or imperfections in the cavity wall. For instance, the two cavities used in these measurements each had two fibers coupled in to deliver the input pulse and measure the output pulse. These are essentially ports in the cavity, and thus lower the overall cavity reflectivity from that of an ideal cavity made from the same material.

2.8 SEM Measurements

The cavity used for the 532 nm reflectivity measurements was made of the same material, and was of similar size as that used for the 266 nm test. However, it was subjected to an additional high-temperature bakeout prior to the ring-down measurement. This bakeout was done in a lab furnace at a temperature of 1000° C, and was in addition to the pre-bake process described Sec. 2.6. This baking process

resulted in a higher cavity reflectivity than the previous best for the fumed silica at 532 nm; a value of 0.998.[22]

In order to verify the benefit of this additional step, a single cavity was prepared and tested both before, and after the bakeout. The two cavity halves were made using the quartz glass mold process described in Sec. 2.6. This resulted in a spherical cavity with a diameter of 52 mm. A ring-down test at 532 nm was performed immediately after the cavity was completed. The piece was then baked at $\sim$1000° C for several hours, and tested again. Figure 2.20 shows the output ring-down signal for this cavity before, and after the high-temperature bakeout. The fits to these two ring-down curves yield decay constants of 13.89 ns and 83.76 ns, which correspond to cavity reflectivities of 0.9934 and 0.9985, respectively.[‡]

It is evident from Figure 2.20, and the corresponding reflectivity numbers, that the bakeout has a significant effect on the cavity. On a more tangible level, the packed fumed silica material has a different feel to it after this process. It is noticeably drier to the touch, and also seems slightly more durable and machinable. Of course, one would like to know what, if any, effect this bakeout is actually having on the material at the microscopic level. The basics of the method used to make the these cavities is essentially identical to the process for sintering powders. Sintering typically involves a high-purity metal or ceramic powder that is pressed into a mold and then baked at a high-temperature under the material's melting point. The result is to turn the powdered material into a solid via atomic diffusion. However, existing work with quartz ceramic powders suggests that no real sintering effects occur for temperatures of less than 1100° C.[25]

[‡]This reflectivity is lower than the reflectivity for the measurements presented in the previous section (i.e. 0.9985 vs. 0.9992). This is because this was a molded piece, as opposed to a pressed and machined piece. The molded cavities tend to have a lower reflectivity than the machined cavities due to the lower packing pressures that are used to protect the quartz glass mold.

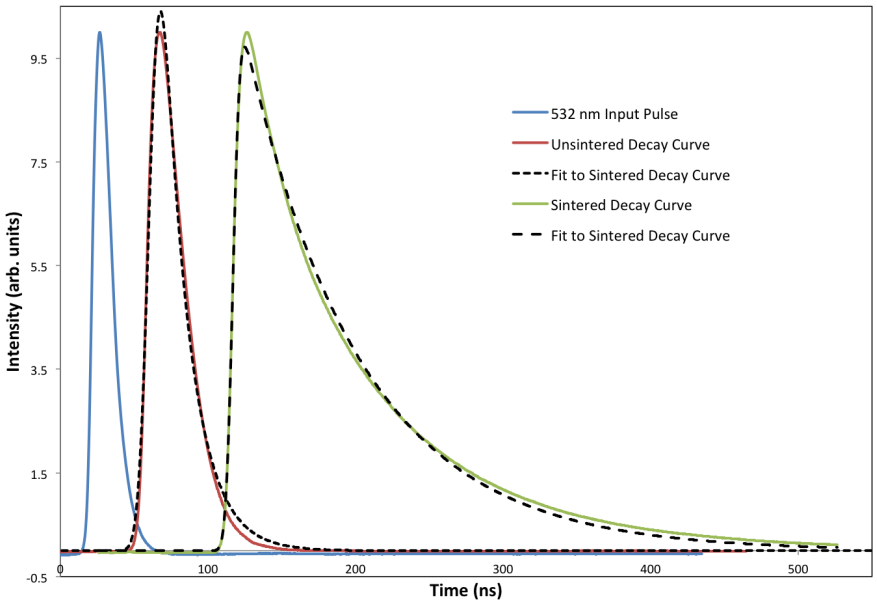

Figure 2.20: Ring-down (RD) decay curves before, and after a high-temperature bakeout. The blue trace is the 532 nm input pulse, while the red and blue traces represent the RD curve before and after the high temperature bakeout, respectively. Fits for both of the RD curves are also shown. All three curves on this plot have been shifted in time for presentation.

Another possibility is that this bakeout is simply removing volatile contaminants trapped in the powder. As mentioned before, these fumed silica powders are hydrophilic, so water is a likely contaminant. The pre-bake procedure described in Sec. 2.6 is done to remove any trapped water. Nevertheless this second bake could be removing residual water, as well as any water vapor that was absorbed during the manufacturing process.

In an effort to determine whether the benefits of the bakeout are due to an actual change in the microscopic characteristics of the material, several samples were imaged with a scanning electron microscope (SEM). The samples were all 2.5 mm thick 12 mm diameter disks of pre-baked packed Aerosil EG50. The disks were held in quartz

glass rings with a outer diameter of 16 mm, and a thickness of 2.5 mm. All of the samples were initially prepared the same way, but two of the three samples were given an additional high-temperature bakeout at temperatures of 930° C and 1085° C. These two temperatures were chosen based on previous experience. Pieces baked at ∼1085° C have a tendency to shrink, while pieces baked at ≤1000° C seem to maintain their original volume. These three samples were imaged using a JEOL JSM-7500 field emission SEM. SEM imaging for insulating materials like quartz is complicated by the fact that the quartz sample tends to pick up charge from the electron beam, which then produces a repulsive effect on the beam. This results in a jittering of the beam that limits the SEM's ability to focus. To alleviate this issue, the quartz samples were placed in a set of brass sample holders. These holders were machined with recesses to accommodate the height and diameter of the quartz glass rings that encompassed the quartz powder sample disks. In addition to this, the top surface of each sample was sputtered with a 5 nm Platinum-Palladium coating. These two steps were effective in reducing the surface charging effects, and allowing for higher magnification imaging. A fourth sample of loose powder was also prepared. This involved taking a very small portion of the powder (about the size of a pinhead) and dissolving it in several milliliters of isopropyl alcohol. This solution was then sonicated and applied to the surface of a TEM grid, which was then allowed to dry.

Figure 2.21 shows the SEM images for the loose powder sample. In Fig. 2.21(a) we see a close-up of an agglomerate particle several microns in length, where the individual spherical base particles are clearly visible. At a slightly higher magnification, see Fig. 2.21(b), we see base particles in small aggregates, as well as on their own. At this scale it is easy to tell that the base particles have a considerable size variance, but all fall in the range of several ∼10-100 nm. The dark webbing structure that is visible in both images is conductive tape that was used to hold the TEM grid

in place during the imaging process.

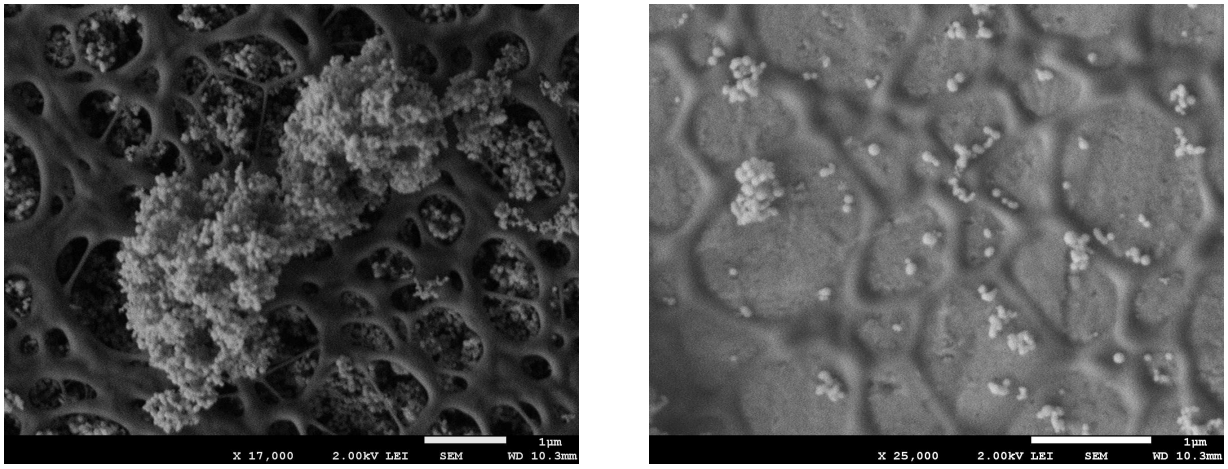

(a) (b)

Figure 2.21: SEM images of a loose powder sample showing (a) an agglomerate particle, and (b) individual base particles. The webbed structure underneath the particles is conductive tape used to hold the TEM grid in place.

Figures 2.22-2.24 show two SEM images each, at magnifications of 20,000x and 50,000x for the unbaked sample, and the samples baked at 930° C and 1085° C, respectively. The slight blur on the three higher magnification images is due to the surface charging effects mentioned above. The three sets of images look strikingly similar, and do not show any obvious change in the microscopic structure due to the high-temperature bake. This suggests that if any true sintering effects are taking place, they are minimal.

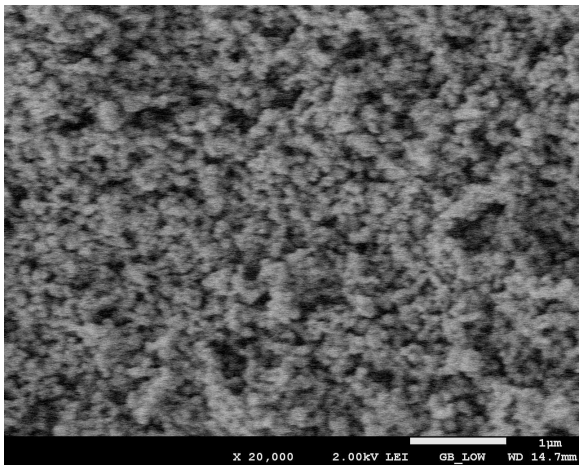

(a)

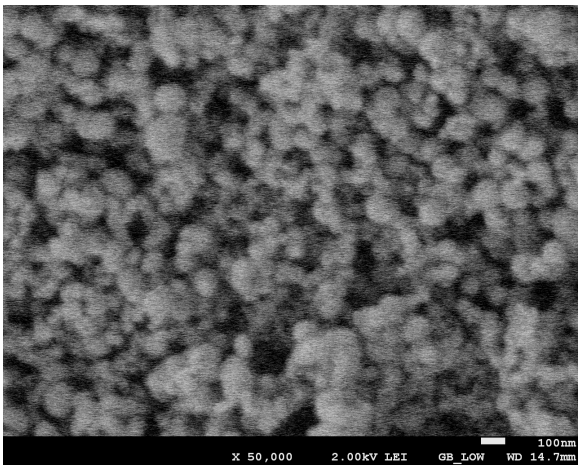

(b)

Figure 2.22: SEM image of a packed fumed silica sample without the additional high-temperature bakeout at (a) low (20,000x) and (b) high (50,000x) magnification.

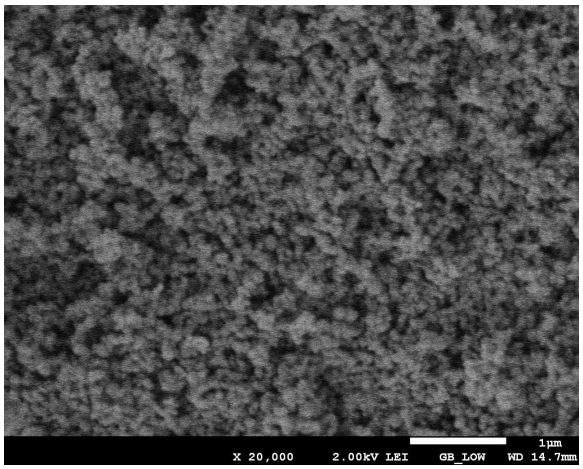

(a)

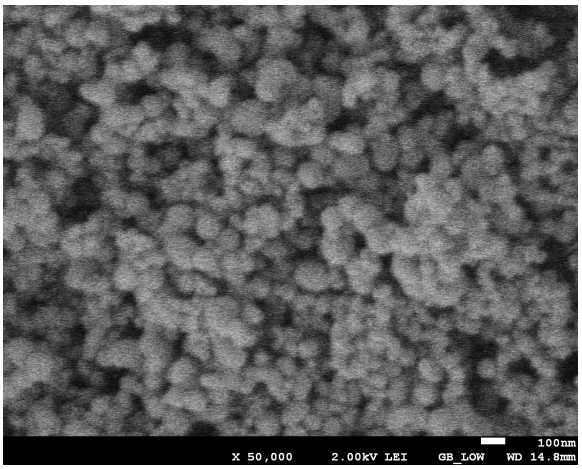

(b)

Figure 2.23: SEM image of a packed fumed silica sample baked at 930° C for (a) low (20,000x) and (b) high (50,000x) magnification.

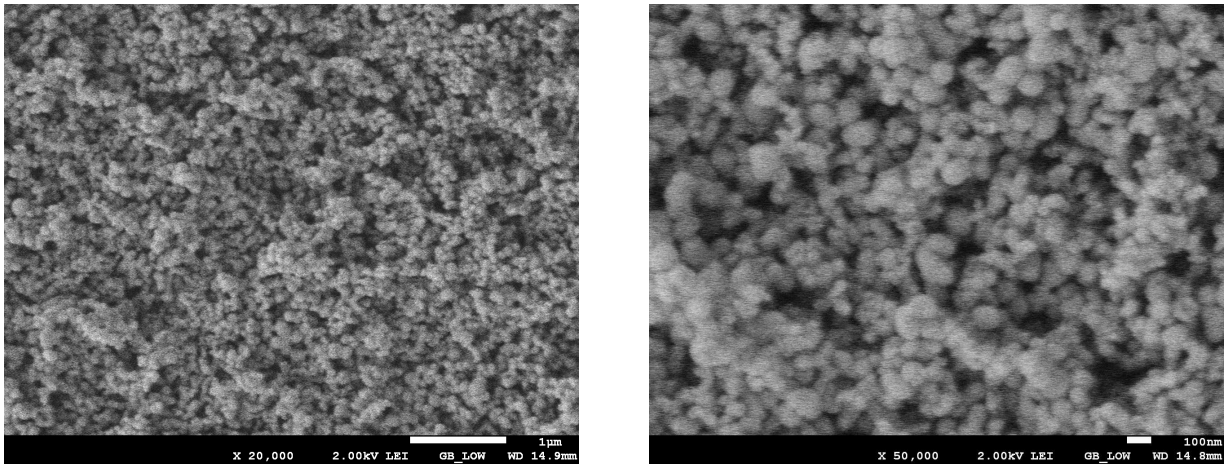

(a) (b)

Figure 2.24: SEM image of a packed fumed silica sample baked at 1085° C for (a) low (20,000x) and (b) high (50,000x) magnification.

3. THE INTEGRATING CAVITY ABSORPTION METER

The initial interest in developing the fumed silica diffuse reflector stemmed from a desire to measure the absorption coefficient of pure water a_{pw}, in the ultraviolet. Pope *et al.* used a device called an Integrating Cavity Absorption Meter (ICAM) to measure a_{pw} from 380-700 nm.[26] However, early attempts to extend this data set down to 300 nm met with considerable difficulties. This was primarily due to the limitations of the Spectralon used to make the ICAM's walls.[27] As we saw in Ch. 2, Spectralon has a reflectance of 99.0-99.2% across the visible spectrum, but it drops considerably as one moves into the UV, being only 95.0% at 250 nm. On the other hand, cavities made from the fumed silica diffuse reflector can have reflectivities as high as 99.6% at 266 nm. The sensitivity of the ICAM is dependent on the reflectivity of its walls. Thus, replacing the Spectralon in the ICAM with packed fumed silica should allow for superior measurements in the ultraviolet. In this chapter we will detail the implementation of a modified ICAM (or, UV-ICAM) for measuring a_{pw} down to 250 nm.

3.1 The Optical Properties of Pure Water

The optical properties of water are typically divided into two categories: inherent optical properties (IOP's), and apparent optical properties (AOP's). The IOP's are those that depend only on the water itself, and not on the nature of the light field. On the other hand, the AOP's depend on the nature of the light field, as well as the water the light is traveling in. Thus the AOP's actually depend on the IOP's.[3]

The absorption coefficient and the volume scattering function are the two fundamental IOP's for water. Therefore, accurate measurements of these properties for pure water is of tremendous value. As an example, consider that a natural body of

water will, in general, have dissolved organic and inorganic compounds, as well as suspended particles and biological material. Knowledge of the pure water IOP's can be used as a baseline, allowing for measurement of the optical properties of these other constituents.

3.2 Typical Methods of Absorption Spectroscopy

Anyone who has ever visited a particularly clear lake or ocean can attest to the fact that water is very transparent to visible light. In fact, it is precisely this transparency that makes measuring the absorption coefficient of pure water very challenging. For instance, $a_{pw} \leq 0.7\,\mathrm{m}^{-1}$ over the entire region from 250-700 nm, and $a_{pw} \leq 0.01\,\mathrm{m}^{-1}$ over the region from 385-460 nm. In addition, if we consider the scattering coefficient of water over the same spectral region, we find that it can be quite significant. Values for the scattering coefficient are $b_{pw} \approx 0.06\,\mathrm{m}^{-1}$ for 250 nm, $b_{pw} \approx 0.006\,\mathrm{m}^{-1}$ for 420 nm, and $b_{pw} \approx 0.003\,\mathrm{m}^{-1}$ for 500 nm. Clearly, if we are interested in making accurate measurements of a_{pw}, the effects of scattering cannot be ignored.[26,28]

A variety of methods have been used to measure a_{pw} in the visible and near-UV. The easiest experiment to envision involves measuring the attenuation of a light source that has been transmitted through a long column of water. An obvious drawback to this method is that the quantity being measured is the attenuation coefficient, $c = a + b$, and not the absorption coefficient. Thus, the scattering coefficient must either be measured, or calculated and subtracted out. This necessarily leads to an increase in the error for the measurement. In addition to this problem, the large path lengths needed for this style of experiment require the preparation and maintenance of large volumes of pure water. Numerous groups have used transmission style experiments to measure a in the visible and near-UV for both pure water and

heavy water, including; Quikenden *et al.*, Boivin *et al.*, and Litjens *et al.*.[29–31] Other methods of measuring a_{pw} include: measuring the photoacoustic effects that result from the heating of the water due to laser light, used by Tam *et al.*, the photothermal deflection of a probe laser resulting from the index of refraction gradient produced by the heating of the medium due to absorption of laser light, used by Sogandares *et al.*, and thermal lens spectroscopy, used by Cruz *et al.*[32–34]

3.3 The ICAM

In Sec. 1.4 it was mentioned that Elterman showed an integrating cavity could be used for absorption spectroscopy.[9] Based on this idea, Fry *et al.* developed the original ICAM as a novel approach for measuring the absorption coefficient of pure water.[35] The ICAM consists of two concentric integrating cavities. The outer cavity is an air gap, while the inner cavity is the sample region. Figure 3.1 shows a cross section of a generic ICAM. The air gap, and sample regions are labeled as regions I and II, respectively, and the concentric diffuse reflecting walls are depicted in dark blue. Two fibers sample the irradiance on the cavity wall in regions I and II of the ICAM. This light is sent to detectors that produce signals S_0 and S_1 that are proportional to the irradiances F_0 and F_1. The ratio, S_1/S_0, of these two detector signals is what is actually measured in this experiment. In the following section, we will show that this ratio is directly proportional to the absorption coefficient of whatever fills the sample region.

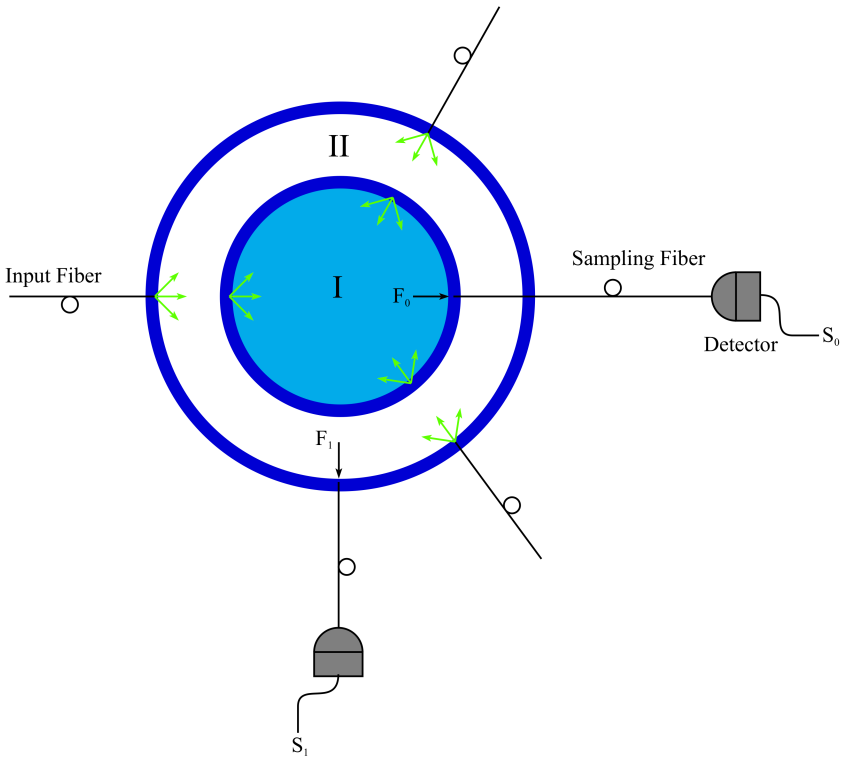

Figure 3.1: Cross section of a generic ICAM.

3.4 ICAM Theory

The theoretical derivation of the working equation for the ICAM was originally developed by Fry *et al.*, and is reviewed here.[26,35] We begin by defining a vector irradiance $\boldsymbol{F}$, such that

$$\boldsymbol{F} = \int_{\Omega} L(\boldsymbol{r}, \hat{\Omega}) \hat{\Omega} \mathrm{d}\Omega, \tag{3.1}$$

where $L(\boldsymbol{r}, \hat{\Omega})$ is the radiance in the direction of the unit vector $\hat{\Omega}$ at a point $\boldsymbol{r}$, and the integral is over the solid angle Ω. In addition, we define a radiant energy, U, given by,

$$U = \frac{m}{c} \int_{\Omega} L \mathrm{d}\Omega, \tag{3.2}$$

where c is the speed of light, and a homogenous medium of refractive index m is assumed. Recall from Sec. 1.2 that the radiative transfer equation describes how the radiance is propagated through a medium. For this case we can express the RTE as,

$$\hat{\Omega} \cdot \nabla L(\boldsymbol{r}, \hat{\Omega}) = -\beta_e L(\boldsymbol{r}, \hat{\Omega}) + \frac{\beta_s}{4\pi} \int_{\Omega'} p(\Omega, \Omega') L(\boldsymbol{r}, \hat{\Omega}') \mathrm{d}\Omega', \tag{3.3}$$

where β_e is the attenuation coefficient, β_s is the scattering coefficient, and p is the scattering phase function.[4] The scattering phase function satisfies the normalization condition,

$$\frac{1}{4\pi} \int_{\Omega} p(\Omega, \Omega') \mathrm{d}\Omega = 1. \tag{3.4}$$

From here it is straightforward to show that integrating Eq. 3.3 over the solid angle Ω gives,

$$-\nabla \cdot \boldsymbol{F} = \frac{(\beta_e - \beta_s)c}{m} U = \frac{ac}{m} U, \tag{3.5}$$

where we have used the fact that $(\beta_e - \beta_s)$ is simply the absorption coefficient, a. Equation 3.5 is a fundamental relation, and is valid at every point in the medium, irrespective of the magnitude of any scattering effects.

Integrating Eq. 3.5 over the volume V of the sample and using the divergence theorem we get

$$-\int_S \boldsymbol{F} \cdot \mathrm{d}\boldsymbol{S} = \frac{ac}{m} \int_V U \mathrm{d}V. \tag{3.6}$$

Examining Eq. 3.6, it is obvious that the left-hand side is the net radiant power entering the sample volume. In other words, it is the power P that is absorbed by the sample. Thus, we have

$$P = \frac{ac}{m} \int_V U \mathrm{d}V. \tag{3.7}$$

So long as the initial assumption of a homogenous medium is valid, Eq. 3.7 is exact and completely independent of any scattering effects. If we also assume that the energy density is homogeneous, then Eq. 3.7 becomes

$$P = \frac{ac}{m} UV. \tag{3.8}$$

This is the same result that Elterman derived for a one-dimensional system.[9]

Equation 3.8 is a very important result, but we can put it in a more useful form by relating the energy density inside the sample to the normal component of $\boldsymbol{F}$ at the inside surface of the sample. This component of $\boldsymbol{F}$ is called the scalar irradiance, F_{out}, and is simply the outwardly directed irradiance at the surface of the sample. For the case of a radiance distribution that is both homogeneous and isotropic within the sample, L is simply a constant. This means Eqs. 3.1 and 3.2 can be expressed as

$$F_{out} = \hat{\boldsymbol{n}} \cdot \int_\Omega L(\boldsymbol{r}, \hat{\Omega}) \hat{\Omega} \mathrm{d}\Omega = \pi L, \tag{3.9}$$

$$U = \frac{4\pi m L}{c}, \tag{3.10}$$

respectively, where $\hat{\boldsymbol{n}}$ is an outward unit vector normal to the surface. Combining these two equations gives

$$U = \frac{4m}{c} F_{out}. \tag{3.11}$$

This, along with Eq. 3.8 gives us our final result for the power absorbed by the sample,

$$P_{abs} = 4aVF_{out}. \tag{3.12}$$

Thus we see that if one is able to measure F_{out}, V, and P, then it is possible to determine to the absorption coefficient a.

In order to make Eq. 3.12 practical we need to apply it to a realistic instrument. Consider the the generic ICAM depicted in Fig. 3.1. Light is injected into region II (an air gap) though several fibers, and is immediately diffused throughout the region due to scattering off of the two diffuse reflecting walls. This light can leave region II by penetrating the outer wall, and thus leaving the cavity, but it can also diffuse through the inner cavity wall into region I (the sample region). Energy conservation requires that the total power entering region I must be equal to the total power leaving the region, plus the total power absorbed inside the region. That is,

$$P_{in} = P_{out} + P_{abs}. \tag{3.13}$$

Combining this with Eq. 3.12 gives

$$P_{in} = P_{out} + 4aVF_0, \tag{3.14}$$

where we have replaced F_{out} from Eq. 3.12 with the outward irradiance in region I, F_0, shown in Fig. 3.1.

In what follows we will assume that the radiance at any point in region I of

Fig. 3.1 is isotropic and homogeneous, and that the radiance at any point in region II is proportional to the radiance at other points in region II. Based on this, we are able to write the power into and out of region I in terms of F_1 and F_0. The power entering region I will be proportional to F_1, and the power leaving the same region will be proportional to F_0. Thus we can write Eq. 3.14 as

$$K_1 F_1 = K_0 F_0 + 4aVF_0, \tag{3.15}$$

where K_0 and K_1 are proportionality constants. As shown in Fig. 3.1, the irradiances F_0 and F_1 are sampled with fibers that send the optical signals to detectors that, in turn, produce electrical signals with magnitudes determined by the spectral response of the detector. If the detectors produce signals S_0 and S_1, then Eq. 3.15 can be rewritten as

$$C_1 S_1 = C_0 S_0 + 4aVS_0, \tag{3.16}$$

where C_0 and C_1 are another set of proportionality constants. Dividing Eq. 3.16 by $C_1 S_0$, and relabeling ${}^{S_1}/_{S_0}$ by S we find,

$$S = \frac{4}{C_1} aV + C_0', \tag{3.17}$$

where ${}^{C_0}/_{C_1}$ has been replaced with C_0'. This is the ICAM working equation which can be solved for the absorption coefficient in terms of the ICAM signal S. A measurement of a for a given sample is made by taking the ICAM signal, S_{full}, for a cavity filled with the sample, and subtracting the signal for the empty cavity S_{empty}. The two proportionality constants correspond to normalization and offset calibrations for the instrument. The offset calibration involves measuring S for increasing volumes

of pure water in the sample region, while normalization is achieved by measuring S for a dye solution with known absorption.[26,35]

Equation 3.17 shows that the ICAM provides a direct measurement of the absorption coefficient, unlike the transmission experiments described in Sec. 3.2. This measurement is completely independent of any scattering effects. Thus, the ICAM can be used to measure a even when the sample exhibits strong scattering.

3.5 Experimental Setup

In the original ICAM measurements by Pope *et al.*, both of the concentric integrating cavities were constructed out of Spectralon, which significantly limited its sensitivity in the ultraviolet.[26] In order to extend these measurements into the UV, two new incarnations of ICAM have been constructed.[27,36] These are designated UVICAM-I and UVICAM-II throughout this discussion. UVICAM-I, shown in Figure 3.2, is simply a rebuild of Pope's ICAM, where the original Spectralon inner cavity wall has been replaced with packed fumed silica. The sample region is a Suprasil fused silica cell from Heraeus Quartz with an 88 mm OD and an inner volume of 566 ml. The ends of the sample cell have a slight taper that leads to two 7 mm OD fused silica delivery tubes. This cell forms the inner boundary for the packed quartz powder. The outer boundary is a TOSOH ED-H synthesized fused silica tube with 96.5 mm ID and 105 mm OD. The end caps of this piece are made of TOSOH ES fused silica and each have a diameter of 105 mm with a 20 mm center hole. A Suprasil tube with a 20 mm OD was welded to each end cap. The quartz power is packed between these two fused silica pieces to form the diffuse reflecting wall. The packing process involves adding small amounts of the quartz powder at a time and pressing it with a quartz rod, or a curved quartz plate. This process is very tedious, and great care must be taken to avoid any inconsistencies in the wall do to

poor packing. One can check the quality of the wall during the packing process by illuminating the sample cell with a bright flashlight or laser pointer. Areas of loose packing will show as bright spots. These areas can be fixed provided that they are not too far down in the packed wall.

The outer wall of the UVICAM-I is made of six interlocking Spectralon plates that form a hexagonal cross section. Each plate is 12.7 mm thick and 254 mm high. The ends of the outer wall are closed with two 12.7 mm thick hexagonal Spectralon end caps. Each end cap has 20 mm through hole to accommodate the fused silica end caps from the inner cavity. Two Spectralon plugs with 7 mm through holes seal up the remaining openings on the top and bottom, while allowing the two fused silica tubes on each end of the sample cell through for water delivery.

Light is sampled from the outer cavity via a Thorlabs FT-800-UMT fiber, with a 800 μm core, and a numerical aperture of 0.37. The fiber is coupled to the outer cavity through a Spectralon plug that mates with one of the six Spectralon plates that form the outer wall. Light in the inner cavity is sampled with a second fiber of the same type. This fiber is coupled to the outside of the fused silica sample cell via another Spectralon plug that penetrates both the inner and outer walls as shown in Fig. 3.2.

UVICAM-II, shown in Fig. 3.3, differs from UVICAM-I in two significant ways: first, both the inner and outer diffuse reflecting walls are made of fumed silica (i.e. no Spectralon), and second, the volume of the sample cell has been significantly increased. The sample cell is again made from Suprasil and has a 136 mm OD, with a volume of 1530 ml. The outer cavity (air gap) is formed by a set of Suprasil quartz tubes (represented by the blue lines in Fig. 3.3), and four quartz plates (represented by the green lines). The outermost wall (shown in black) is made of schedule 40 PVC pipe, and simply serves as a container. Packed fumed silica (shown in grey) fills the

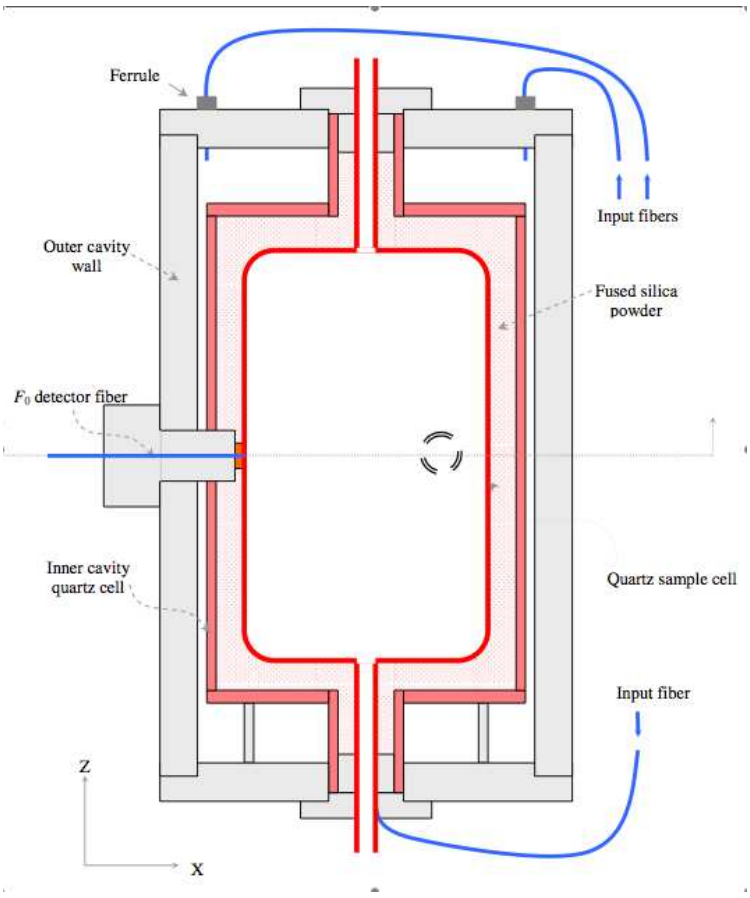

Figure 3.2: Cross section of UVICAM-I.

space between the sample region and the air gap, as well as the region between the air gap, and the outer PVC container. This powder was packed using a custom set of quartz packing plates to eliminate any chance of contamination. In addition, the entire packing procedure was carried out inside a glove hood that was purged with high-purity argon. This step was meant to limit the amount of water vapor that could be absorbed by the powder while packing was carried out. Two polished Suprasil quartz rods (shown in pink in Fig. 3.3) are coupled to the inner and outer cavity of the UV-ICAM II to sample the cavity irradiances.

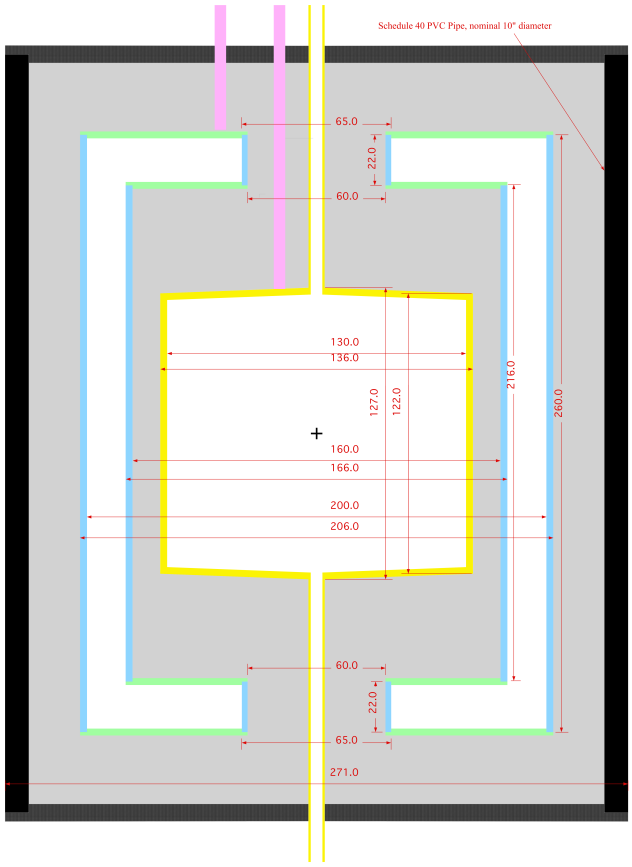

Figure 3.3: Cross section of UVICAM-II.

Figure 3.4 shows the basic experimental setup for both UVICAM's. The light source is an Oriel 6255 150 Watt Xe arc lamp. This is run through a Digikrom 240 monochromator, and then sent through quartz fibers into the UVICAM. The irradiances in the inner and outer cavities are monitored via two quartz optical fibers (two quartz rods for UVICAM-II) and the light signals are sent through light choppers before being sent to a single shielded PMT detector (a Burle 4840 for UVICAM-I, and an ET Enterprises 9558QB for UVICAM-II). Two lock-in amplifiers (an SRS 830, and an EG&G 5210) are used to pick out the individual signals, S_0 and S_1. These signals are then sent to a computer through a GPIB connection. A

Labview virtual instrument (VI) program is used to collect this data from the lock-in amplifiers, as well as to adjust the monochromator during the data runs.

The pure water is provided by a Millipore Gradient water purification system which can deliver Type I ultrapure water with a resistivity of 18.5 $M\Omega\,\mathrm{cm}$ at $\sim 25°$ C, and a total organic content (TOC) of ≤ 5 ppb. Quartz glass tubing delivers the water into the ICAM in order to minimize any potential contamination. The volume of water in the cavity is controlled by using pressurized high-puity nitrogen to push the water into the ICAM's sample region.

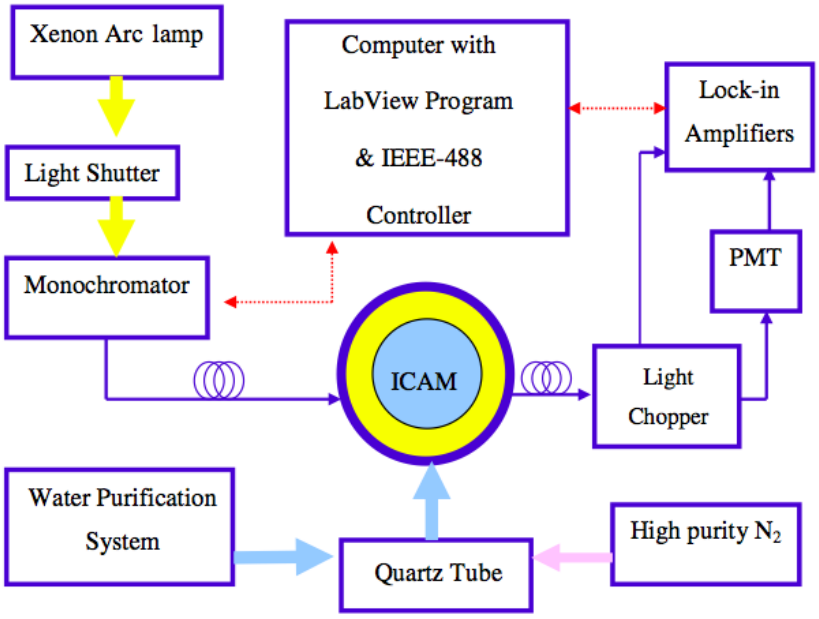

Figure 3.4: Flowchart for a typical UV-ICAM experiment.[27]

3.6 Calibration

In Sec. 3.4 we saw that the ICAM requires calibration in order to determine the coefficients C_1 and C_0 in Eq. 3.17. The theory for this calibration has been presented in great detail in previous work dealing with the ICAM.[26,27,35,36] A summary of this theory, along with a detailed explanation of the calibration process is given in App. A. Here we simply give a brief description of the techniques used.

The dye used for the normalization calibration to determine C_1 was made by taking a small amount of Irgalan Black powder and diluting it in Type I ultra pure water. A sonication bath was used to thoroughly mix the solution, which was then filtered several times to remove any undissolved particles. The absorption coefficient for this "Master Dye" was measured using an Agilent 8453 UV-VIS spectrophotometer. Calibration involves filling the ICAM sample region with dilutions of this Master Dye solution and measuring the ICAM signal, S, for each dilution at a particular wavelength. This signal is plotted against the absorption coefficient for each dye dilution. The slope from a linear fit to this data give C_1.

The offset calibration C_0 was determined by measuring the ICAM signal for increasing volumes of pure water. This is necessary because there are discontinuities in the data that correspond to index matching differences between an empty and full cavity.

3.7 UV-ICAM Results

Figure 3.5 shows the results for measurements of the absorption coefficient of pure water by UVICAM-I and II. It is immediately evident that the two methods give different results for various portions of the spectrum. In the visible they produce results with nearly identical shape and structure, but the UV-ICAM II data has a vertical shift relative to UV-ICAM I. The shape and structure seen in the visible

for both sets of data are in good agreement with the harmonic structure described by Pope and Fry.[26] The vertical shift for UVICAM-II may be due to issues in the volumetric water calibration used for the measurement of C_0. This calibration is performed for the entire region of measurement, and thus it may not correctly reflect any difference in C_0 for the UV versus the visible. This could potentially be improved by running the visible portion of the spectrum as a separate experiment, with its own calibration. The visible data for UVICAM-I is in very good agreement with the existing data.

In the UV region from about 300-350 nm UVICAM-I shows a distinct "hump" structure that does not appear in the UVICAM-II data. UVICAM-I also gives a considerably lower minimum ($\sim$0.003 m^{-1} for 386-394 nm), then has previously been seen in ICAM results.[26,27,36] However, both data sets agree fairly well for the region below 300 nm. This is likely due to the fact that the larger absorption coefficient in this region is inherently easier to measure.

Figure 3.6 shows the same UVICAM results plotted along with previous ICAM results, and the transmission-style UV measurements of Quikenden *et al.*[26,27,29,36] It is clear that the various measurements show substantial disagreement for a_{water} in the UV. The ICAM data taken by Lu and Fry, shows structure that is in-line with the expected vibrational and rotational harmonic structure.[27] However, this data has thus far not been replicated by later ICAM experiments, including the two UVICAM experiments.[36] It should be noted that the Wang and Fry data was acquired using a different approach to the calibration than all of the other ICAM experiments shown here.[36]

The high degree of variability in the data for a_{water} in the UV suggests the need for future work. There is definitely potential room for improvement in the ICAM experiments. For instance, the UVICAM-II currently has a very thick ($\sim$10 mm)

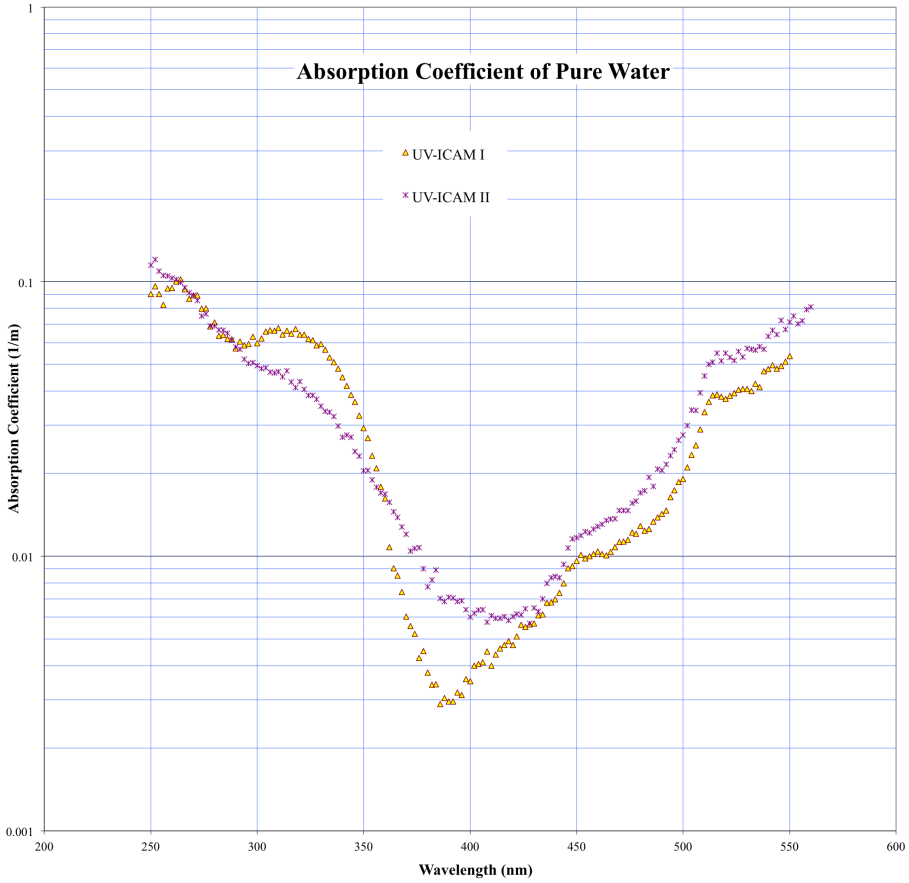

Figure 3.5: Results for the measurement of the absorption coefficient of pure water for UV-ICAM I and II.

inner cavity fumed silica wall. This has led to some difficulty in getting sufficient input light into the sample region, which in turn leads to a very small inner cavity signal. Redesigning the UVICAM-II inner cavity wall to be thinner, perhaps 5-8 mm, could increase the amount of light that diffuses into the inner cavity. This would likely result in an improved inner cavity signal. Another option is to attempt a different experimental method. One potential path is to use the integrating cavity ring-down spectroscopy technique that is introduced in the next chapter.

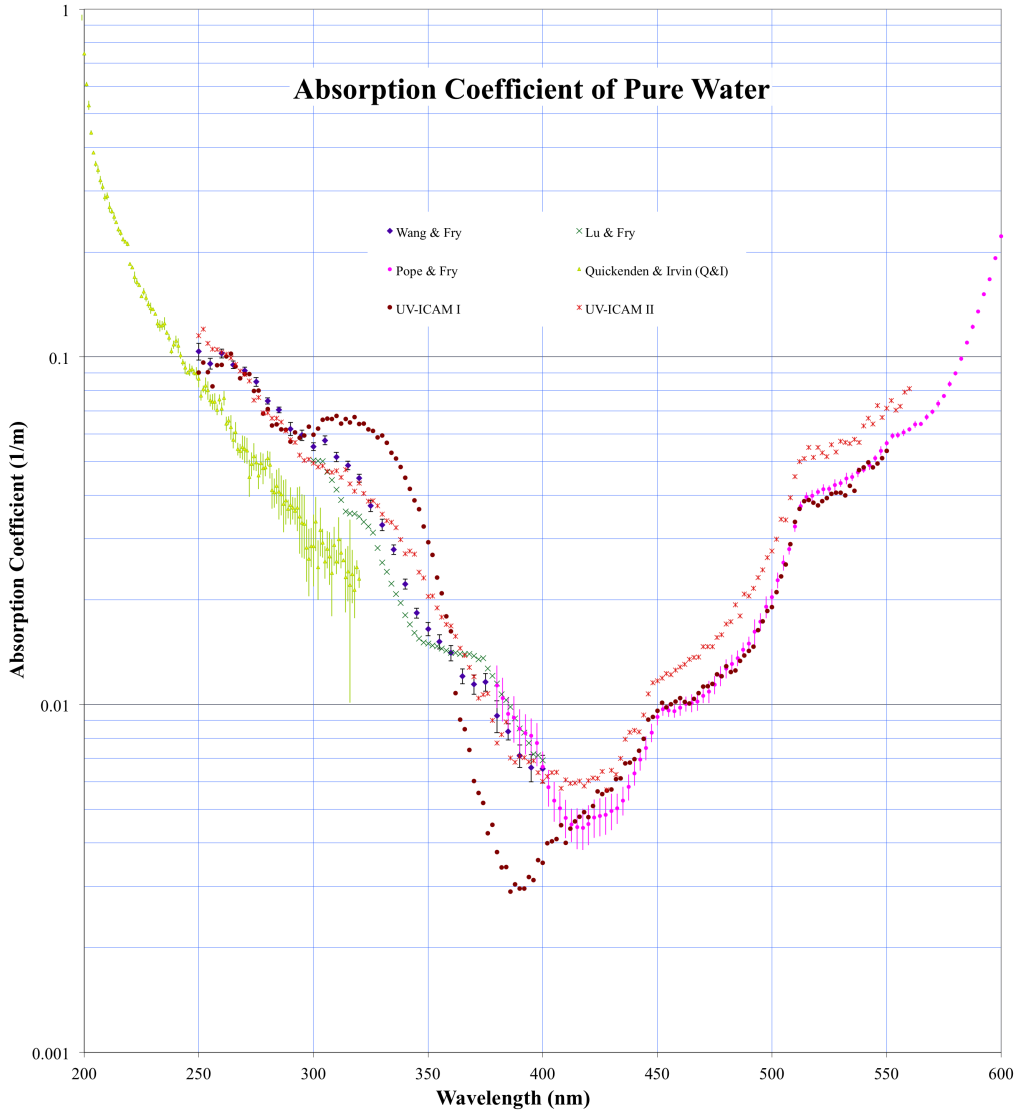

Figure 3.6: Summary of the results for various ICAM experiments. The results of Quickenden *et al.* for the absorption coefficient of pure water in the UV are also shown.[29]

4. INTEGRATING CAVITY RING-DOWN SPECTROSCOPY

4.1 Cavity Ring Down Spectroscopy

When discussing the absolute reflectivity measurements in Sec: 2.7, we briefly mentioned the CRDS technique. We will now discuss CRDS in a bit more detail. Figure 4.1 shows a basic setup for a CRDS measurement. A temporally short laser pulse is introduced into a high-finesse cavity, and allowed to decay. This decay is measured by observing the intensity of light leaving one of the cavity mirrors over time.

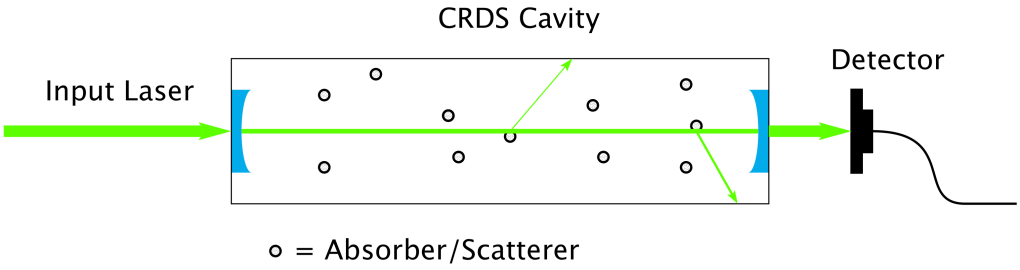

Figure 4.1: Diagram of a generic CRDS cavity.

If an absorber is present in the cavity, the decay constant will be reduced in accordance with the relation,

$$\tau = \frac{t_r}{2[-\ln\rho + al]}, \tag{4.1}$$

where t_r is the roundtrip time, ρ is the mirror reflectivity, l is the cavity length, and a

is the absorption coefficient.[23,24] Thus, the absorption coefficient for a sample placed in this cavity can be deduced by comparing the empty cavity decay constant τ_{empty}, to the decay constant for the sample τ_{sample}. Using Eq. 4.1, it is trivial to show that the absorption coefficient a_{sample} is given by

$$a_{sample} = \frac{1}{c}\left(\frac{1}{\tau_{sample}} - \frac{1}{\tau_{empty}}\right), \tag{4.2}$$

where we have used $c = {}^{2l}/_{t_r}$, and assumed that the sample uniformly fills the entire cavity length l.

In CRDS it is the temporal behavior of the cavity that is being measured, so there is an inherent insensitivity to fluctuations in source intensity. However, in order to ensure exponential decay inside the cavity, it is important that the source has a linewidth narrower than the width of the absorption features being measured. The minimum absorbance detectable by CRDS was shown by Zalicki *et al.* to be given by the expression,

$$al_s = (1-\rho)\left(\frac{\Delta\tau}{\tau}\right), \tag{4.3}$$

where a is the absorption coefficient, l_s is the length of the sample inside the cavity, and $\Delta\tau$ is the decrease in the decay constant when the sample is placed in the cavity. They also give an estimate for this based on the reported accuracy possible for determining the ring-down time. With $\left({}^{\Delta\tau}/_{\tau}\right)_{min} \approx 3\text{x}10^{-3}$, and mirror reflectivities as high as 0.9999 (in the visible), Eq. 4.3 gives a minimum detectable absorbance of $3\text{x}10^{-6}$.[24] Thus, the CRDS technique provides an exceptional method for measuring extremely low absorption coefficients when the species being measured is abundant, or strong absorption coefficients when the species is present in only trace amounts.[37]

The high sensitivity of CRDS makes it an excellent technique for absorption

spectroscopy, but it does have two significant complications. The first is that the cavity must be precisely locked to the input laser mode, and therefore the cavity must be adjusted if the input wavelength is changed. This makes scanning over a range of wavelengths more difficult. Another issue is the way the cavity ring-down signal relates to the absorption coefficient. Introducing an absorbing sample into a high-finesse cavity will reduce the decay constant for the cavity, but this reduction is due to the total attenuation inside the sample, not just the absorption (see Fig. 4.1). Thus, CRDS actually provides a direct measurement of the attenuation coefficient. In the case where scattering is negligible this will indeed give a good direct measurement of the absorption coefficient. However, when the amount of scattering is significant the a in Eq. 4.1 must be replaced with the attenuation coefficient, and the scattering must be either independently measured, or corrected for to get a.

4.2 Integrating Cavity Ring-Down Spectroscopy

We are introducing a new version of CRDS called integrating cavity ring-down spectroscopy (ICRDS) that eliminates both of the complications discussed in the previous section. Figure 4.2 shows a cross section of a generic ICRDS cavity. The input pulse is delivered via a fiber into the sample region of an integrating cavity. A second fiber samples the ring-down of the irradiance on the cavity wall.

The issue of mode-locking is solved because integrating cavities, owing to the disordered makeup of the diffuse reflecting wall structure, have no preferred modes. In principle, an ICRDS cavity can be used over the entire wavelength range for which the wall reflectivity is sufficiently high. In addition, after several reflections of the input pulse the light field inside the integrating cavity is essentially isotropic, so there are no effects due to any scattering present in the sample. This means that ICRDS provides a true direct measurement of the absorption coefficient, even in the presence

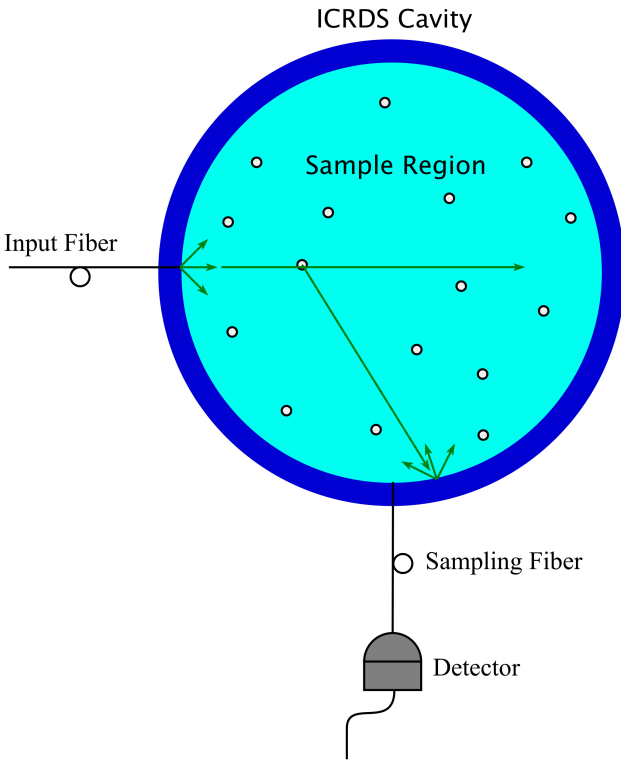

Figure 4.2: Diagram of a generic ICRDS cavity.

of strong scattering.

For samples with negligible scattering, traditional CRDS will always, in principle, be able to outperform ICRDS whenever the cavity mirror reflectivity exceeds the diffuse reflectivity for the integrating cavity wall. This is the case in the visible spectrum, where mirror reflectivities can easily exceed 0.9999. However, mirror reflectivities drop off considerably in the UV. Below 355 nm, the best mirrors have reflectivities of 0.995, which is less than the 0.9968 diffuse reflectivity measured for the fumed silica cavity in Ch. 2. Therefore, ICRDS could potentially outperform CRDS, even with negligible scattering effects, in the UV. For the case of strong scattering ICRDS will always outperform CRDS for measuring the absorption coefficient

providing that the cavity reflectivity is sufficiently high.

4.3 Measuring the Cavity Wall-Time

For a typical specular reflection the incoming light is reflected off the surface of the reflector. However, for a diffuse reflector the light actually penetrates into the cavity wall. Individual photons will, in general, scatter off of many particles before finding their way out of the wall. The difference between these two processes was illustrated in Fig. 1.3 in the introduction. It is clear that the light spends some time in the cavity wall, and thus any measurement of the decay time for a cavity with diffuse reflecting walls will include this contribution.

To account for this "wall-time" Eq. 2.11 can be modified as follows,

$$\tau = \frac{1}{-\ln \rho}\left(\frac{\bar{d}}{c} + \delta t\right), \tag{4.4}$$

where δt is the average amount of time the light spends in the wall for each reflection. This modified equation also suggests a method to measure δt. Rearranging Eq. 4.4 as follows,

$$\tau = \left(\frac{-1}{c\ln \rho}\right)\bar{d} + \left(\frac{-\delta t}{\ln \rho}\right) = m\bar{d} + b, \tag{4.5}$$

we have a linear equation in terms of $\bar{d}$, where the slope is given by $m = (\,{}^{-1}\!/_{c\ln \rho})$, and the y-intercept is given by $b = (\,{}^{-\delta t}\!/_{\ln \rho})$. Thus we can make several cavities of increasing size and plot τ versus $\bar{d}$ for the entire set. A linear fit to this data allows for the determination of δt for the cavities.

In Sec. 2.7 we saw that the total effective path length and decay constants for an integrating cavity scale with the reflectivity as ${}^{1}\!/_{(1-\rho)}$. In other words, very small changes in the reflectivity lead to large changes in L_{eff} and τ. In practice, it can be

difficult to reproduce exactly the same reflectivity for multiple cavities, even when they are made the same way. To deal with this issue a single cylindrical cavity was used for the entire experiment. The increase in cavity size was achieved by machining out ever larger cavities after each measurement. The outer diameter of the cylindrical cavity was made large to minimize any effects due to changes in cavity wall thickness. For the data presented here the total wall thickness was never less than 25 mm.

The cavity halves were prepared by taking pre-baked Aerosil EG50 powder and pressing it into solid cylindrical pieces at a pressure of ∼85 psi. These two cylindrical halves were then baked at 1000° C for 10 hours. The various interior cavity sizes were then machined out using a mill.

The setup for the experiment was essentially identical to Fig. 2.14. The input pulse was the 532 nm frequency doubled output from a Continuum Powerlite 9010 Nd:YAG. A set of 200 μm core multimode-fibers were used to couple the input pulse into the cavity, and sample the output ring-down signal. The output signal was measured using a 1P21 PMT. Each cavity size produced its own ring-down curve that was fit with the convolution fit function given in Eq. 2.13 to calculate its decay constant τ. Figure 4.3 shows the decay constants for the various cavities versus the average distance between reflections $\bar{d}$, for each cavity. The geometry of each cavity size was a right-circular cylinder with $D = H$, so Eq. 2.12 yields $\bar{d} = (2/3)\, D$. The linear least squares fit to the data gives a slope of $m = 3.45 \pm 0.09$ ns/mm, and a y-intercept of $b = 4.0 \pm 2.6$ ns. Using Eq. 4.5, this leads to a cavity wall-time of $\delta t = 3.9 \pm 2.5$ ps.

A second method for calculating the cavity wall-time involves filling the cavity with a dilute dye solution of known concentration. The dye solution consists of Irgalan Black, a water-soluble powder, and Type I ultra pure water produced from a Millipore Gradient water system. When the cavity is filled with such a solution

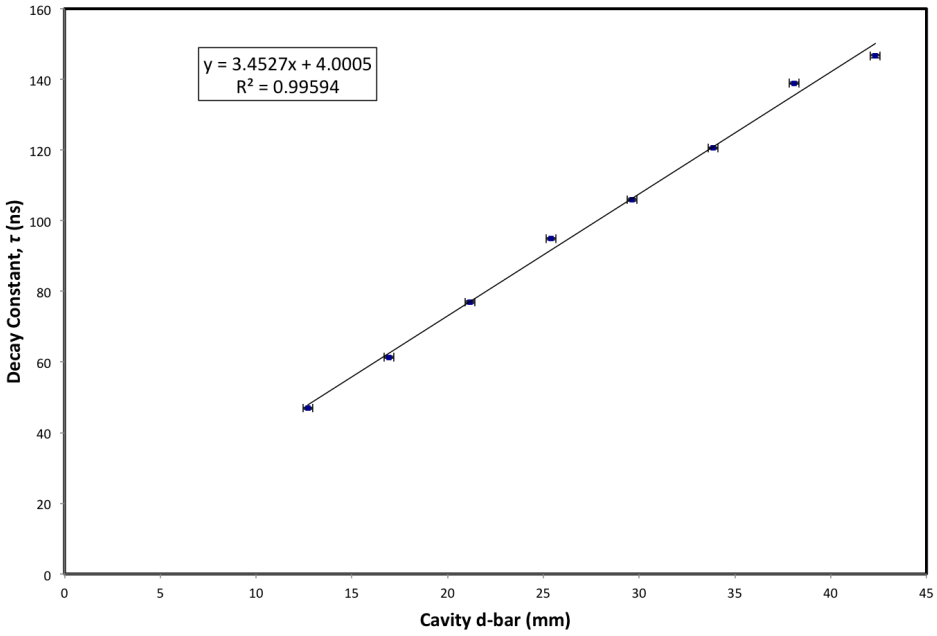

Figure 4.3: Plot showing the decay time τ vs. the cavity $\bar{d}$ for a single fumed silica cavity that has been machined with an increasing inner diameter. A linear fit to the data is also shown.

Eq. 4.4 becomes,

$$\tau = \frac{1}{-\ln \rho + (a_{water} + a_{dye})} \left(\frac{\bar{d}}{c_{water}} + \delta t \right), \tag{4.6}$$

where a_{water} is the absorption coefficient for water, a_{dye} is the absorption coefficient for the dye, and c_{water} is the speed of light in water. This equation can be rearranged to give,

$$\frac{1}{\tau} = \frac{\bar{d}}{\left(\frac{\bar{d}}{c_{water}} + \delta t \right)} a_{dye} + \frac{\left(a_{water} \bar{d} - \ln \rho \right)}{\left(\frac{\bar{d}}{c_{water}} + \delta t \right)}. \tag{4.7}$$

Equation 4.7 shows a linear relation between the absorption coefficient of the dye,

and the inverse of the decay constant.

In order to measure δt, a master dye solution was made using the Irgalan Black powder and ultrapure water. The absorption coefficient for this master dye was measured using an Agilent 8453 UV-VIS spectrophotometer. Dilutions were made by pipetting small amounts of the master dye into additional ultrapure water.

The cavity for this experiment was a 52 mm spherical cavity made from pre-baked Aerosil EG50 fumed silica powder. The powder was packed into a quartz glass mold, and then baked at 1000° C for 10 hours. In order to contain the dye solution a 52 mm OD (50 mm ID) hollow fused silica sphere was placed inside the cavity to act as a sample holder. The solution was added to the sample holder with a glass syringe.

The ring-down curve for the cavity was measured for each of these diluted dye samples, and that curve was fit using Eq. 2.13 to calculate the decay constant. The inverse of these decay constants versus the measured absorption coefficients for the various dye dilutions is plotted in Figure 4.4. A linear least-squares fit to this data, along with Eq. 4.7 yields a wall-time of 9.2 ± 0.6 ps.

The two methods described above give different values for δt, but this is not unexpected. The wall-time is likely to be highly dependent on the nature of the cavities manufacturing. The two cavities used for these methods were made in different ways (one was machined, while the other was molded). They were also packed at different pressures, which may result in different spacing between adjacent quartz powder particles. One reason for this difference in pressure is that the molded cavities require a lower packing pressure to avoid destroying the quartz glass mold that forms the inner cavity surface. Nevertheless, the two values are of the same order, and demonstrate that the cavity wall-time is an important quantity to consider for ICRDS measurements. The cavity dye measurements also show a basic proof of principle that ICRDS is easily capable of distinguishing small differences in absorption for samples with

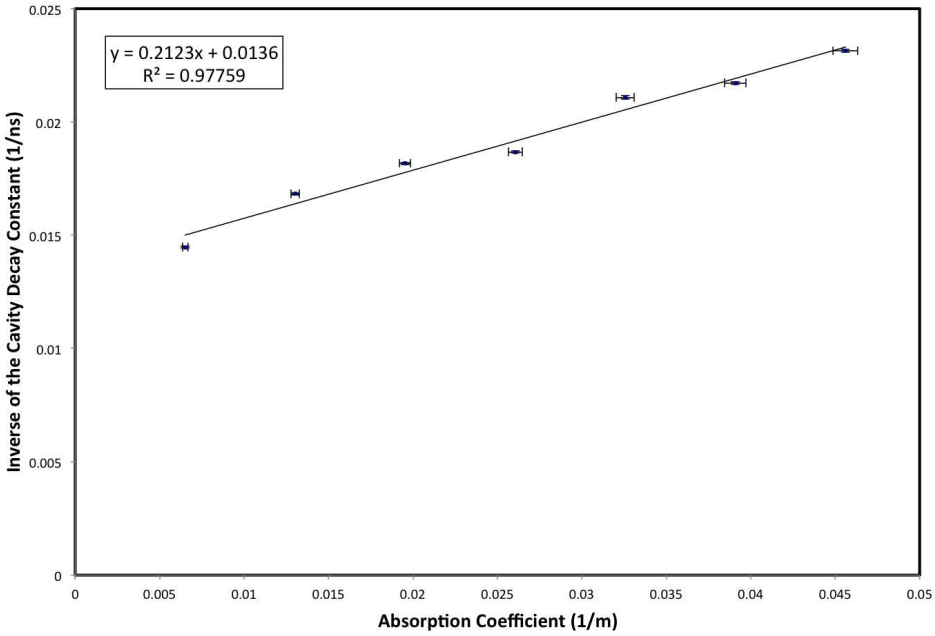

Figure 4.4: Plot showing the inverse of the decay time, $1/\tau$, vs. the absorption coefficient of a dye solution inside the cavity. A linear fit to the data is also shown.

very low absorption coefficients (the two lowest concentration dyes in Fig. 4.4 have absorption coefficients of 0.0130 and 0.0065 m^{-1} at 532 nm, respectively).

5. INTEGRATING CAVITIES: APPLICATIONS

In this final chapter we will discuss some of the practical applications for this new diffuse reflector. Numerous applications have been explored, but the three presented here all involve integrating cavities made from the fumed silica. The first two applications merely exploit the isotropic field provided by an integrating cavity, and the very long effective optical path lengths for a very high-reflectivity diffuse reflecting wall. In other words, the cavity is providing signal enhancement. The final application demonstrates the first real-world application of the ICRDS technique. This involves measuring the absorption coefficient of biological samples.

5.1 Cavity Enhanced Raman Scattering

Raman spectroscopy is a very powerful tool that has found extensive use in the fields of chemistry, physics, and the biomedical sciences. It is based on Raman scattering, which involves the inelastic scattering of incident photons off a molecule. Figure 5.1 shows the basic energy level scheme for both Rayleigh and Raman scattering. In Rayleigh scattering, incident photons of energy $\hbar\omega_I$ interact with the molecule and excite a virtual state. This excited state is very short-lived, and the photon is re-emitted (scattered) with the same energy as the incident photon. Thus, Rayleigh scattering is an elastic process. For Raman scattering, the process is inelastic and the scattered photon can either lose energy (Stokes Raman scattering), or gain energy (anti-Stokes Raman scattering). The difference between the incident and scattered photon energy is known as the Raman shift.[38–40]

Raman scattering involves the vibrational energy levels of the molecule, which are specific to the chemical bond structure and symmetry of the individual molecular species. Therefore, the Raman shift provides spectroscopic fingerprints by which

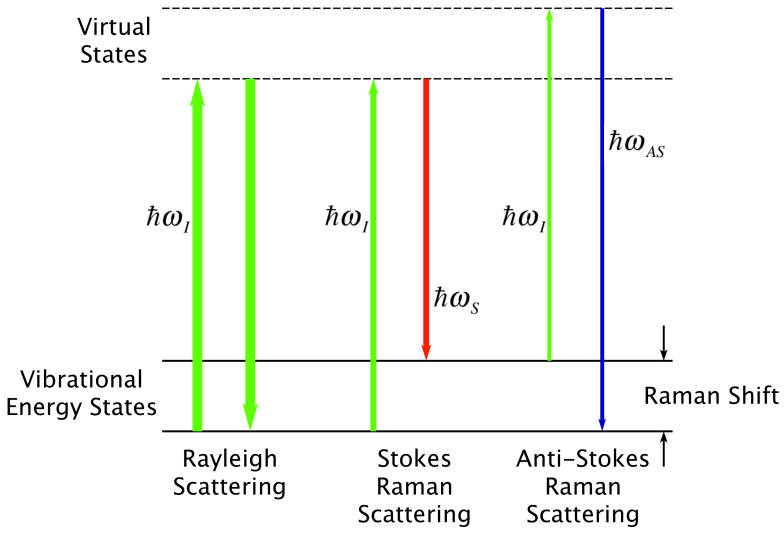

Figure 5.1: Energy level scheme describing Rayleigh (elastic), and Raman (inelastic) scattering.

specific molecules can be identified. This is however, complicated by the fact that the Raman shifted signal can be difficult to measure. Typically, only about 1 in 10 million photons will scatter via Stokes Raman scattering. The vast majority will simply undergo Rayleigh scattering. The amount of photons that undergo the anti-Stokes process is even less. This means that the Raman signal will typically be drowned out by the overwhelming Rayleigh signal. This issue can be alleviated by filtering out the elastically scattered light with a Raman filter. However, for very small sample sizes, the amount of Raman shifted light will still be quite low.

An integrating cavity can allow for an enhanced Raman signal due to the long effective optical path it provides. In addition, the cavity both illuminates the sample, and collects the scattered light from the sample isotropically. This means that both the excitation, and collection efficiencies are improved. We used this technique to look at atmospheric Raman scattering in an empty cavity, and to detect the Raman

signal from small samples of several toxins.

The setup involved a fumed silica integrating cavity with a inner cavity diameter of 52 mm. It was prepared and manufactured in an identical manner to the machined cavities described in Sec. 2.6, and was baked for 10 hours at 1000° C. A small (∼1-2 mm) aperture was machined in the top half of the cavity to allow for both the input pump, and output detection. The source was a 100 mW, 532 nm diode pumped Nd:YVO4 continuous wave laser. A dichroic mirror at 45% and an aspheric condenser lens were used to direct the pump beam into the cavity aperture. The Raman emission leaving the aperture was collected using the same aspheric condenser lens. This light passes through the dichroic, and is focussed onto a fiber bundle that launches it into a 0.3 m Acton spectrometer.

Figure 5.2 shows the spectra for the empty cavity plotted as the intensity recorded by the spectrometer for a given Raman shift. The conversion between the wavelength spectrum and the Raman shifted spectrum is given by,

$$\text{RamanShift}(\text{cm}^{-1}) = \left(\frac{1}{\lambda_s(\text{nm})} - \frac{1}{\lambda_r(\text{nm})}\right) \times \left(\frac{10^7(\text{nm})}{(\text{cm})}\right), \tag{5.1}$$

where λ_s is the source wavelength, and λ_r is the wavelength of the Raman scattered light. The two peaks at 1556 cm^{-1} and 2330 cm^{-1} correspond to the Raman signals for atmospheric oxygen and nitrogen, respectively. Thus we see that the cavity enhancement allows for easy detection of the Raman scattered light from these atmospheric components without any need for pressurization.

FIgure 5.3 shows the same empty cavity spectrum, but this time the background due to the cavity is subtracted using a method based on polynomial least-squares fitting.[41] The structure on either side of the 1556 cm^{-1} peak is an artifact of the spectrometer, and shows up in all the spectra for these experiments.

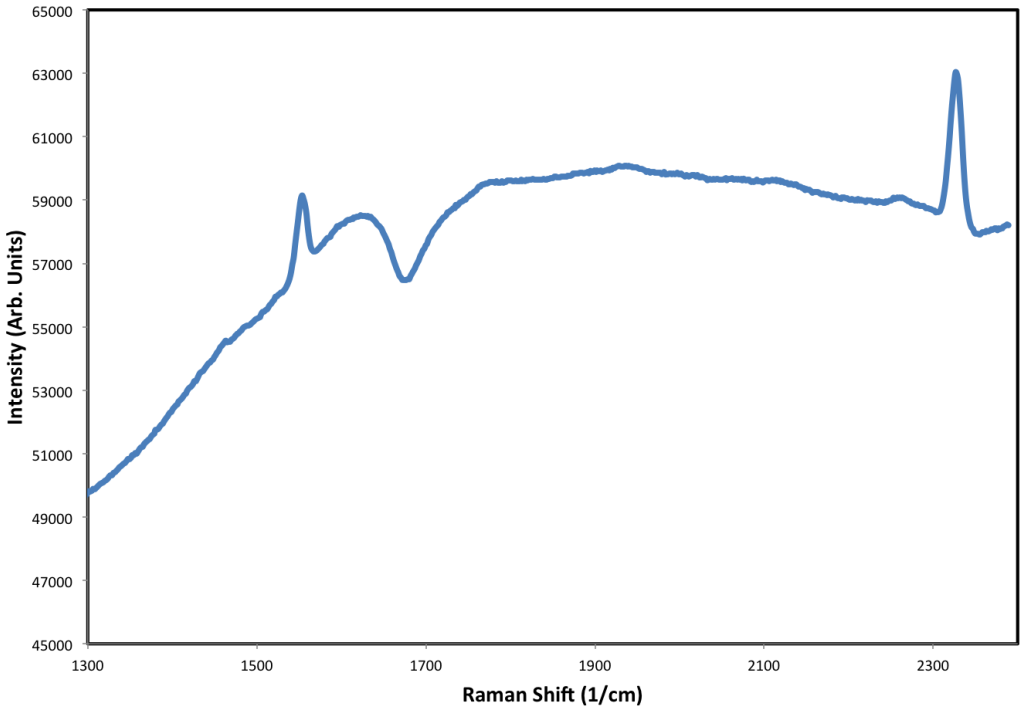

Figure 5.2: Raman shifted spectra for the empty fumed silica integrating cavity. The peaks at 1556 cm^{-1} and 2330 cm^{-1} correspond to the Raman signal for oxygen and nitorgen.

The three toxins tested were Benzo[a]pyrene (BaP), Napthalene, and Pyrene, all of which have been shown to have toxicity or carcinogenic properties. Measured samples of each toxin were placed in a high-purity fused silica crucible that was then set inside the integrating cavity. Figure 5.4 shows the Raman shifted spectrum for the cavity with a sample of 400 μg of the BaP, along with the empty cavity spectrum. The peak at 1380 cm^{-1} corresponds to the the Raman shifted signal for the BaP. Figures 5.5 and 5.6 show similar spectrum plots for 550 μg of Napthalene, and 510 μg of the Pyrene, with the corresponding peaks at 1377 cm^{-1} and 1400 cm^{-1}, respectively.

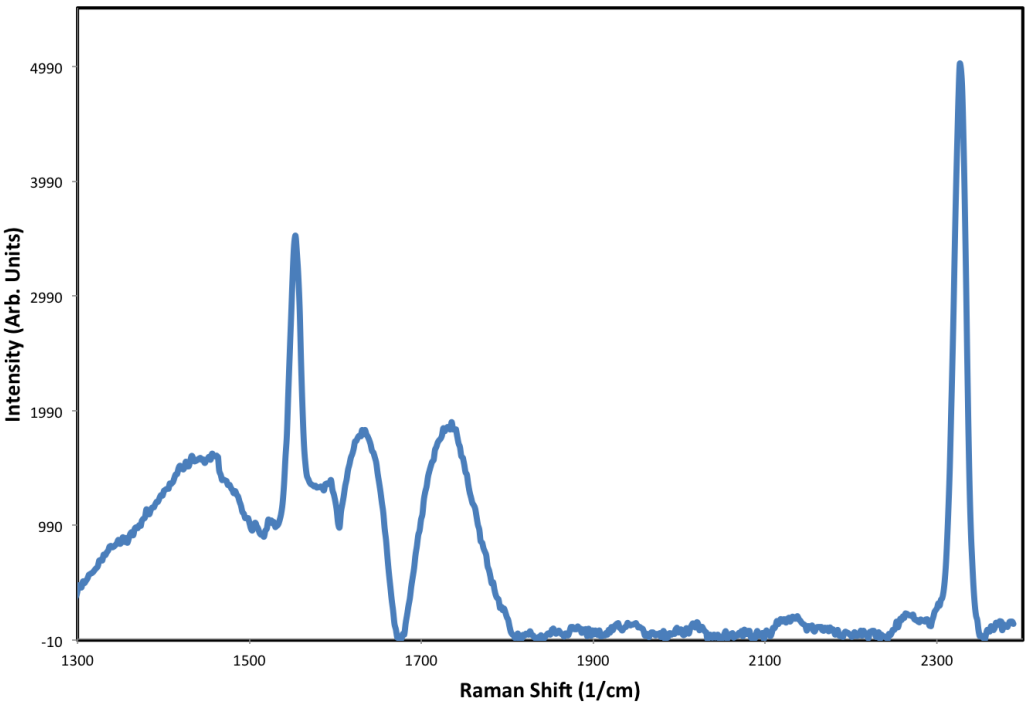

Figure 5.3: Raman shifted spectra for the empty fumed silica integrating cavity with the background subtracted. The peaks at 1556 cm^{-1} and 2330 cm^{-1} correspond to the Raman signal for oxygen and nitorgen.

Figure 5.7 shows a plot of the intensity of the Raman signal versus the mass of the BaP toxin in the cavity. All of the data points on this plot were normalized to the intensity of the oxygen peak at 1556 cm^{-1}. This was done to account for any changes in the signal strength due to variations in the alignment of the quartz crucible sample holder with respect to the input pump beam. Figures 5.8 and 5.9 are similar plots for the Napthalene and Pyrene toxins.

Looking at Fig. 5.7- 5.9, we see that this cavity enhanced Raman spectroscopy technique is easily capable of detecting small amounts of toxin inside the cavity. These amounts are as small as 200 μg for the Napthalene, and 100 μg for BaP and

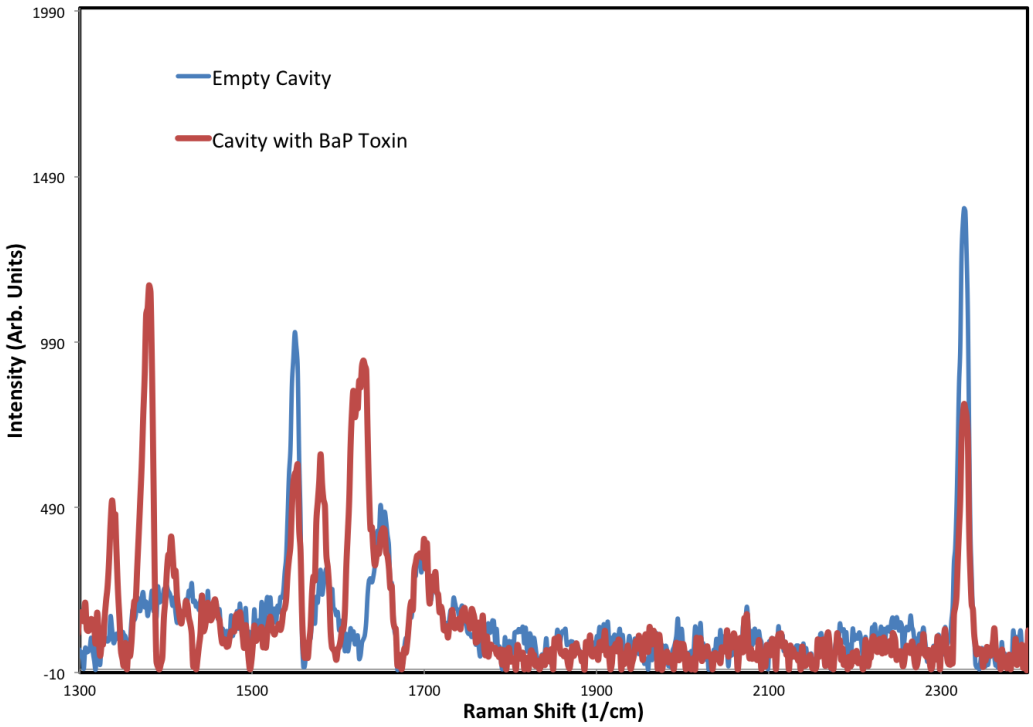

Figure 5.4: Raman shifted spectra for the empty fumed silica cavity (blue), and the cavity with the BaP toxin. The peak at 1380 cm^{-1} corresponds to the Raman signal for the BaP toxin.

Pyrene. Without the cavity enhancement the Raman signals for such small quantities of these toxins would be below the threshold of detection. Simple improvements, like increasing the input pump power, and shifting to a shorter wavelength to increase the Raman scattering cross section should allow for detection of even smaller amounts.

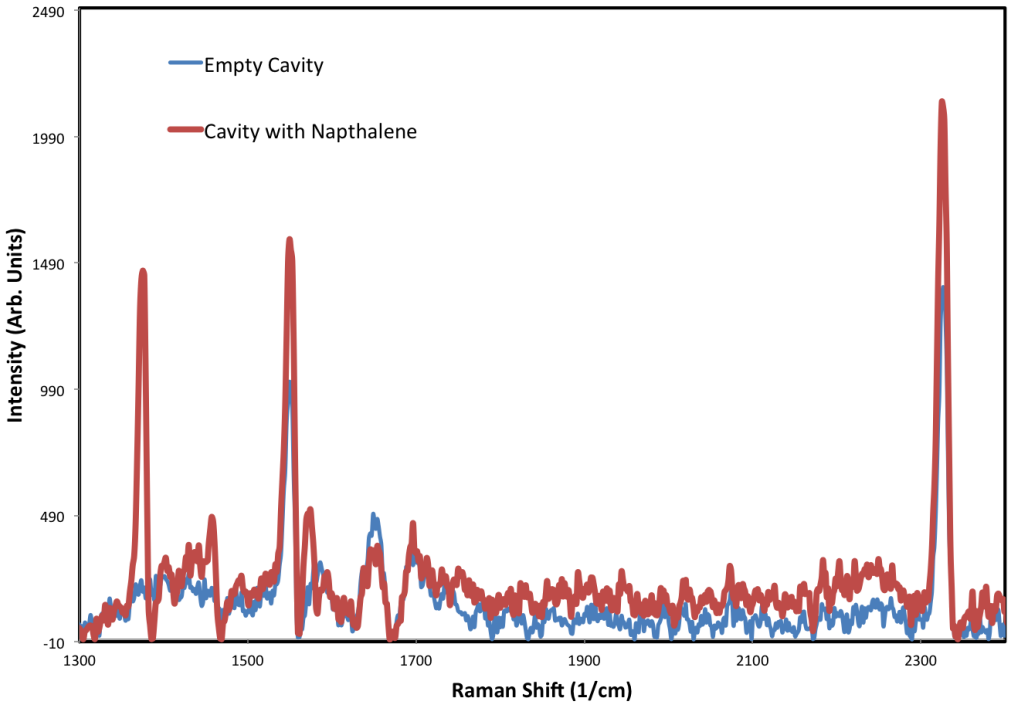

Figure 5.5: Raman shifted spectra for the empty fumed silica cavity (blue), and the cavity with the Napthalene toxin. The peak at 1377 cm^{-1} corresponds to the Raman signal for the Napthalene toxin.

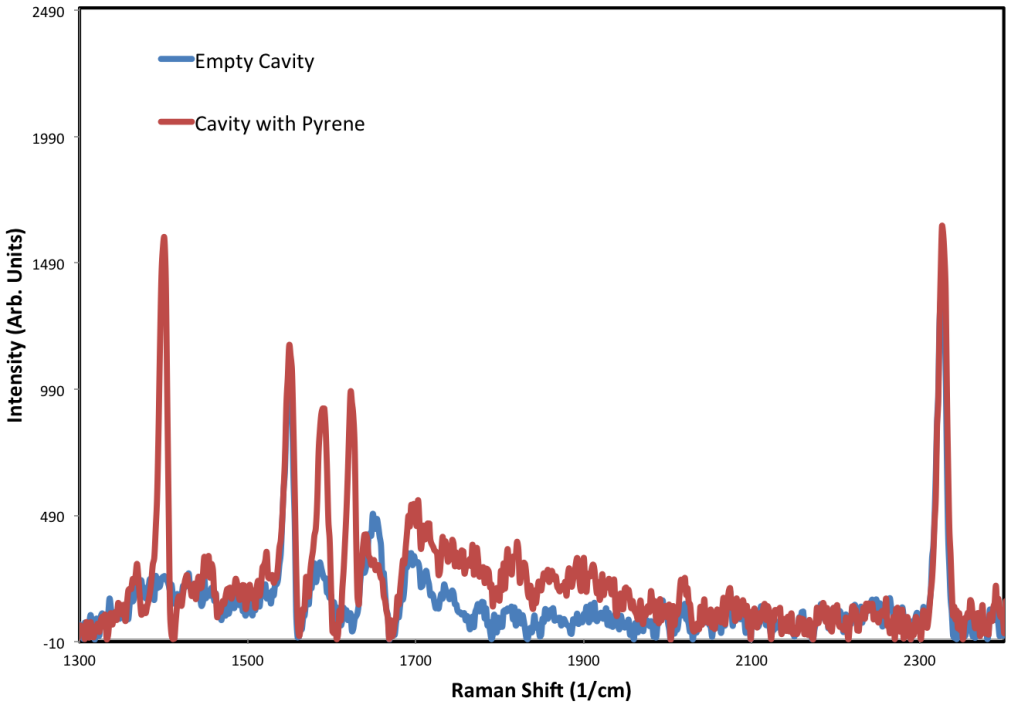

Figure 5.6: Raman shifted spectra for the empty fumed silica cavity (blue), and the cavity with the Pyrene toxin. The peak at 1400 cm^{-1} corresponds to the Raman signal for the Pyrene toxin.

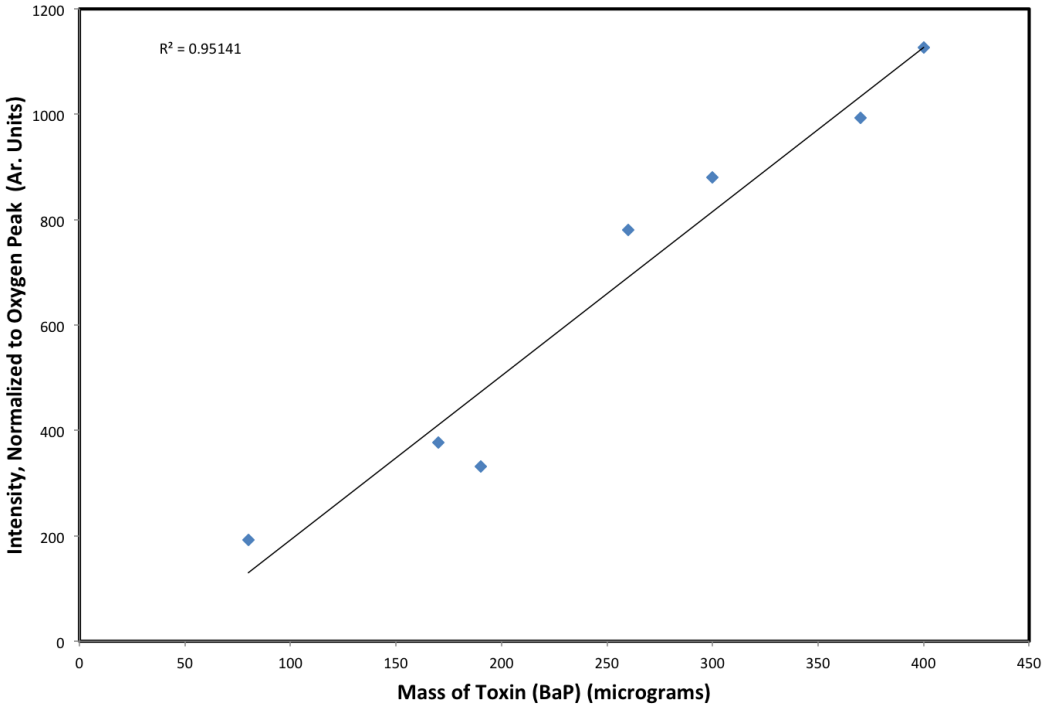

Figure 5.7: Plot showing the intensity of the Raman shifted signal vs. the mass of BaP toxin in the cavity. Each data point has been normalized to the Oxygen peak in order to eliminate changes in signal strength due to alignment of the crucible holding the toxin.

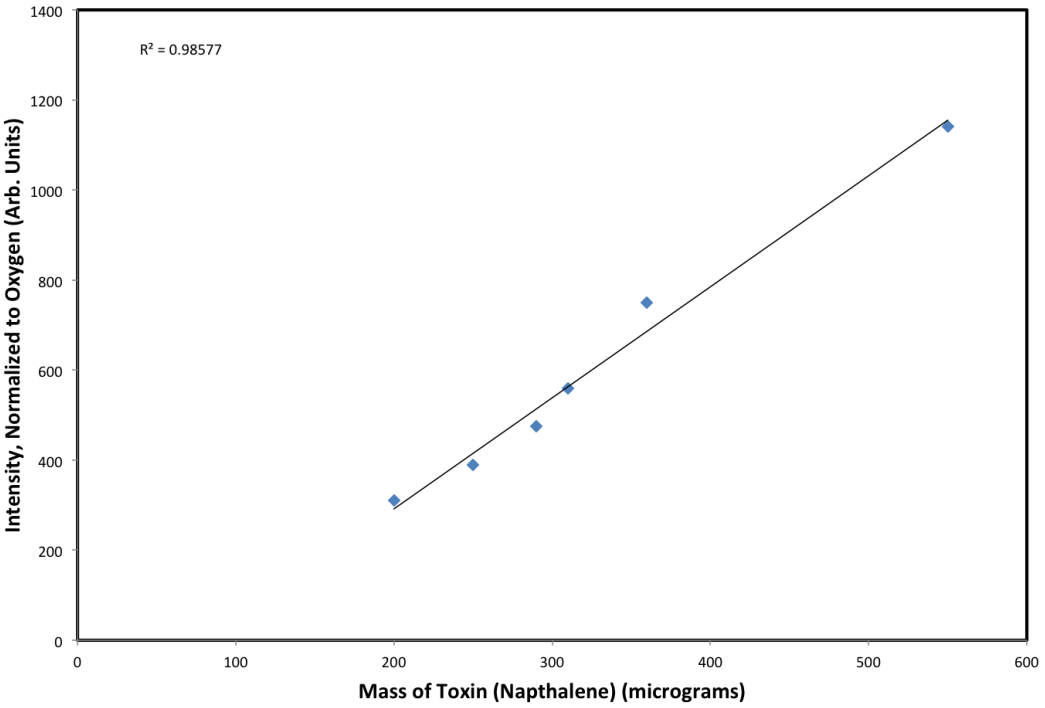

Figure 5.8: Plot showing the intensity of the Raman shifted signal vs. the mass of Napthalene toxin in the cavity. Each data point has been normalized to the Oxygen peak in order to eliminate changes in signal strength due to alignment of the crucible holding the toxin.

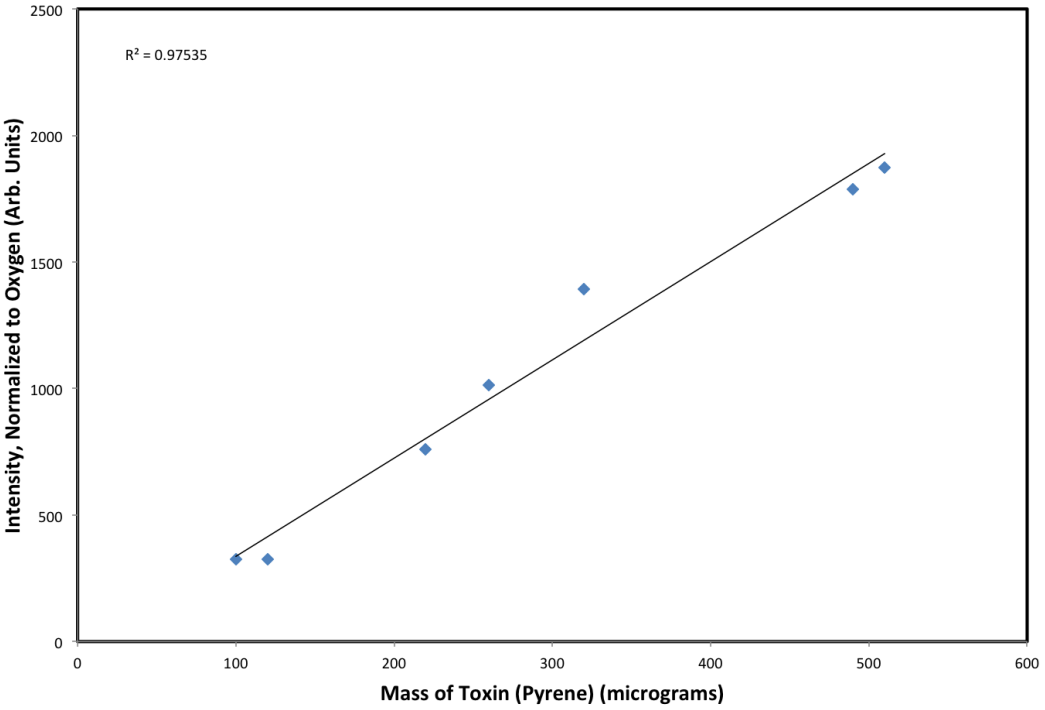

Figure 5.9: Plot showing the intensity of the Raman shifted signal vs. the mass of Pyrene toxin in the cavity. Each data point has been normalized to the Oxygen peak in order to eliminate changes in signal strength due to alignment of the crucible holding the toxin.

5.2 Cavity Enhanced Fluorescence Measurements*

In the previous section we used a fumed silica integrating cavity to enhance the Raman shifted signal for atmospheric oxygen, atmospheric nitrogen, and several organic toxins. In this section we will see that the same integrating cavity can be used to enhance the fluorescence signal of samples inside the cavity.

The detection of contaminants in water supplies is an issue of great significance throughout the world. Animal and human waste (i.e. feces, and urine) are obvious examples that are particularly important due to their potential to cause the spread of disease. One indicator that has been shown to be helpful in the detection of such waste in water supplies is the biochemical urobilin.[43] Urobilin is one of the final by-products of hemoglobin metabolism, and is excreted in both the urine and feces of many mammals, including both humans and common livestock.[44] Urobilin can also be an indicator of disease, such as hepatic dysfunction, or jaundice. Thus, an ultra-sensitive technique for the detection and quantification of urobilin in solution has both diagnostic and environmental applications.

Urobilin detection in solution has previously been demonstrated using the formation of a phosphor group from the combination of urobilin and zinc ions.[45] Normal heme catabolism results in the production of bilirubin, which is then broken down into stercobilin and urobilin. Both urobilin and stercobilin have been shown to be viable biomarkers for detection of fecal pollution levels in rivers.[46]

Fluorescent detection of urobilin in urine has been demonstrated based on the Schlesinger's reaction in which an urobilinogen-zinc chelation complex exhibits a characteristic green fluorescence when excited by blue light.[47] Methods for detection of urobilinoids using high-performance liquid chromatography with a reverse-phase

*The work described in this section has recently been submitted and accepted for publication.[42]

column and an ultraviolet detector have also been presented, however, the initial sensitivity of this method proved insufficient for clinical analysis.[48] Miyabara *et al.* reported an increase in detection sensitivity of this methodology, but only to detection levels of 1.5 nM, where efficient illumination and collection of the fluorescent signal were the limiting factor.[45] Traditional epi-illumination fluorescence spectroscopy systems utilize an objective lens to focus excitation light into the sample and collect the fluorescence emission. For these configurations, the signal generated is limited to the focal volume of the optics. Since the generated signal is diffuse in nature, only a small fraction of the total emitted light is collected. Only a small volume of the sample can be probed at any given time with this type of configuration, so detection of sub-nanomolar concentrations is difficult. A method that allows for probing a larger volume of the sample, or better yet, the entire sample could significantly enhance the ability to detect sub-nanomolar concentrations of urobilin. If the method also allows for more efficient collection of the diffuse fluorescence emission, then the enhancement would be even more significant. As we saw in the previous section, a high-reflectivity integrating cavity can provide both of these desired enhancements.

The integrating cavity used for these experiments was manufactured in the manner described in Sec. 2.6, and baked at 930° C for several hours. After the bakeout, the cavity halves were machined to form a right-circular cylindrical inner cavity with a diameter and height of 50.8 mm. Figure 5.10 is a diagram showing a cross section of the cavity. The sample holder depicted inside is the quartz crucible that was used to hold the sample solutions. A ∼2.0 mm hole was machined into the top half of the cavity to allow for coupling light into and out of the cavity.

The excitation source for the experiment was a 5 mW LED (Radio Shack #276-316) centered at 468 nm. The output of the LED was sent through a bandpass filter to limit its inherently broad output spectrum. A 490 nm long pass filter angled at 45°

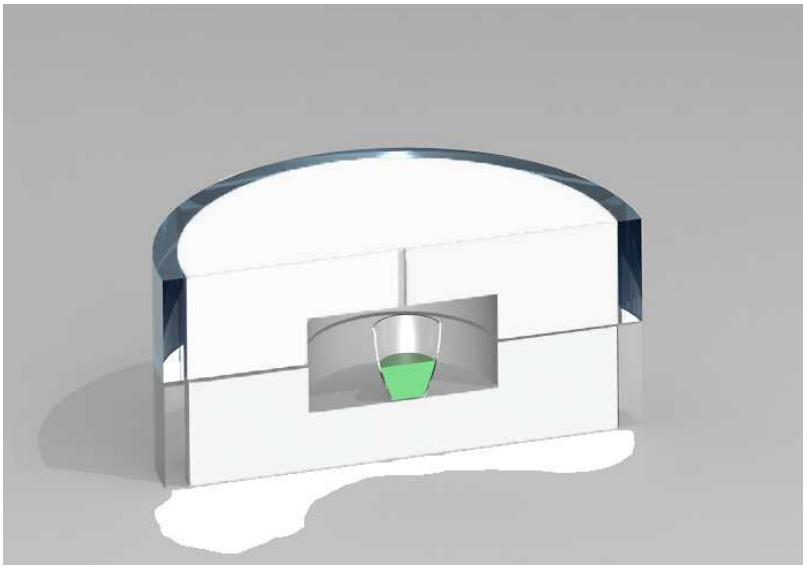

Figure 5.10: Diagram showing a cross section of the cavity setup. The quartz crucible used as a sample holder is shown below the aperture hole in the cavity.

was used to direct the excitation source to a 20 mm focal length aspheric condenser lens. This setup delivered approximately 420 μW of light into the integrating cavity. The same condenser lens was used to collect the fluorescent emission. This light was sent through a 500 nm long pass filter before being imaged into an Acton 0.3 m CCD spectrometer. Figure 5.11 shows the actual integrating cavity in the experimental setup. The blue excitation light can be seen entering the cavity from the top, while the green fluorescence can be seen along the seam between the two cavity halves. This image was taken with a very high concentration of the fluorescent solution, which is why the fluorescence is so easily visible.

A stock solution of urobilin was prepared by dissolving 1.1 mg of urobilin hydrochloride in 20 ml of ethanol. This solution was then diluted down to a concentration of 1 μM urobilin. 11.25 mg of zinc acetate was added to the solution to allow for phosphor formation. The samples were prepared from this final stock solution,

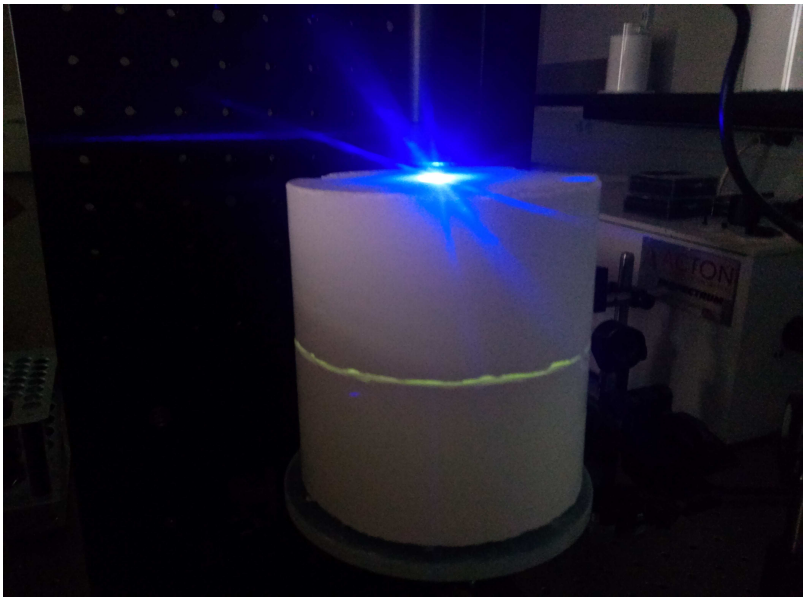

Figure 5.11: Image of the integrating in the experimental setup. The excitation source (blue light) can be seen entering the cavity. The green band visible is from a high concentration of the urobilin in solution.

and had concentrations ranging from 100 nM to 500 fM.

Fluorescence spectra were recorded for the various concentrations. Figure 5.12(A) shows a typical set of excitation and emission spectra. The spectra of the empty cavity and the ethanol buffer were also measured and used for background removal. Integration times of 100 ms were used for the 100, 10 an 1 nM concentrations, and 500 ms for all other concentrations. Figure 5.12(B) shows the fluorescence signal for each concentration. The intensity at each concentration was calculated by integrating the area under the emission curve after the removal of the ethanol buffer background signal. The data point for each concentration represents the average of five measurements. These results show that the urobilin fluorescence signal was detectable down to a concentration of 500 fM. It should be noted that, even at this very low concentration sufficient signal remained to suggest that detection at even

lower concentrations may be possible. In addition, these measurements are both simple and fast. There is no need for an expensive, or complicated laser source, and the data acquisition allows for near real-time measurements.

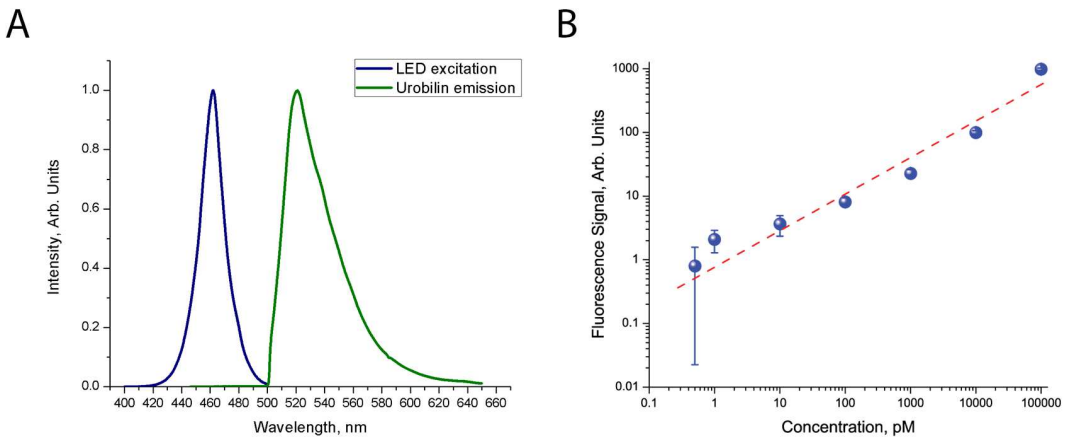

Figure 5.12: (A) Excitation and emission spectrums for the LED and urobilin fluorescence. The blue trace shows the LED emission after it went through a bandpass filter. The green trace shows the typical fluorescence observed from the cavity. (B) Fluorescence counts plotted against concentration following cavity and ethanol background removal and correction for varying acquisition times on the spectrometer. The blue dots indicate the average fluorescence intensity measured for each concentration where the error bars represent standard deviation between samples. The red dashed trace shows a linear fit to this data.

5.3 ICRDS Measurements of RPE Cells

Accurate knowledge of the absorption coefficient of biological cells and their constituents is of great importance in the fields of biology and medicine. Biomedical imaging techniques, modeling of light transport in tissue, and laser-based procedures like laser refractive surgery all depend on this data.[49,50] That being said, much

of the previous work in this area has relied on transmission-style experiments that measure attenuation, as opposed to absorption.[51,52] Biological tissues often produce strong scattering, so the measured attenuation may include a significant contribution from losses due to this scattering.[53] Thus, to find the absorption coefficient these scattering losses must either be independently measured, or numerically modeled.

In Ch. 4 we introduced integrating cavity ring-down spectroscopy as new technique for direct measurement of the absorption coefficient, even for the case of a strongly scattering sample. Therefore, ICRDS seems ideally suited for measuring absorption in biological samples.

We have used the ICRDS technique to measure the absorption coefficient of retinal pigment epithelium (RPE) cells. The RPE is a pigmented layer of cells between the neurosensory retina and the choroid in the eye. It is involved in the nourishment of the retinal photoreceptor cells, and serves as an absorber of scattered light in the eye. The latter property is made possible by the granules of melanin that are packed into the cells.[54–56]

Samples of the RPE cells were prepared in a phosphate buffered saline (PBS) solution. The overall sample size for the RPE cell solution was 3 ml, and contained ∼60 million cells. These samples were pipetted into a quartz crucible which was then placed into a fumed silica integrating cavity (see Fig. 5.10). The integrating cavity used had a cylindrical inner geometry with a 63.5 mm diameter, and a 63.5 mm height.

Clearly the RPE cell sample (3 ml) occupies only a small portion of the the inner cavity volume. This means that two samples of known absorption must be used to calibrate the cavity. In addition to this, a sample of the PBS solution must also be measured so that its contribution to the total absorption coefficient of the sample can be subtracted out.

If we consider Eq. 4.4 for the case of our RPE solution we have

$$\tau_{RPE} = \frac{1}{-\ln\rho + (a_{PBS} + a_{RPE})\,\bar{d}_s}\left(\frac{\bar{d}}{c} + \frac{\bar{d}_s}{c_s} + \delta t\right), \tag{5.2}$$

where τ_{RPE} is the decay constant for the RPE solution, $\bar{d}_s$ is the average distance between reflections in the sample, c is the speed of light in the sample, $\bar{d}$ is the average distance between reflections excluding the distance in the sample, c is the speed of light in air, and a_{PBS} and a_{RPE} are absorption coefficients for the PBS buffer and the RPE cells, respectively. Similarly, for a solution of pure water and dye we have

$$\tau_D = \frac{1}{-\ln\rho + (a_{pw} + a_D)\,\bar{d}_s}\left(\frac{\bar{d}}{c} + \frac{\bar{d}_s}{c_{pw}} + \delta t\right), \tag{5.3}$$

where a_{pw} is the absorption coefficient of pure water, a_D is the absorption coefficient of the dye, and c_{pw} is the speed of light in pure water. Thus, if we measure the decay time for equal volumes of the RPE cell solution, the PBS buffer, and two dye solutions we can use Eqs. 5.2 and 5.3 to derive the following expression for the absorption coefficient of the RPE cells

$$a_{RPE} = \frac{\tau_{RPE}^{-1} - \tau_{PBS}^{-1}}{\tau_{D1}^{-1} - \tau_{D2}^{-1}}\,(a_{D1} - a_{D2})\,. \tag{5.4}$$

It should be noted that in this derivation it is assumed that $c_{pw} \approx c_{PBS}$. This is reasonable, as the PBS solution is simply a water based isotonic solution.

The two dye solutions were prepared by diluting known amounts of a master dye solution in pure water. The absorption coefficient of this master dye was determined separately using a spectrophotometer, and this data was then used to calculate a_{D1} and a_{D2}. The dye used for these experiments was the same Irgalan Black powder used in the ICAM experiments. A more detailed description of the preparation

and measurement of this master dye is given in the ICAM calibration discussion in App. A.

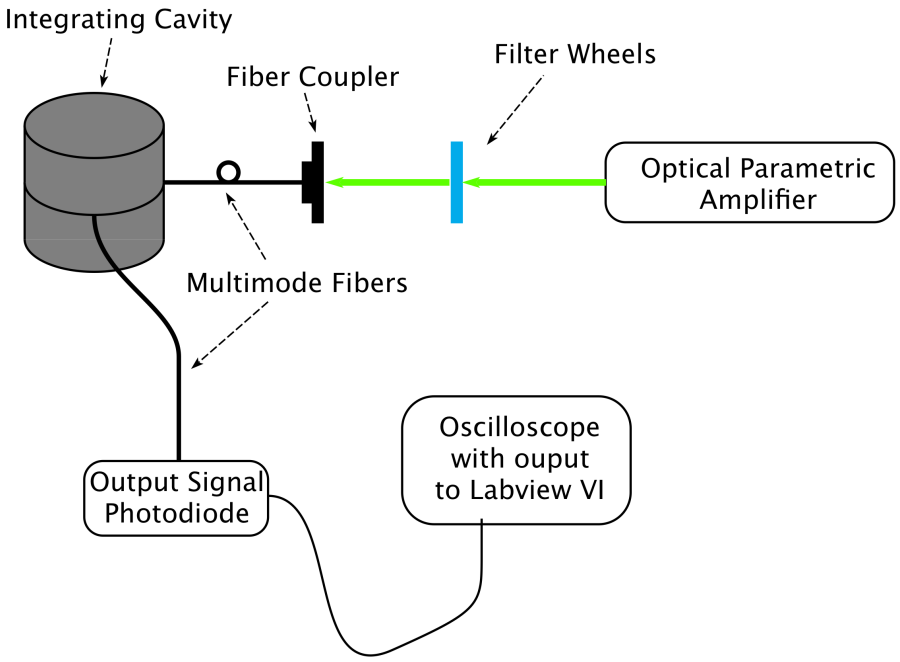

Figure 5.13: Basic setup for the ICRDS measurements of RPE cells.

The basic setup for the experiment is shown in Fig. 5.13. The source was a Pro290 Nd:YAG-pumped QuantaRay OPA that produced a 6 ns pulse, and was tunable over a range of ∼400-800 nm. The beam was attenuated with a filter wheel before being launched into a multimode fiber that was used to couple the input pulse into the integrating cavity. Another multimode fiber sampled the ring-down signal inside the cavity. This signal was sent to a Thorlabs DET 100 photodiode. An oscilloscope and a LabView VI were used to average and record the data.

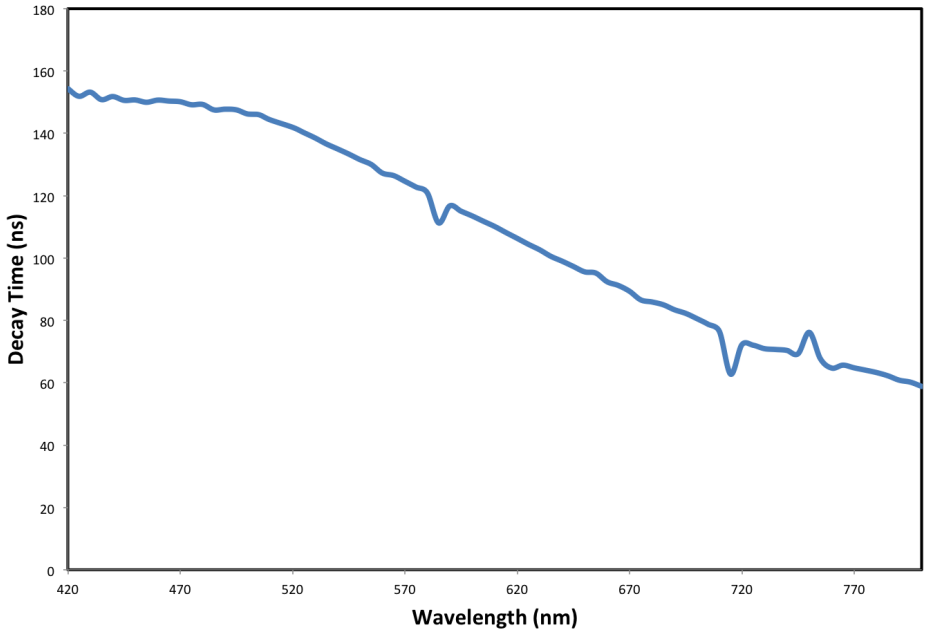

Figure 5.14: Plot of the decay constant vs. wavelength for the empty ICRDS cavity from 420-800 nm.

Figure 5.14 shows a plot of the decay constant vs. wavelength for the empty integrating cavity (i.e. no sample) from 420-800 nm. Based on Eq. 4.4, we can say that this plot is also representative of the cavity reflectivity. All of the decay constants were determined by fitting the corresponding ring-down decay curves with the Gaussian-exponential convolution fit function given in Eq. 2.13. We see that the decay time for the empty cavity, and thus the reflectivity, goes steadily down as we move towards the infrared. This means that our cavity sensitivity will also go down as we move towards the infrared.

Figure 5.15 shows a plot of the decay constant vs. wavelength for 3 ml samples of: the RPE cell solution, the PBS buffer, and two different concentrations of dye solution. For the region from 420-630 nm we see that the cavity can easily distin-

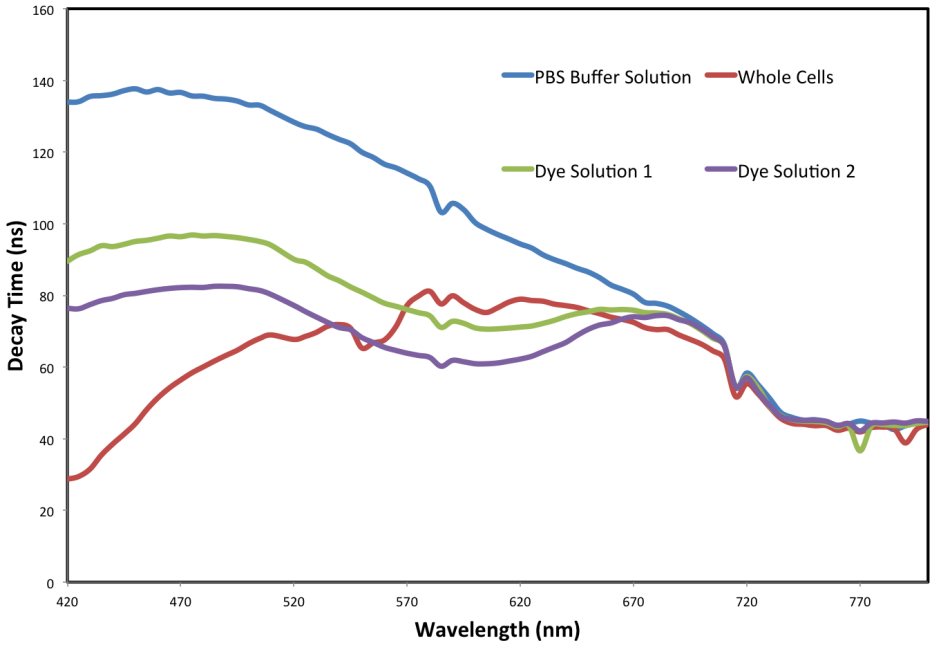

Figure 5.15: Plot of the decay constant vs. wavelength 3 ml samples of: the RPE cell solution, the PBS buffer, and two different concentrations of dye solution.

guish between the various samples. However, above 630 nm we begin to see the curves for all the samples start to converge, and by ∼710 nm they are practically indistinguishable. Notice that these decay constants are still significantly less than the empty cavity decay times. We can make sense of this by considering the two dye solutions. Dye solutions 1 and 2 are 35.7x dilution and 50x dilutions of the master dye, respectively. We see a clear difference between these two dyes below 630 nm, but above 700 nm they give essentially identical decay constants. This suggests three causes that combine to produce the effects seen in Fig. 5.15. First, the decline in the cavity sensitivity reduces its ability to distinguish small differences in absorption. Second, as we move towards the infrared the absorption coefficient of water increases, and eventually becomes the dominant contribution to the absorption of

the various samples. This would explain why all the samples converge, as the PBS buffer is primarily water. Finally, the absorption coefficient of the Irgalan Black dye drops considerably past 650 nm, and remains small into the infrared. This can be seen in Fig. 5.16 which shows the absorbance of the the master dye solution from 250-1000 nm. Due to these issues, only the region from 420-630 nm was considered when calculating the absorption coefficients for the RPE cells.

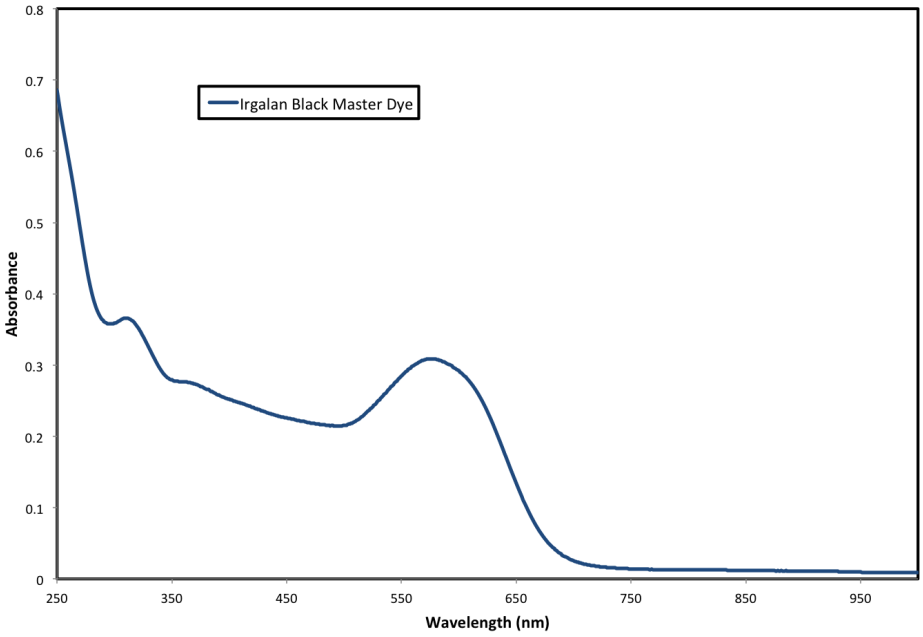

Figure 5.16: The absorbance of the Irgalan Black master dye solution for 250-1000 nm.

Figure 5.17 shows the final results for the absorption coefficient of the RPE cells from 420-530 nm. The values given are for the sample of ∼60 million cells, and not the absorption coefficient for an individual cell. The values can easily be converted

to individual cell numbers using the known concentration of the sample (i.e. 60 million cells diluted to 3 ml in PBS buffer). The errors in the decay constants were determined using 99% confidence intervals for the convolution fits. Additional contributions to the error bars come from the pipetting to make the dye solutions, and the standard deviations in the spectrophotometer measurements. The larger error bars for the shortest wavelengths are primarily due to low signal limitations imposed by the source. Tables 5.1 and 5.2 list the absorption coefficient values from Fig. 5.17 along with their respective uncertainties.

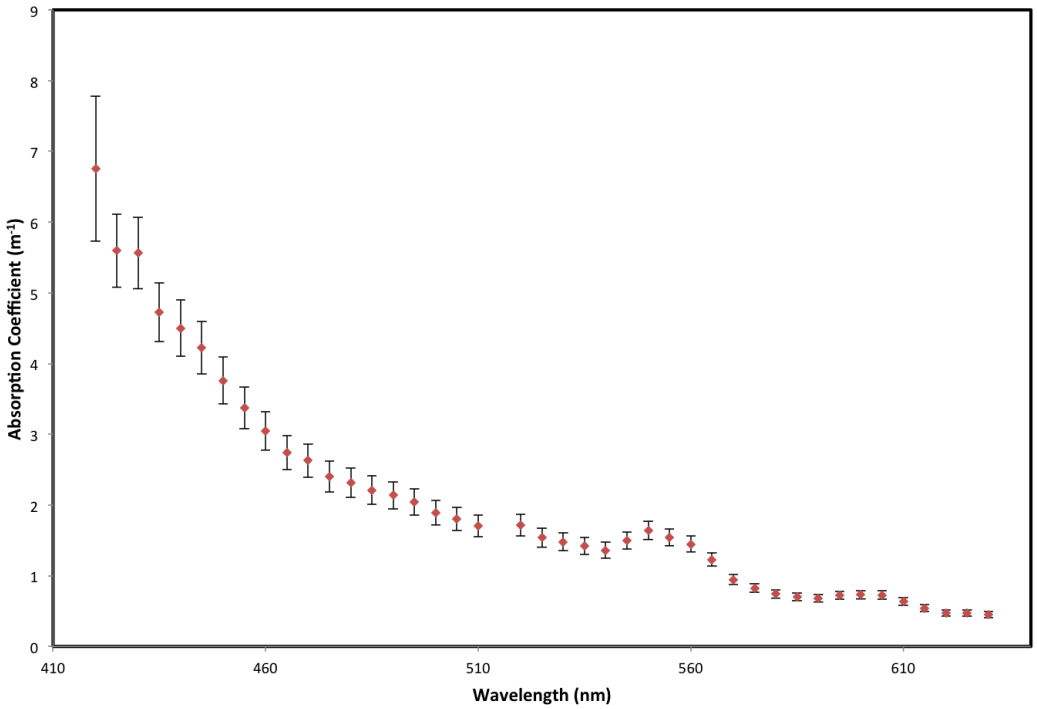

Figure 5.17: The absorption coefficient for a sample of ∼60 million RPE cells in 3 ml of PBS solution. The contribution to the absorption coefficient from the PBS solution has been subtracted out.

This data shows the effectiveness of the ICRDS technique for measuring absorption coefficients of scattering samples. Even with the limitation of small sample sizes, 3 ml in a 63.4 mm $D = H$ cylindrical cavity, the high-sensitivity of ICRDS allows for the distinction of the correspondingly small changes in absorption between the various samples.

Several possibilities exist for improving the results above 630 nm. The steady decrease of the cavity reflectivity with increasing wavelength suggests the possibility that the hydrophilic fumed silica still contains some trapped water. The high-temperature bakeout process may not be sufficient to remove all of this trapped water. Performing this high-temperature bakeout under vacuum may allow for additional removal of any trapped water, or other volatile contaminants. Additionally, switching to another calibration dye with stronger absorption above 650 nm could allow for better discrimination between various dye concentrations in that region. As mentioned above, Fig. 5.15 seems to show that the water in the various samples becomes the dominant contribution to the total absorption coefficient above 700 nm. This could potentially be alleviated by increasing the concentration of the RPE cells, in conjunction with finding a more strongly absorbing dye.

Table 5.1: Table of the absorption coefficient from 420-550 nm for a sample of ∼60 million RPE cells in 3 ml of PBS solution. The contribution to the absorption coefficient from the PBS solution has been subtracted out.

Wavelength (nm)	**Abs. Coeff. (m^{-1})**	**Relative Uncertainty (m^{-1})**
420	6.75	1.02
425	5.59	0.51
430	5.56	0.50
435	4.73	0.42
440	4.50	0.40
445	4.22	0.37
450	3.76	0.33
455	3.38	0.30
460	3.04	0.27
465	2.74	0.24
470	2.63	0.24
475	2.40	0.22
480	2.31	0.21
485	2.21	0.20
490	2.14	0.19
495	2.04	0.19
500	1.89	0.17
505	1.80	0.16
510	1.70	0.15
520	1.71	0.15
525	1.54	0.14
530	1.48	0.13
535	1.42	0.12
540	1.36	0.11
545	1.50	0.12
550	1.64	0.13

Table 5.2: Table of the absorption coefficient from 555-630 nm for a sample of ∼60 million RPE cells in 3 ml of PBS solution. The contribution to the absorption coefficient from the PBS solution has been subtracted out.

Wavelength (nm)	**Abs. Coeff. (m^{-1})**	**Relative Uncertainty (m^{-1})**
555	1.54	0.12
560	1.45	0.11
565	1.23	0.09
570	0.94	0.07
575	0.82	0.06
580	0.74	0.06
585	0.70	0.05
590	0.68	0.05
595	0.72	0.06
600	0.73	0.06
605	0.73	0.06
610	0.63	0.05
615	0.54	0.05
620	0.47	0.04
625	0.47	0.05
630	0.45	0.05

6. SUMMARY AND CONCLUSIONS

We have developed a new diffuse reflecting material and demonstrated its use for constructing high-reflectivity integrating cavities for various spectroscopic applications. The new material is a high-purity fumed silica powder that can be packed to produce diffuse reflecting walls. We report reflectivity values as high as 0.9992 at 532 nm, and 0.9969 at 266 nm for cavities made of this fumed silica. These values are, to the author's best knowledge, the highest diffuse reflectivity values ever produced. Furthermore, we have successfully used these cavities for a wide variety of spectroscopy applications. Results were presented that demonstrate how these integrating cavities can enhance Raman and fluorescence signals from various molecules and compounds, allowing for trace detection of these substances in air, or in solution. The setup for both of these applications was both simple, and inexpensive.

The fumed silica was also used to construct the walls of an integrating cavity absorption meter (ICAM) for measuring the absorption coefficient of pure water, a_{pw}, in the UV region from 250-400 nm. Two versions of this UV-ICAM were made and used in the experiment. The two versions show inconsistent results for the absorption coefficient, suggesting that future work is needed to accurately determine a_{pw}.

We also introduced a new spectroscopic technique that we call integrating cavity ring-down spectroscopy (ICRDS). It is based on traditional cavity ring-down spectroscopy (CRDS), but the mirrored cavity is replaced with an integrating cavity. ICRDS offers two significant benefits over traditional CRDS. The first benefit is that ICRDS provides a direct measurement of the absorption, as opposed to CRDS, which measures attenuation. In other words, ICRDS is insensitive to any scattering in the

sample. The second benefit is that the integrating cavities have no preferred modes, and thus there is no need for cavity mode-locking. We demonstrated the effectiveness of ICRDS by using it to measure the the absorption coefficient of retinal pigment epithelium (RPE) cells from 420-630 nm.

Finally, we discussed the idea that light propagating inside an integrating cavity will spend a small amount of time in the cavity wall during each reflection. We demonstrated this cavity wall-time by measuring it with two independent techniques. The results show that the wall-time is on the order of several picoseconds in magnitude, and thus is an important parameter to consider for applications involving the temporal response of an integrating cavity.

REFERENCES

[1] J. Palmer and B. Grant, *The Art of Radiometry*, SPIE Press Monograph (SPIE Press, 2010).

[2] R. Boyd, *Radiometry and the Detection of Optical Radiation*, Wiley series in pure and applied optics (Wiley, 1983).

[3] C. Mobley, *Light and Water: Radiative Transfer in Natural Waters* (Academic Press, 1994).

[4] S. Chandrasekhar, *Radiative Transfer*, Dover Books on Intermediate and Advanced Mathematics (Dover Publications, 1960).

[5] C. Bohren and E. Clothiaux, *Fundamentals of Atmospheric Radiation: An Introduction with 400 Problems*, Physics textbook (Wiley, 2006).

[6] Labsphere, "A guide to reflectance coatings and materials," Tech. rep., Labsphere, Inc., http://www.labsphere.com/ (2006).

[7] F. E. Nicodemus, J. C. Richmond, J. J. Hsia, I. W. Ginsberg, and T. Limperis, "Radiometry," (Jones and Bartlett Publishers, Inc., USA, 1992), chap. Geometrical Considerations and Nomenclature for Reflectance, pp. 94–145.

[8] J. Beaulieu, "A guide to integrating sphere theory and applications," Tech. rep., Labsphere, Inc., http://www.labsphere.com/ (1999).

[9] P. Elterman, "Integrating cavity spectroscopy," Appl. Opt. **9**, 2140–2142 (1970).

[10] E. S. Fry, J. Musser, G. W. Kattawar, and P.-W. Zhai, "Integrating cavities: temporal response," Appl. Opt. **45**, 9053–9065 (2006).

[11] F. Grum and T. E. Wightman, "Absolute reflectance of eastman white reflectance standard," Appl. Opt. **16**, 2775–2776 (1977).

[12] F. Grum and G. W. Luckey, "Optical sphere paint and a working standard of reflectance," Appl. Opt. **7**, 2289–2294 (1968).

[13] I. C. on Illumination, *International Lighting Vocabulary*, International Commission on Illumination: Publication (Bureau central de la CIE, 1970).

[14] Labsphere, "Spectralon® care and handling guidelines," Tech. rep., Labsphere, Inc., http://www.labsphere.com/.

[15] D. R. Gibbs, F. J. Duncan, R. P. Lambe, and T. M. Goodman, "Ageing of materials under intense ultraviolet radiation," Metrologia **32**, 601 (1995).

[16] W. Möller, K.-P. Nikolaus, and A. Höpe, "Degradation of the diffuse reflectance of spectralon under low-level irradiation," Metrologia **40**, S212 (2003).

[17] A. E. Stiegman, C. J. Bruegge, and A. W. Springsteen, "Ultraviolet stability and contamination analysis of spectralon diffuse reflectance material," Optical Engineering **32**, 799–804 (1993).

[18] C. J. Bruegge, A. E. Stiegman, R. A. Rainen, and A. W. Springsteen, "Use of spectralon as a diffuse reflectance standard for in-flight calibration of earth-orbiting sensors," Optical Engineering **32**, 805–814 (1993).

[19] G. G. Stokes, "On the intensity of the light reflected from or transmitted through a pile of plates," Proceedings of the Royal Society of London **11**, 545–556 (1860-1862).

[20] H. Barthel, M. Heinemann, M. Stintz, and B. Wessely, "Particle sizes of fumed silica," Chemical Engineering & Technology **21**, 745–752 (1998).

[21] E. Industries, "Product information: Aerosil® EG50," Tech. rep., Evonik Industries, http://www.evonik.com/.

[22] J. A. Musser, "Novel instrumentation for a scattering independent measurement of the absorption coefficient of natural waters, and a new diffuse reflector for spectroscopic instrumentation and close cavity coupling," Ph.D. thesis, Texas A&M University (2006).

[23] A. O'Keefe and D. A. G. Deacon, "Cavity ring-down optical spectrometer for absorption measurements using pulsed laser sources," Review of Scientific Instruments **59**, 2544–2551 (1988).

[24] P. Zalicki and R. N. Zare, "Cavity ring-down spectroscopy for quantitative absorption measurements," The Journal of Chemical Physics **102**, 2708–2717 (1995).

[25] E. Suzdal'tsev, "The sintering process of quartz ceramics," Refractories and Industrial Ceramics **44**, 236–241 (2003).

[26] R. M. Pope and E. S. Fry, "Absorption spectrum (380–700 nm) of pure water. ii. integrating cavity measurements," Appl. Opt. **36**, 8710–8723 (1997).

[27] Z. Lu, "Optical absorption of pure water in the blue and ultraviolet," Ph.D. thesis, Texas A&M University (2006).

[28] R. C. Smith and K. S. Baker, "Optical properties of the clearest natural waters (200–800 nm)," Appl. Opt. **20**, 177–184 (1981).

[29] T. I. Quickenden and J. A. Irvin, "The ultraviolet absorption spectrum of liquid water," The Journal of Chemical Physics **72**, 4416–4428 (1980).

[30] L. P. Boivin, W. F. Davidson, R. S. Storey, D. Sinclair, and E. D. Earle, "Determination of the attenuation coefficients of visible and ultraviolet radiation in heavy water," Appl. Opt. **25**, 877–882 (1986).

[31] R. A. J. Litjens, T. I. Quickenden, and C. G. Freeman, "Visible and near-ultraviolet absorption spectrum of liquid water," Appl. Opt. **38**, 1216–1223 (1999).

[32] A. C. Tam and C. K. N. Patel, "Optical absorptions of light and heavy water by laser optoacoustic spectroscopy," Appl. Opt. **18**, 3348–3358 (1979).

[33] F. M. Sogandares and E. S. Fry, "Absorption spectrum (340–640 nm) of pure water. i. photothermal measurements," Appl. Opt. **36**, 8699–8709 (1997).

[34] R. A. Cruz, A. Marcano, C. Jacinto, and T. Catunda, "Ultrasensitive thermal lens spectroscopy of water," Opt. Lett. **34**, 1882–1884 (2009).

[35] E. S. Fry, G. W. Kattawar, and R. M. Pope, "Integrating cavity absorption meter," Appl. Opt. **31**, 2055–2065 (1992).

[36] L. Wang, "Measuring optical absorption coefficient of pure water in the uv using the integrating cavity absorption meter," Ph.D. thesis, Texas A&M University (2008).

[37] G. Berden, R. Peeters, and G. Meijer, "Cavity ring-down spectroscopy: Experimental schemes and applications," International Reviews in Physical Chemistry **19**, 565–607 (2000).

[38] R. Boyd, *Nonlinear Optics*, Nonlinear Optics Series (Elsevier Science, 2008).

[39] J. Popp and W. Kiefer, *Raman Scattering, Fundamentals* (John Wiley & Sons, Ltd, 2006).

[40] C. Krafft, B. Dietzek, M. Schmitt, and J. Popp, "Raman and coherent anti-stokes raman scattering microspectroscopy for biomedical applications," Journal of Biomedical Optics **17**, 040801–1–040801–15 (2012).

[41] C. A. Lieber and A. Mahadevan-Jansen, "Automated method for subtraction of fluorescence from biological Raman spectra,," Applied Spectroscopy **57**, 1363–1367 (2003).

[42] J. N. Bixler, M. T. Cone, B. H. Hokr, J. D. Mason, E. Figueroa, E. S. Fry, V. V. Yakovlev, and M. O. Scully, "Ultrasensitive detection of waste products in water using fluorescence emission cavity enchanted spectroscopy," Accepted for Publication in the Proceedings of the National Academy of Sciences (2014).

[43] Y. Miyabara, N. Sugaya, J. Suzuki, and S. Suzuki, "Estimation of urobilin as a fecal pollution indicator in the aquatic environment," Bulletin of Environmental Contamination and Toxicology **53**, 77–84 (1994).

[44] E. Collinder, G. Björnhag, M. Cardona, E. Norin, C. Rehbinder, and T. Midtvedt, "Gastrointestinal host-microbial interactions in mammals and fish: Comparative studies in man, mice, rats, pigs, horses, cows, elks, reindeers, salmon and cod," Microbial Ecology in Health and Disease **15**, 66–78 (2003).

[45] Y. Miyabara, M. Tabata, J. Suzuki, and S. Suzuki, "Separation and sensitive determination of i-urobilin and 1-stercobilin by high-performance liquid chromatography with fluorimetric detection," Journal of Chromatography B: Biomedical Sciences and Applications **574**, 261–265 (1992).

[46] C.-W. Lam, C.-K. Lai, and Y.-W. Chan, "Simultaneous fluorescence detection of fecal urobilins and porphyrins by reversed-phase high-performance thin-layer chromatography," Clinical Chemistry **44**, 345–346 (1998).

[47] J. Kerkhoff and H. Peters, "A reproducible estimation of the urobilin concentration in urine by means of a modified schlesinger test," Clinica Chimica Acta **21**, 133–137 (1968).

[48] R. V. Bull, C. Lim, and C. Gray, "High-performance liquid chromatography of bile pigments: Separation and characterization of the urobilinoids," Journal of Chromatography A **218**, 647–652 (1981).

[49] S. Flock, M. Patterson, B. Wilson, and D. Wyman, "Monte carlo modeling of light propagation in highly scattering tissues. i. model predictions and comparison with diffusion theory," Biomedical Engineering, IEEE Transactions on **36**, 1162–1168 (1989).

[50] K. Muellner, E. Bodner, G. E. Mannor, G. Wolf, T. Hofmann, and W. Luxenberger, "Endolacrimal laser assisted lacrimal surgery," British Journal of Ophthalmology **84**, 16–18 (2000).

[51] J. C. Murchio and M. B. Allen, "Measurement of absorption spectra of chlorophyll in algal cell suspensions*," Photochemistry and Photobiology **1**, 259–266 (1962).

[52] J. R. Mourant, R. R. Gibson, T. M. Johnson, S. Carpenter, K. W. Short, Y. R. Yamada, and J. P. Freyer, "Methods for measuring the infrared spectra of biological cells," Physics in Medicine and Biology **48**, 243 (2003).

[53] J. R. Mourant, J. P. Freyer, A. H. Hielscher, A. A. Eick, D. Shen, and T. M. Johnson, "Mechanisms of light scattering from biological cells relevant to noninvasive optical-tissue diagnostics," Appl. Opt. **37**, 3586–3593 (1998).

[54] B. Cassin, S. Solomon, and M. Rubin, *Dictionary of Eye Terminology* (Triad Pub. Co., 1984).

[55] M. Boyer, G. Poulsen, and T. Nork, "Relative contributions of the neurosensory retina and retinal pigment epithelium to macular hypofluorescence," Archives of Ophthalmology **118**, 27–31 (2000).

[56] J.-Y. Kim, H. Zhao, J. Martinez, T. Doggett, A. Kolesnikov, P. Tang, Z. Ablonczy, C.-C. Chan, Z. Zhou, D. Green, and T. Ferguson, "Noncanonical autophagy promotes the visual cycle," Cell **154**, 365–376 (2013).

APPENDIX A. ICAM CALIBRATION

Section 3.6 gave a brief summary of the two calibration methods involved in ICAM measurements. This appendix will provide a more thorough description of these methods.

A.1 Offset Calibration

In Sec. 3.4 we derived the following working equation for the ICAM,

$$S = \frac{4}{C_1} aV + C_0', \tag{A.1}$$

where S is the ratio of the outer cavity signal to the inner cavity signal, a is the absorption coefficient of the medium in the sample region, V is the volume of the sample region, and C_1 and C_0 are the coefficients to be determined by calibration. Solving Eq. A.1 for the absorption coefficient, we find,

$$a = \frac{C_1}{4V} \left(S - C_0' \right) \equiv C_1' \left(S - C_0 \right), \tag{A.2}$$

where we have replaced the term $C_1/4V$ by C_1'. Looking at Eq. A.2, we see that the coefficients C_0 and C_1 can be thought of as offset and normalization constants, respectively. Determining these coefficients is essential for the calibration of any measurements made with the ICAM.

We begin by considering the case of an ideal ICAM, where both C_1' and C_0' are assumed to be constants that are independent of a for a given wavelength. For an empty cavity, a will be zero, and Eq. A.1 reduces to $S_E = C_0'$, where S_E denotes the empty cavity signal. To gain some insight on the second calibration constant, C_1', consider the following partial derivative of Eq. A.2,

$$\left.\frac{\partial a}{\partial S}\right|_V = \frac{C_1}{4V} = C_1'. \tag{A.3}$$

This suggests that C_1' can be determined by plotting the absorption coefficient versus signal for several solutions of known absorption. The details of this procedure is described in the next section.

In reality, the determination of the offset calibration C_0' is more complicated than the ideal case described above. Figure A.1 is an example of actual data for UVICAM-I at a wavelength of 404 nm. The plot shows the ICAM signal S as a function of the volume V of pure water in the sample region, along with a linear fit to the data. There is a clear difference between between the y-intercept of the fit, and the actual measured value for the empty cavity. To account for this discrepancy we must take a closer look at the design of actual experimental ICAM.

The inner cavity of the ICAM has several holes that allow light to leak out, and thus perturb the irradiance on the cavity wall. One of these holes is the output coupling for the detector, and the other two are the tubes that allow the water sample to flow in and out of the inner cavity. In addition to this, the change in the index of refraction as water fills the cavity leads to additional perturbations. The net result is that there are systematic deviations in the irradiance F_0 on the cavity wall at the position of the detection fiber. Furthermore, these systematic deviations will, in general, depend on both the wavelength, and the absorption of the sample. The deviations are manifested as shifts in the signal S, and occur as water first enters the cavity, as water passes the position of the detection fiber, and as the water just fills the cavity. Recalling Fig. 3.2, we see that the detection fiber is located approximately halfway up the height of the cavity. Thus we can denote the signal at these three points as S_E for the empty cavity, S_H for the half-filled cavity , and S_F for the full

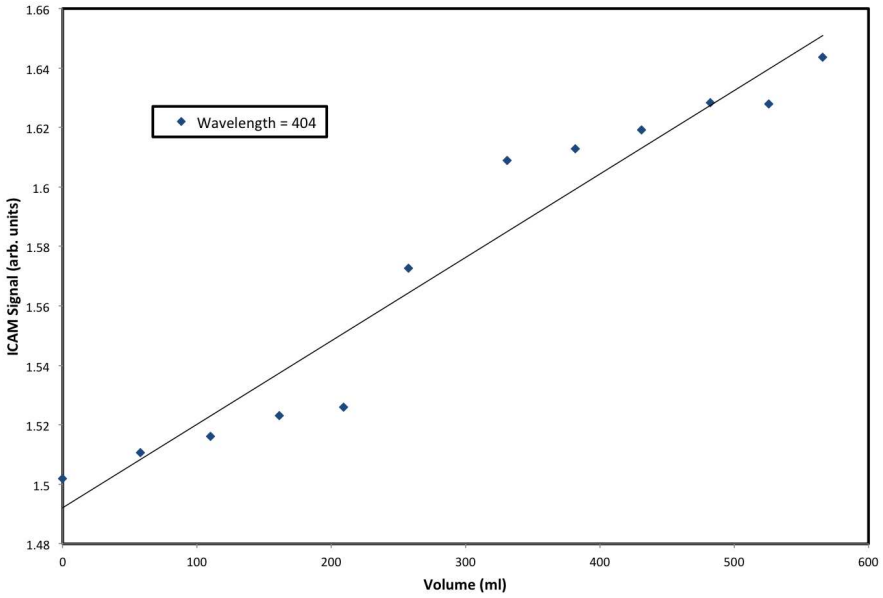

Figure A.1: Example of the ICAM signal S as a function of the volume V of pure water in the sample region at 404 nm. A linear fit to the data is also shown.

cavity.

Figure A.2 shows a simulated plot of the ICAM signal vs. the volume of water in the cavity with the systematic shifts in signal for S_E, S_H, and S_F labeled s_1, s_0, and s_2, respectively. The plot also shows a linear fit to the data (excluding the points at S_E, S_H, and S_F). This fit takes the form,

$$f(V) = f_0\Theta(V - 280) + f_1\Theta(280 - V) + V\frac{\partial S}{\partial V}, \tag{A.4}$$

where f_0 and f_1 are the intercepts, $\Theta(...)$ is the Heaviside step function, and V is the volume of water in the cavity. The cavity sample region has a total volume of 566 ml, so the value of 283 ml in Eq. A.4 represents the point when the cavity is

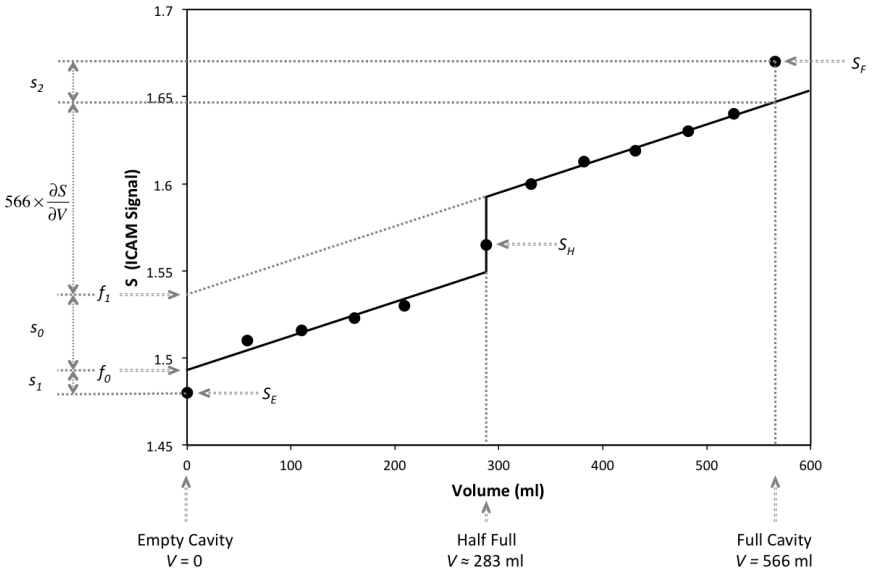

Figure A.2: Simulated plot of the ICAM signal S vs. the volume of water in the cavity. The shifts s_0, s_1, and s_2 are shown, along with a linear fit to the data (excluding the points S_E, S_H, and S_F).

half-full.*

A standard experiment for the measurement of the absorption coefficient of pure water (or any other absorbing sample) involves first measuring a baseline for the empty cavity, S_E, and then measuring the signal when the cavity is filled with pure water. Using Eq. A.2 for the case of an ideal ICAM we can express the absorption coefficient as

*This description is specific to UVICAM-I. The calibration procedure for UVICAM-II is identical, with the exception that there is no discontinuity at S_H. This is because the quartz rod that samples the light from the inner cavity in UVICAM-II is at the top of the sample region, as opposed to half-way up (see Figs. 3.2 and 3.3)

$$a = \frac{C_1}{4V}\left(S_F - S_E\right). \tag{A.5}$$

This ideal expression can be modified for a practical ICAM by including the shifts from Fig. A.2, leading to

$$a = \frac{C_1}{4V}\left[\left(S_F - s_2\right) - \left(S_E + s_0 + s_1\right)\right]. \tag{A.6}$$

If we define a net offset $s(\lambda)$ as

$$s(\lambda) = s_0(\lambda) + s_1(\lambda) + s_2(\lambda), \tag{A.7}$$

then Eq. A.6 can be rewritten as

$$a = \frac{C_1}{4V}\left(S_F - S_E - s(\lambda)\right). \tag{A.8}$$

Therefore, it is essential to find the net offset as a function of wavelength in order to calculate the absorption coefficient. Figure A.2 suggests a simple way to calculate $s(\lambda)$:

$$s(\lambda) = S_F - S_E - V\frac{\partial S}{\partial V} = S_F - S_E - 566 \times \frac{\partial S}{\partial V}. \tag{A.9}$$

Thus we simply fill the ICAM sample region with sequentially increasing volumes of pure water and measure the corresponding value of S for each volume. The slope $\partial S/\partial V$ is calculated by fitting the data to the function given in Eq. A.4 (excluding the values S_E, S_H, and S_F). The net offset $s(\lambda)$ can then be calculated using Eq. A.9. Since the offset depends on λ, this must be carried out for the entire wavelength range.

The partial derivative in Eq. A.9 can be replaced by considering the following partial derivative of Eq. A.1:

$$\left.\frac{\partial S}{\partial V}\right|_a = \frac{4}{C_1}a. \tag{A.10}$$

Thus, we can write,

$$s(\lambda) = S_F - S_E - 566 \times \frac{4}{C_1}a, \tag{A.11}$$

showing the expected dependence of $s(\lambda)$ on a.

In order to isolate the absorption dependence of the offset we define a general function of the form

$$s(\lambda) = k_1 + k_2\lambda + (k_3 + k_4\lambda)\frac{\partial S}{\partial V}, \tag{A.12}$$

where we have assumed a linear dependence on the wavelength λ, combined with a linear dependence on the slope $^{\partial S}/_{\partial V}$ for $s(\lambda)$. The coefficients k_i can be determined by a least-squares fit to the $s(\lambda)$ data which is calculated from the $S(V)$ data using Eq. A.9 in the manner described above.

If we substitute Eq. A.12 into Eq. A.8 we have

$$\begin{aligned} a &= \frac{C_1}{4V}\left[S - S_E - k_1 - k_2\lambda - (k_3 + k_4\lambda)\frac{\partial S}{\partial V}\right] \\ &= \frac{C_1}{4V}\left[S - S_E - k_1 - k_2\lambda - (k_3 + k_4\lambda)\frac{4a}{C_1}\right]. \end{aligned} \tag{A.13}$$

Solving Eq. A.13 for a gives the final working equation for a practical ICAM:

$$a = C_1''\left(S_F - S_E - C_0''\right), \tag{A.14}$$

where the new coefficients C_1'' and C_0'' are given by

$$C_1'' = \frac{C_1}{4\,(V + k_3 + k_4)}, \tag{A.15}$$

$$C_0'' = k_1 + k_2\lambda. \tag{A.16}$$

It should be noted that both C_1'' and C_0'' are independent of the absorption coefficient. While Eq. A.16 is used to evaluate the offset coefficient C_0'', the normalization coefficient C_1'' is actually determined via another method discussed in the following section.

A.2 Normalization Calibration

In the previous section we saw that the normalization coefficient C_1' is related to the partial derivative of a with respect to S for constant volume (see Eq. A.10). This suggested that we could find C_1' by measuring the ICAM signal for a set of reference solutions with known absorption coefficients. The slope of the a vs. S data would then give C_1' for any given wavelength.

Consider a dilute solution of dye and pure water. The ICAM signal when the sample region is full of such a solution is given by

$$S_{solution} = S_{dye} + S_{pure\,water}, \tag{A.17}$$

and Eq. A.14 becomes,

$$a_{dye} + a_{pure\,water} = C_1''\,(S_{solution} - S_E - C_0'')\,. \tag{A.18}$$

Similarly, when the cavity is filled with pure water (i.e. no dye) we have

$$a_{pure\,water} = C_1'' \left(S_{pure\,water} - S_E - C_0'' \right). \tag{A.19}$$

Subtracting Eq. A.19 from Eq. A.18 gives

$$\begin{aligned} a_{dye} &= C_1'' \left(S_{solution} - S_{pure\,water} \right) \\ &= C_1'' S_{dye}. \end{aligned} \tag{A.20}$$

Thus, we find that our modified normalization coefficient C_1'' from Eqs. A.14 and A.16 can also be expressed as the slope of a_{dye} with respect to S_{dye}, that is

$$C_1'' = \frac{\partial a_{dye}}{\partial S_{dye}}. \tag{A.21}$$

Reference solutions were prepared by dissolving an absorbing dye (Irgalan Black powder) into pure water to make a master dye solution. Typical concentrations for this master solution were ∼50 mg of Irgalan Black dissolved into 1000 ml of pure water. This solution was then sonicated and filtered several times through Gelman Supro®-200 47 mm diameter, 0.2 μm membrane filters to remove any undissolved solute. The absorbance of this master dye was measured using an Agilent 8453 UV-VIS spectrophotometer. This instrument has a wavelength range of 190-1100 nm, and a photometric accuracy of ±0.005 Au at 1 Au. In order to isolate the absorbance of the dye A_{dye} from the absorbance of the solution $A_{solution}$, a pure water blank was measured and subtracted out (i.e. $A_{dye} = A_{solution} - A_{pure\,water}$). The absorbance A_{dye} can then be converted to an absorption coefficient a_{dye} using the following definition of absorbance for liquids,

$$A = \log_{10} \left(\frac{I_0}{I} \right) \tag{A.22}$$

where I_0 is the input intensity, and I is the intensity transmitted through the sample. Combining this with the definition of the absorption coefficient discussed in Sec. 1.2, we have

$$a_{dye} = \frac{1}{L} \ln \frac{I_0}{I} = \frac{\ln 10}{L} \log_{10} \frac{I_0}{I} = \frac{2.303}{L} A_{dye}, \tag{A.23}$$

where L is the path length through the sample. The fused silica cuvettes used for these measurements had a path length of 10 mm. Figure A.3 shows a plot of absorbance vs. wavelength for a typical master dye solution.

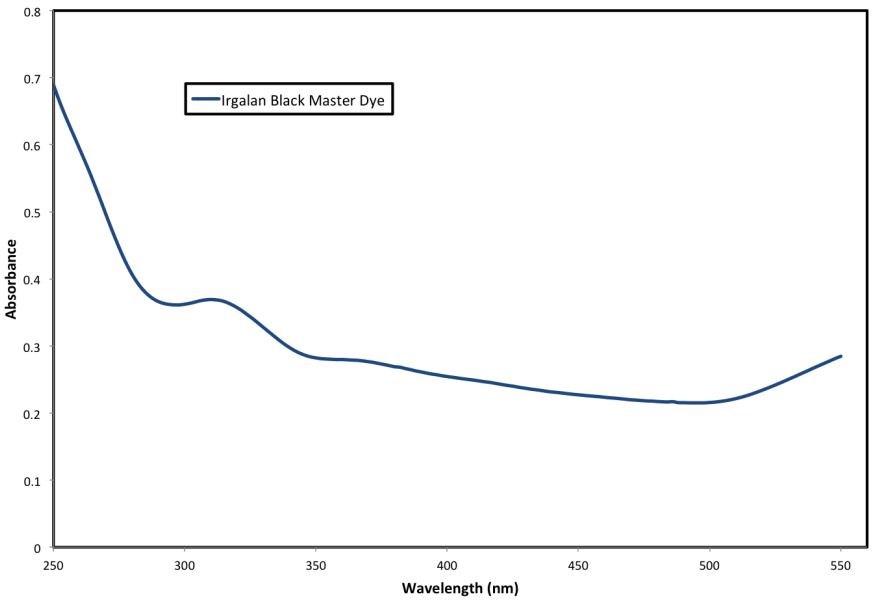

Figure A.3: Plot of the absorbance vs. wavelength for a master dye solution of Irgalan Black diluted in pure water.

Small volumes of this master dye solution can be diluted with additional pure

to form to form a set of dye solutions of known concentration, and thus known absorption coefficient. Typically a set of 8-10 solutions with steadily increasing dye concentrations are used. The lowest and highest concentration are chosen such that the absorption coefficient a_{dye} at 418 nm is approximately 0.01m^{-1}, and $0.1\text{m}^{-}1$, respectively. The remaining concentrations are evenly spaced between these two. The ICAM signal $S_{solution}$ is measured over the entire wavelength range with the sample region filled with the lowest concentration solution. This process is then repeated for each solution in order of increasing concentration. S_{dye} is then calculated by subtracting the value of $S_{pure\,water}$ from each of these measurements. Figure A.4 shows a plot of a_{dye} vs. S_{dye} at 404 nm, along with a linear fit to the data. The slope of this fit gives the value of C_1'' for this wavelength.

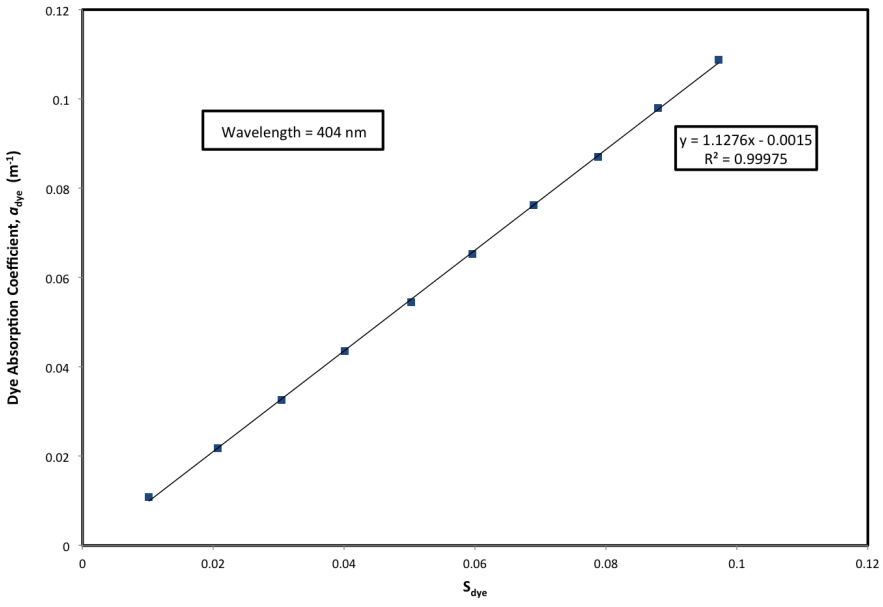

Figure A.4: Example of the absorption coefficient of a set of dye solutions a_{dye} vs. the ICAM signal S_{dye} at 404 nm. A linear fit to the data is also shown.

Thus, a full ICAM measurement for a given wavelength range requires the following basic steps. First, the empty cavity signal S_E is measured to provide a baseline. Then the cavity is filled with pure water to measure S_F over the same range. Both of these measurements are typically averaged over several runs to reduce random fluctuations in the data. The volumetric pure water measurements to determine the offset coefficient C_0'' are performed next. In order to avoid any potential contamination of the ICAM before the pure water samples are measured, the dye solution measurements to determine the normalization coefficient C_1'' are performed last. After a full set of measurements are completed, the ICAM is thoroughly cleaned. This is typically done by first filling the ICAM with a chromic acid cleaning solution to dissolve any residual dye. The ICAM is then thoroughly rinsed with pure water several times to remove the acid.

APPENDIX B. ERROR ANALYSIS

B.1 Reflectivity Measurements

There are two sources of error for the absolute reflectivity measurements presented in Sec. 2.7: error in the cavity dimensions, and error in the decay constant. Any error in the cavity dimensions manifests itself in $\bar{d}$. The machining process for the cylindrical cavities had an accuracy of ± 0.3 mm for the height, and ± 0.03 mm for the radius (the differing values are due to the difference in accuracy for vertical vs. horizontal adjustments on the mill). This leads to relative uncertainties of $\pm 0.6\%$ and $\pm 0.7\%$ for the $\bar{d}$ of the 532 nm, and 266 nm test cavities, respectively.

The uncertainty in the decay constant τ was determined using the 99% confidence interval values for the convolution fit function given in Eq. 2.13. These were calculated using the nonlinear fitting parameter confidence options in Mathematica®. The relative uncertainty for τ is less than $\pm 1\%$ for both of the tests. Using Eq. 2.11, and basic error propagation, we find the uncertainty in the cavity reflectivity ρ is less than $\pm 1\text{x}10^{-4}$ for both the 532 nm and 266 nm tests.

B.2 UVICAM Measurements

Descriptions of the error analysis for the ICAM measurements have been presented in detail in previous works, and will not be repeated here.[26,36] Typical measurements for a_{pw} have relative uncertainties of less than 5% for wavelengths from 535-700 nm, less than 10% for 430-535 nm, and less than 16% for 380-430 nm. Similarly, the UV region from 250-380 nm typically produces relative errors on the order of 10%, or less. These relative errors are based on the standard deviations in the ICAM signal S, the accuracy of the volume measurements in the volumetric water calibration (see App. A), the accuracy of the diluting process for the dye offset cali-

bration (see App. A), and the accuracy of the spectrophotometer measurements for the absorption coefficient of the calibration dye.

It is easy to tell from the data shown in Sec. 3.7 that the differences between the UV-ICAM I and II data sets often exceeds the relative unceratinties quoted above. The same is true for either of the UV-ICAM data sets when compared to the Lu or Wang data sets.[27,36] This suggests that there is a systematic error in the UV-ICAM measurements that has not been accounted for.

B.3 Cavity Wall-Time Measurements

In Sec. 4.3 the cavity wall-time was measured by two independent methods. The first involved measuring the decay constant vs. $\bar{d}$ for increasing cavity sizes. These various cavity sizes were achieved by machining out ever larger cavities from two cylindrical cavity halves. The machining process had an accuracy of ± 0.3 mm for the height of the cavity, and ± 0.03 mm for the radius. All cavities were right-circular cylinders with $D = H$. Based on Eq. 2.12, the resulting relative uncertainty in the cavity $\bar{d}$ is given by the expression

$$\frac{\delta \bar{d}}{\bar{d}} = \sqrt{\left(\frac{\delta V}{V}\right)^2 + \left(\frac{\delta S}{S}\right)^2}, \tag{B.1}$$

where V is the cavity volume, and S is the cavity surface area. This gives a relative uncertainty of only 2% for the $\bar{d}$ of the smallest cavity size, with the larger cavities having even smaller values. Just as for the absolute reflectivity measurements described above, uncertainty in the decay constant τ was determined using the 99% confidence interval values for the convolution fit, and was calculated in Mathematica®. All of the relative uncertainties for τ were less than $\pm 1\%$.

The scatter of the data around the linear fit in Fig. 4.3 exceeds the size of the error bars for the individual data points. Thus the contributions from these er-

ror bars is neglected when calculating the error in the wall-time δt. Instead, we simply use the standard method for calculating the uncertainty in the slope and y-intercept for a linear leas-squares fit. Consider a series of N pairs of measurements (x_1, y_1),(x_2, y_2),...,(x_N, y_N). Suppose we want to find a least-squares fit of this data to a linear function of the form

$$y = mx + b, \tag{B.2}$$

where m is the slope, and b is the y-intercept. Then m and b are given by,

$$\begin{aligned} m &= \frac{N\sum xy - \sum x \sum y}{\Delta}, \text{ and} \\ b &= \frac{\sum x^2 \sum y - \sum x \sum xy}{\Delta}, \end{aligned} \tag{B.3}$$

where Δ is given by,

$$\Delta = N\sum x^2 - \left(\sum x\right)^2. \tag{B.4}$$

The uncertainties for m and b are given by

$$\begin{aligned} \sigma_m &= \sigma_y\sqrt{\frac{N}{\Delta}}, \text{ and} \\ \sigma_b &= \sigma_y\sqrt{\frac{\sum x^2}{\Delta}}, \end{aligned} \tag{B.5}$$

where σ_y is given by

$$\sigma_y = \sqrt{\frac{1}{N-2}\sum_{i=1}^{N}(y_i - b - mx_i)^2}. \tag{B.6}$$

Applying Eq. B.5 to the data in Fig. 4.3 gives relative uncertainties of $\pm 2.6\%$ for the

slope, and ±65.6% for the y-intercept. This leads to a relative uncertainty of ±66% for δt.

The second method for determining the wall-time δt involved measuring the decay constant τ for several dye solutions of known absorption coefficient a_{dye}. The wall-time is then calculated from the slope of a linear least-squares fit to a plot of $1/\tau$ vs. a_{dye}. The uncertainty in the individual data points comes from the error in the decay constants, the error in the spectrophotometer measurements for the master dye solution, and the error in the diluting process for the various dye solutions. The master dye used for these experiments was a solution of Irgalan Black powder and ultra-pure water.

The relative uncertainties in the values of the decay constants were determined by the same means mentioned above, and were all less than ±1%. The absorption coefficient for the master dye solution a_{md} was measured with a Agilent 8453 UV-VIS spectrophotometer. The accuracy of this spectrophotometer is ±0.005, and the master dye absorbance at 532 nm was measured as 0.283 Au. Thus the relative uncertainty for a_{md} is $\sim \pm 2\%$.

The dye solutions used were made by diluting small amounts of the master dye with pure water. This dilution process involved first taking 10 ml of the master dye using a 10 ml pipet with an accuracy of ±0.02 ml. The same pipet was then used to add 40 ml of pure water, giving a total dilution factor of 5 ± 0.01. This diluted solution was then used to make each of the samples for the experiment. This involved pipetting small volumes of the diluted solution (ranging from 0.5 to 3.5 ml) using a 2 ml pipet with an accuracy of ±0.01 ml, and further diluting it to 1000 ml in a volumetric flask with an accuracy of ±0.3 ml. Thus for the entire dilution process we have an overall relative uncertainty of ±2% for the $10,000$x dilution, and ±0.4% for the 1429x dilution. Combining this with the uncertainty for the absorption coefficient

of the master dye, we find a ±2.5% to ±1.6% range of relative uncertainties for the absorption coefficient of the various diluted dye samples.

Inspection of Fig. 4.4 shows that, much like the previous case, the scatter in the data points relative to the least-squares fit is larger than the error bars on the individual data points. Therefore, the contribution of these error bars is neglected in the calculation of the uncertainty for the wall-time δt. For this case, δt is a simple function of the slope of the least-squares fit, the cavity $\bar{d}$, and the speed of light in water. The relative uncertainty for the diameter of the spherical sample region (i.e. the cavity diameter) is assumed to be ±1%, and thus the relative uncertainty for $\bar{d}$ is also ±1%. Equations B.3 and B.5 give a value of $m = 0.212 \pm 0.014$ $^{\mathrm{m}}/_{\mathrm{ns}}$, or a relative uncertainty of ±7%. Standard propagation of uncertainties leads to a relative uncertainty of ±7% for δt.

B.4 Cavity Enhanced Fluorescence Measurements

The plot in Fig. 5.12(B) shows the fluorescence signal vs. concentration for urobilin solutions inside an integrating cavity. This fluorescence signal was calculated by integrating the total fluorescence curve for each concentration. To reduce the effects of thermal noise, the spectrometer was set to average 30 times for each spectra taken. The measurement was repeated 5 times for each concentration, and the error bars represent the standard deviation of the integrated signal for these 5 scans.

B.5 ICRDS Measurements of RPE Cells

The potential sources of error for the RPE cell measurements were very similar to those described above for the wall-time measurement using the dye solutions. The uncertainties in the decay constants τ were determined using the 99% parameter confidence intervals for the convolution fits, and were calculated in Mathematica®. There were four τ's needed for each each data point: τ_{RPE}, τ_{PBS}, τ_{D1}, and τ_{D2}.

The relative uncertainties in each of these was used to determine the overall relative uncertainty in the $(\tau_{RPE}^{-1} - \tau_{PBS}^{-1}/\tau_{D1}^{-1} - \tau_{D2}^{-1})$ term that shows up in Eq. 5.4. At 420 nm the relative uncertainty for this term was ±13%, but for all other wavelengths it was less than ±6%.

The other source of error involved the two diluted dye solutions used to calibrate the measurements. The master dye used for these experiments was a solution of Irgalan Black powder and ultra-pure water. The diluted dye solutions were made by pipetting a small volume of the master dye (7 ml for dye 1, and 5 ml for dye 2) into a 250 ml volumetric flask. The accuracy of the flask was ±0.05%, and the 5 ml pipet used had an accuracy of ±1%. Therefore, the uncertainty contribution of the flask was neglected. The absorption coefficient of the master dye a_{md} was measured with a Cary UV-VIS spectrophotometer with an accuracy of 0.005 Au for an absorbance of 1 Au. This lead to a relative uncertainty for a_{md} of less than ±2% for the range from 420-630 nm. Standard uncertainty propagation was used to combine the uncertainties from the decay constants, a_{md}, and the dilution process, leading to the error bars shown in Fig. 5.17.